Aramco Journal of Technology

SPRING 2020

page 2 /

Light- and Heavy-Duty GCI Engine Combustion System Optimization Using CFD and Machine Learning: A Methodological Approach

Dr. Jihad A. Badra, Dr. Fethi Khaled, Dr. Meng Tang, Dr. Yuanjiang Pei, Dr. Janardhan Kodavasal, Dr. Pinaki Pal, Dr. Opeoluwa Owoyele, Carsten Füetterer, Mattia Brenner, Dr. Aamir Farooq, and Dr. Junseok Chang

page 35 /

Evaluation of an ENP Coating Material for Downhole Corrosion and Scale Protection in Sour Gas Wells

Dr. Tao Chen, Dr. Feng Liang, Dr. Fauken F. Chang, and Dr. Qiwei Wang

Aramco
Journal
of Technology

The *Aramco Journal of Technology* is published quarterly by the Saudi Arabian Oil Company, Dhahran, Saudi Arabia, to provide the company's scientific and engineering communities a forum for the exchange of ideas through the presentation of technical information aimed at advancing knowledge in the hydrocarbon industry.

Editor

William E. Bradshaw
william.bradshaw.1@aramco.com.sa
tel: +966-013-876-0498

Production Coordination

Richard E. Doughty

Design

Graphic Engine Design Studio
Austin, Texas, U.S.A.

The *Aramco Journal of Technology* gratefully acknowledges the assistance, contribution and cooperation of numerous operating organizations throughout the company.

ISSN 1319-2388

Contents

p. 2 **Light- and Heavy-Duty GCI Engine Combustion System Optimization Using CFD and Machine Learning: A Methodological Approach**

Dr. Jihad A. Badra, Dr. Fethi Khaled, Dr. Meng Tang, Dr. Yuanjiang Pei, Dr. Janardhan Kodavasal, Dr. Pinaki Pal, Dr. Opeoluwa Owoyele, Carsten Füetterer, Mattia Brenner, Dr. Aamir Farooq, and Dr. Junseok Chang

p. 15 **Reservoir Simulation Well Data Exchange toward Digital Transformation and Live Earth Models**

Menhal A. Al-Ismael, Dr. Ali A. Al-Turki, and Abdulaziz M. Al-Darrab

p. 24 **Laser Perforation: The Smart Completion**

Dr. Sameeh I. Batarseh, Dr. Damian P. San-Roman-Alerigi, Abdullah M. Al-Harith, and Dr. Haitham A. Othman

p. 35 **Evaluation of an ENP Coating Material for Downhole Corrosion and Scale Protection in Sour Gas Wells**

Dr. Tao Chen, Dr. Feng Liang, Dr. Fauken F. Chang, and Dr. Qiwei Wang

p. 44 **Mitigating Drilling Hazards in a High Differential Pressure Well Using Managed Pressure Drilling and Cementing Techniques**

Peter I. Egbe and Carlos O. Iturrios

p. 55 **Dependence of Key Estimates from PTA on Flow Paths in Heterogeneous Reservoir Systems**

Dr. N.M. Anisur Rahman and Sukru Sarac

p. 67 **Autonomous Reservoir Nano-Agents**

Dr. Afnan A. Mashat, Dr. Nan Shi, Dr. Todd Squires, and Dr. Amr I. Abdel-Fattah

p. 75 **Reservoir Description Insights from Interwell Gas Tracer Test**

Dr. Abdulaziz S. Al-Qasim, Dr. Sunil L. Kokal, Sven K. Hartvig, and Dr. Olaf K. Huseby

Light- and Heavy-Duty GCI Engine Combustion System Optimization Using CFD and Machine Learning: A Methodological Approach

Dr. Jihad A. Badra, Dr. Fethi Khaled, Dr. Meng Tang, Dr. Yuanjiang Pei, Dr. Janardhan Kodavasal, Dr. Pinaki Pal, Dr. Opeoluwa Owoyele, Carsten Füetterer, Mattia Brenner, Dr. Aamir Farooq, and Dr. Junseok Chang

Abstract / In this study, the combustion system of a light-duty gasoline compression ignition (GCI) engine running on a market gasoline fuel with a Research Octane Number of 91 was optimized using computational fluid dynamics (CFD) and machine learning (ML). This work was focused on optimizing the piston bowl geometry at compression ratio (CR) of 18:1, and this exercise was carried out at full load conditions (20 bar indicated mean effective pressure (IMEP)).

First, a ML grid gradient ascent (ML-GGA) algorithm was developed to optimize the performance of internal combustion engines (ICE). The developed ML-GGA model was compared with a recently developed ML genetic algorithm (ML-GA). Detailed investigations of optimization solver parameters and variables limits the extension performed in the presence of the ML-GGA model to improve the accuracy and robustness of the optimization process.

Then, a two stage optimization process was performed to optimize the bowl geometry of the CR 18:1 piston. First, a CFD design of experiments (DoE) optimization was performed where CAESES, a commercial software tool, was used to automatically perturb key piston bowl design parameters, and CONVERGE software was utilized to perform the CFD simulations. A total of 128 piston bowl designs were evaluated. Subsequently, the ML-GGA approach was used to further optimize the piston bowl design. This extensive optimization exercise yielded significant improvements in the engine performance and emissions compared to the baseline piston bowl designs. A savings of up to 15% in indicated specific fuel consumption (ISFC) was obtained. Similarly, the optimized piston bowl geometries produced significantly lower emissions compared to the baseline. Emission reductions up to 90% were obtained from this optimization exercise.

Introduction

The global demand for energy used in the transportation sector is expected to continue rising at an annual rate of 1% to 1.5% by 2040 according to recent projections[1, 2]. This increase is mainly driven by the expected rise in population, gross domestic product, and living standards. Currently, internal combustion engines (ICEs), fueled by petroleum-derived liquid hydrocarbons, gasoline and diesel, dominate the passenger and commercial transportation sectors with over 99% market share. ICEs are expected to remain the major source of the transportation energy demand in the interim future, despite significant growth in alternative energy and competing technologies, e.g., electric and fuel cells[1-3].

ICEs have been around since the 19th century and their conceptual identity as a fuel powered machine has not changed since. There have been significant technological improvements to their performance in response to fuel efficiency and emissions regulations[4]. The tools used to co-optimize the fuel and engine system have evolved over the years. Until 20 years ago, experimental prototyping was the main optimizing method. It was followed by numerical simulations, including complex three-dimensional computational fluid dynamics (CFD), which played a major role in the engine or fuel system optimization. This development was enabled by the significant advancements in computing power — supercomputers, clusters, parallelization, etc. — and numerical models — turbulence, combustion, spray, heat transfer, meshing, moving boundaries, etc.

Due to high dimensionality, complexity, and highly nonlinear dependencies in engine properties and responses, both experimental and numerical optimization approaches can be inefficient, and take a significant amount of time and effort to obtain local rather than global optimum designs and operating conditions[5-7]. To overcome the issues with manual optimizations, alternative approaches have been developed over the years.

The design of experiments (DoE) technique is commonly used now to enhance design optimization[8]. Probst et al. (2018)[8] showed that the sequential DoE approach, coupled with CFD models, can successfully and efficiently optimize engines. The sequential DoE optimization was compared to an optimization performed

using a genetic algorithm (GA). Their study highlighted the strengths of both methods for optimization. The GA — known to be an efficient and effective method — found a better optimum, while the DoE method found a good optimum with fewer total simulations. The DoE method also ran more simulations concurrently, which is an advantage when sufficient computing resources are available. GAs[9, 10] have also been used to facilitate design optimization, where an objective function is defined to represent CFD simulations. This GA approach often yields better optimum solutions compared with the DoE-based optimization.

Significant advancements have been made in the area of artificial intelligence (AI) in the last couple of decades. These advances have enabled machine learning (ML) to be a potentially effective tool to optimize the engine or fuel systems[11, 12]. Particularly, neural networks have been used in several studies to efficiently optimize the engine or fuel systems. The real-time engine control system correction[13, 14] and the effects of fuel properties on engine emissions[7, 15] are examples of some recent applications. Other ML algorithms, such as random forest and support vector machines, have also been used in engine and vehicle-related problems[16-18].

Recently, Moiz et al. (2018)[19] proposed an improved ML-GA approach based on an ensemble ML technique known as SuperLearner[20], to optimize the operating conditions of a heavy-duty gasoline compression ignition (GCI) engine. DoE was first performed to generate a database to train an ML algorithm. The ML optimization algorithm was then used without any further CFD modeling to search for optimum engine design parameters. Their approach yielded comparable optimum operating conditions in significantly less computing time compared to the CFD-GA approach[19]. Other studies that implemented ML-GAs for engine optimization may be found in the literature[7, 9, 21, 22].

Compression ignition engine technologies have been considered as attractive alternatives, because they have the potential to combine the best of gasoline and diesel engines. The compression ignition combustion mode eliminates traditional engine knock observed in spark ignition engines, and the globally lean operation reduces the engine output emissions. Additionally, a lean, throttle-less operation, coupled with higher compression ratios (CRs), improves engine efficiency. Better mixing of fuel and air prior to combustion, due to the higher volatility of gasoline, reduces soot production relative to the conventional mixing controlled (diesel) combustion. Our research group in Saudi Aramco extensively investigated the combustion of various fuels in GCI engines.

In this work, an ML grid gradient ascent (GGA) approach, with similar functionality[19] is proposed. The developed ML-GGA code builds upon the work of Moiz et al. (2018)[19]. In addition, the repeatability of the optimization method is investigated. Then, a two-stage optimization process is performed to optimize the bowl geometry of the CR 18:1 piston at full load operating conditions. Significant fuel consumption and emission reductions are obtained from this optimization process.

ML-GA Approach

Definition and Details

The ML-GA is an optimization technique that can be used to efficiently optimize ICEs. More details about this approach can be found in Moiz et al. (2018)[19], as only a brief description of the main features are provided here.

In an engine optimization task, the optimization problem is first posed and the different engine design parameters are defined. A sample of cases with different combinations of these parameters are solved using detailed CFD simulations or are prototyped to define the effect of these design variables on the performance of the studied engine. The performance of the engine is normally measured by a merit function that combines a certain set of output parameters, which need to be defined before starting the optimization process.

These sets of input variables and output parameters are utilized in a supervised ML algorithm for training purposes. The trained ML routine is then coupled with an optimization tool — in this case a GA — to search for the optimum set of engine design variables that lead to improved performance. Moiz et al. (2018)[19] used the ML package SuperLearner[20], which is available as an add-on package to the statistical software R[23].

The super learning technique calculates the optimal combination of a pool of prediction algorithms, such as the arithmetic mean (SL.mean), Lasso and Elastic-Net Regularized Generalized Linear Models (SL.gmlnet), Breiman and Cutler's Random Forests for Classification and Regression (SL.randomForest), Support Vector Machines (SL.svm), Extreme Gradient Boosting (Xgboost), linear regression models (SL.lm), and Feed-Forward Neural Networks and Multinomial Log-Linear Models (SL.nnet).

The optimal combination is a set of these multiple models with weighting factors (wf_i) that minimize the cross-validated error. The GA method used to find the optimal design by Moiz et al. (2018)[19] is the GA "malschains" (memetic algorithms with local search chains)[24]. Malschains uses a combination of local and global optimization techniques. The idea behind the algorithm is to apply a local search method on the most promising regions, which are found to have the highest fitness value using a (global) GA.

The GA in the malschains is different from a standard GA, where the individuals of the population are subjected to genetic operations simultaneously. The malschains algorithm randomly generates an initial population of individuals. The GA then evaluates the merit values (fitness) of these individuals and builds a set of individuals that can be further refined by the local search method. The main advantage of the ML-GA technique is the ability to find an optimum design for highly nonlinear problems in a short time for engine optimization tasks, where repeated CFD simulations

can be time-consuming and expensive[19]. They showed that a ML-GA reduces the optimization time from about 50 days to one day.

Repeatability and Enhancements in the ML-GA Approach

In this work, we opted to use the ML-GA methodology of Moiz et al. (2018)[19], and proposed some modifications and/or improvements to it. In this section, a detailed investigation of the repeatability ability of the optimization scheme and two additional enhancements are presented and applied to a case study[19] to demonstrate their utility. More details about the objective, design variables, and optimization problem may be found in Moiz et al. (2018)[19]. Here, only the impact of the proposed enhancements on the design solution is presented.

Repeatability

Although a ML-GA presents an efficient resource and relatively easily implemented tool for engine optimization, it can suffer from repeatability issues where the optimum set of design variables that yields the highest merit are not the same for subsequent runs. This is an anticipated behavior because the malschains optimization method in R (Rmalschains), is based on random selections, and therefore, running it multiple times could lead to different local solutions if not set with care. To avoid finding unrepeatable local optimum designs, special care has to be taken when using certain optimization schemes.

To demonstrate this, the ML-GA code of Moiz et al. (2018)[19] is reconstructed here. It is then solved using the exact same training data set five consecutive times while changing the search parameters of the Rmalschains algorithm. Table 1 summarizes the variability among the top five designs found using each set of Rmalschains where the first line (case 0) represents the base parameters used[19]. A variance higher than $1e^{-4}$ means that the merit values of the top five designs are different from each other by more than 1%. It can be clearly seen that all Rmalschains parameters affect the repeatability of the solution, and correctly setting those parameters is critical to ensure reaching the absolute optimum design in terms of merit value. For example, the number of search iterations has to be around 35,000. An iteration number of only 2,400 represented by case 1 leads to five different local optimum designs. For illustration purposes, the optimum solutions for case 1 are shown in Fig. 1.

In Fig. 1, it can be seen that the five optimal designs obtained here are different from each other despite having similar merit value (right y-axis). The observed differences can be significant for some design variables such as the number of nozzles (nNoz), start of

Table 1 *Dependence of the optimal solutions on the parameters' setting of the Rmalschains.*

Case	Popsize	ls	Istep	Effort	Alpha	Maxevals	Variance of the Top Five Designs Found
0	100	sw	100	0.8	1	35,000	3.83E-07
1	200	cmaes	300	0.5	0.5	2,400	1.05E-01
2	100	sw	200	0.8	1	35,000	1.63E-07
3	100	sw	350	0.8	1	35,000	5.05E-07
4	100	sw	3,500	0.8	1	35,000	2.23E-07
5	50	sw	3,500	0.8	1	35,000	7.76E-07
6	10	sw	3,500	0.8	1	35,000	1.44E-04
7	10	cmaes	3,500	0.8	1	35,000	2.98E-07
8	10	cmaes	3,500	0.8	1	3,500	7.29E-04
9	10	cmaes	3,500	0.8	1	500	7.01E-02
10	10	cmaes	3,500	0.5	1	3,500	1.30E-03
11	10	cmaes	3,500	0	1	3,500	7.58E-03
12	10	cmaes	3,500	0	0.5	3,500	1.34E-04
13	10	cmaes	3,500	0	0.2	3,500	8.22E-04
14	10	cmaes	3,500	0	0	3,500	8.73E-02
15	10	cmaes	3,500	0.5	0	3,500	1.88E-03
16	10	cmaes	3,500	0.5	0	3,500	1.15E-01

Fig. 1 *Optimum designs obtained using Rmalschains. The five designs obtained from repeating the Rmalschains five times are compared with the optimum design parameters[19].*

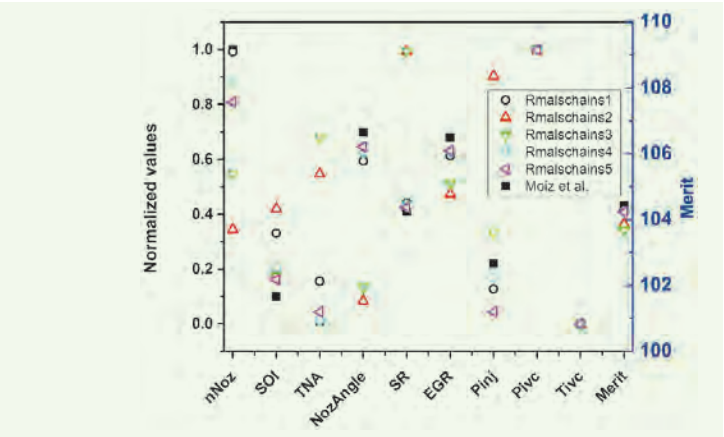

Fig. 2 *Optimum design by using the ML-GA vs. ML-GGA method[19].*

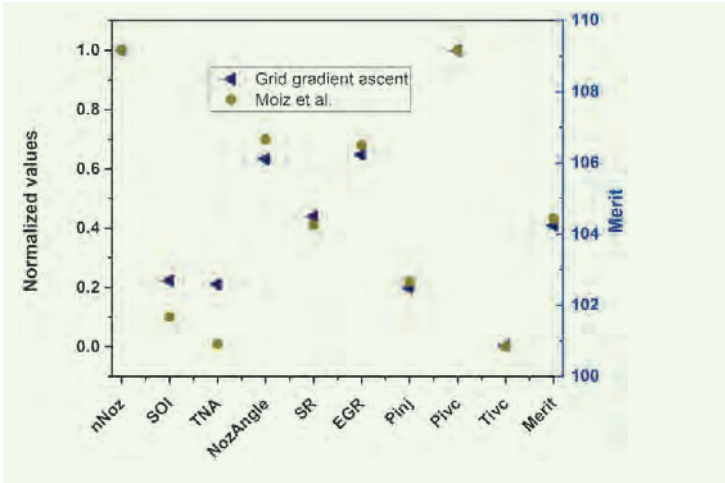

injection (SOI), total nozzle area (TNA), nozzle angle (NozAngle), swirl ratio (SR), exhaust gas recirculation (EGR) and injection pressure (Pinj). Only the obtained optimum intake valve closing pressure (Pivc) and temperature (Tivc) are similar for the different runs.

Finding the best set of optimum solutions using Rmalschains can be a tedious exercise that requires expertise. As a remedy for this, a new method is adopted in this work by utilizing a different GA and GGA, which is, although classical and forward, does not include many setup knobs, and is easy to implement with no black box information. The GGA divides the multidimensional domain (d) of the design parameters into equal multidimensional cubes where the axis of each parameter is divided into n equal segments.

The center of each of the n^d cubes is then used as the initial design for the optimization technique that uses the classical gradient ascent method. At the end of this step, the n^d local optimum designs are obtained and the best among them are chosen as the global optimum design. Applying the ML-GGA for the case study[19] leads to an optimal design that has similar merit value as the design reported by their study.

This repeatable optimum design was obtained by setting the value of n to 2, which requires $2^9 = 512$ iterations as compared to 35,000 iterations for the case of the Rmalschains. Figure 2 shows that the optimum designs from five runs are the same.

Extension of Variable Domain

The optimum designs reported[19] and the best designs obtained in this work have some design variables residing on or near the boundaries set by the predetermined limits. These variables are the number of nNoz, the Tivc, and the TNA. Extending the design parameters range outside their initial preset limits, which could potentially lead to better performance. To demonstrate this, the ML-GGA using the case study[19] is repeated by allowing a 10% extension of the design parameters around their upper and lower limits. Only a 10% margin is used here so that the predictability of the ML is still acceptable, and within the feasible design space. The normalized values of the top five designs are presented in Fig. 3.

For reference, we have also included the predicted indicated specific fuel consumption (ISFC) and merit value by the ML where good predictability — within less than 0.5% — is achieved. The best ML-GA and CFD-GA results[19] are also shown in Fig. 3. All five optimum designs have slightly higher merit values than that of Moiz et al. (2018)[19] with extended ranges. In fact, design 1 has an ISFC that is 0.14% better than the best reported[19].

Similarly, the engine output parameters such as emissions, maximum pressure rise rate (MPRR), and

Fig. 3 *The normalized values of the top five designs from the ML-GGA method with extended limits. The ML-GA design and best CFD taken from Moiz et al. (2018)[19] are also shown.*

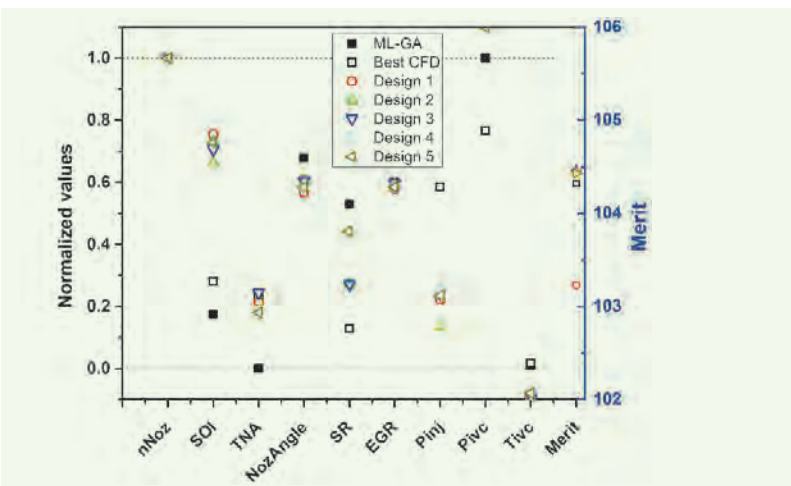

maximum pressure (P_{max}), are better from the ML-GGA and CFD_{MLGGA} compared to those reported[19]. Around 10% reductions in soot and nitric oxides (NOx) were obtained from the new simulations. The design parameters that were at their predetermined limits, such as the Tivc and Pivc, are now residing at the edge of the extended ranges (-0.1 and -1.1), suggesting that further extensions are potentially favorable to obtain higher merit values. Although, a more than 10% extension of the training data space could lead to poor prediction capability of the ML.

Post-Processing and Robustness

An additional enhancement of the ML-GGA technique is to take advantage of the ML algorithm for fast qualification of the optimal design in terms of robustness. In many cases, the optimum design is not unique and the optimization process produces multiple optimum designs with similar merit values. The challenge then is to further assess these results and eventually come up with a selection criterion.

For engines, the main criterion that a proposed design should offer is robustness. A robust design is a design that will not rapidly deteriorate and lose its merit value once its design parameters experience small perturbations. Multiple reasons can cause perturbations in the design variables. Experimental uncertainties are the main factors for variations in the design variables. Intentional perturbations to the design variables to prevent engine output parameters such as MPRR, P_{max}, soot, and NOx emissions from hitting their design or regulated limits, can be another factor. To prevent the engine performance from significantly deteriorating, a robustness parameter is defined here to evaluate the sensitivity of the merit value on the design parameters.

First, the permitted perturbation ranges of the design variables are defined. Subsequently, a new optimization problem can be initiated where the objective is to minimize the merit function, such that the search space is confined around the optimum design within some perturbation radius. The top five local optimum designs are first saved. Afterwards, a sensitivity analysis is used to evaluate the robustness of each of the designs.

The sensitivity is performed by looking for the worst design in the vicinity of each local optimum design. The vicinity space is defined as the multidimensional sphere centered around the local optimum design, and with a radius equal to the percentage of the deterioration rate. Here, we used the Rmalschains to discover the vicinity space of each of the top five designs. The utilization of a grid gradient descent scheme in the vicinity of each of the best designs would also be possible.

The comparison is reported in Fig. 4. It is clear that design 2 is more robust than the other designs.

Piston Bowl Optimization

The engine performance is more dependent on piston bowl geometry at the high-load conditions compared to low-loads, and therefore, the piston bowl optimization process was performed at high-load conditions. The optimization process was performed for CR 18:1 pistons. Table 2 is a list of the conditions at which the optimization process was performed.

The optimization process was performed in two stages. The first was a DoE optimization where the piston bowl was characterized using several design variables and a commercial software was utilized to create the

Fig. 4 *A comparison of the robustness of the five local optimum designs.*

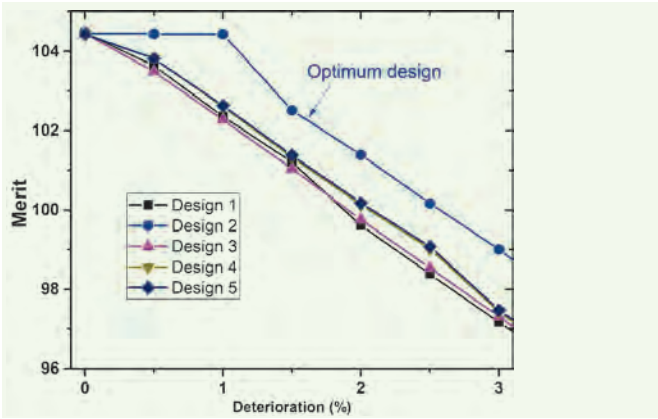

Table 2 *A list of the conditions at which the high-load piston bowl optimization process was performed.*

Load (bar IMEP)	20
CR	17:1
Engine speed (RPM)	1,500
IVC pressure (bar)	2.7
IVC temperature (K)	377
SOI (CAD aTDC)	-3 to 3
Injected mass (mg/cycle)	66
Global equivalence ratio	0.69
Split ratio	0.25
Spray angle (°)	130
Spray plume angle (°)	15
nNoz	10
Nozzle diameter (μm)	165
Pinj (bar)	500
Fuel temperature (K)	363
EGR level (%)	0
T_{liner} (K)	465
T_{head} (K)	465
T_{piston} (K)	515

cases, which were then solved using a commercial CFD code. This optimization process is referred to as CFD-DoE in the remainder of this article. The second stage builds upon the first one, and ML-GGA was used to further optimize the piston bowl geometry. The optimization process was performed for only one SOI (0 CAD aTDC).

The design object of this study was an axisymmetric piston bowl. Therefore, the geometry can be generated simply as a surface of revolution from a parameterized profile.

Figure 5 shows the piston profile shape with the defined design parameters. The two most important geometric features of the piston bowl profile is the so-called "lip" and "pip." The lip determines how the spray from the injector is broken up into separate streams, and how mixing and combustion take place. The pip directly affects the heat losses because it determines the vicinity of the spray and flame to the piston surface. The vertical and radial positions of the lip are controlled by the parameters *lipDepth* and *lipRadius*, respectively, while the sharpness is controlled by the parameter *lipCircleRadius*.

Starting from the lip, the rest of the piston bowl profile is developed in both directions. An "orbit" is generated around the lip circle, with a radius resulting from the sum of the *lipCircleRadius*, the *bowlRadius*, and the distance between the two, *deltaRadius*. The center of the piston bowl radius is placed onto this orbit at a position determined by the parameter *lipAngle*. An initial straight tangential connection is created between the pip (height controlled by the parameter *centerDepth*) and the piston bowl radius, which can then be angled upwards with the parameter *slopeAngle*. To the right of the lip, a parameter referred to as *rampRadiusRel. Pos.* determines the length of the ramp that leads up to the piston crown.

The DoE study was run in CAESES using a Sobol sequence. Since the simulations were run on a supercomputer, CAESES did not directly trigger the computations, but rather generated a library of 128 design variants for each CR with the corresponding CFD input files that were subsequently moved to and executed on Mira. Once all the results were available, they were compiled and evaluated using a merit function, Eqn. 1:

$$Merit = 100 - \left(\frac{wf_1 \times \frac{ISFC - limit}{limit - min(ISFC)} + wf_2 \times f(P^*_{max}) + wf_3 \times f(MPRR^*) + wf_4 \times f(FSN^*) + wf_5 \times f(sNOx^*) + wf_6 \times f(sHC^*) + wf_7 \times f(sCO^*)}{\sum_{i=1}^{7} wf_i} \right) \quad (1)$$

with

$$f(Parameter^*) = \begin{cases} \frac{Parameter - limit}{Limit - \min(parameter)} - 1, & if\ Parameter > Limit \\ 0, & if\ Parameter \leq Limit \end{cases} \quad (2)$$

where the limits of the various parameters and the wf_i are summarized in Table 3. The objective here is to minimize ISFC through maximizing the merit function. Here, the merit is penalized when the other engine parameters and emissions exceed the predefined limits. The ISFC limit is taken as an average of the values from all CFD simulations. The MPRR and P_{max} limits are specific to the engine hardware used in the current work. The emissions limits were obtained from the benchmarking data of a BMW N47 diesel

Table 3 *The limits of various parameters and the wf_i used for the merit function calculation.*

Parameter	Limit	wf_i
ISFC (g/kWh)	205	100
P_{max} (bar)	200	100
MPRR (bar/CAD)	10	10
FSN	1.5	1
sNOx (g/kWh)	7.9	1
sHC (g/kWh)	0.052	1
sCO (g/kWh)	9.4	1

Fig. 5 *Piston bowl profile with design parameters.*

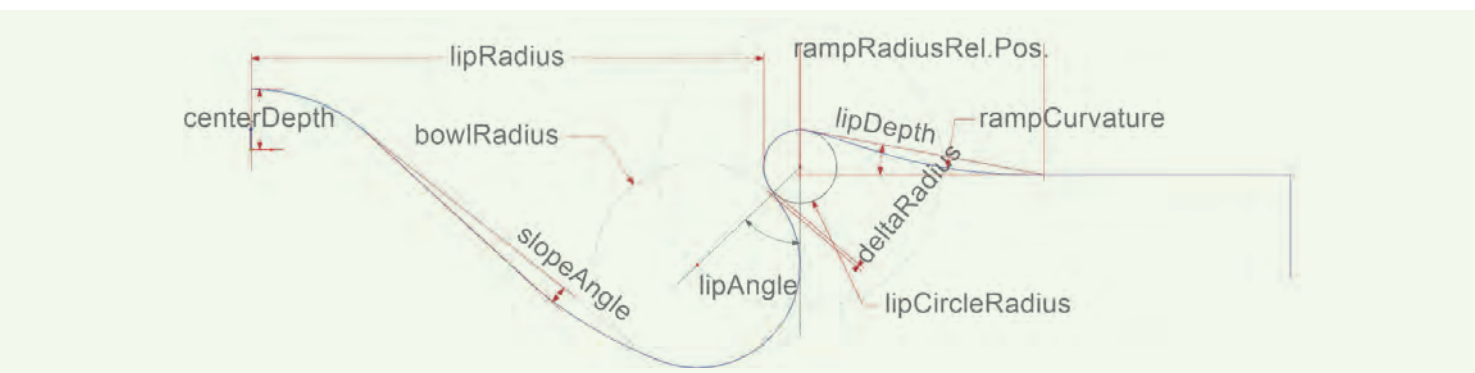

engine at this high-load operating point.

Figure 6 shows the piston bowl geometry profiles for the 128 CR 18:1 design candidates, which were created. The thin pink lines represent each of the individual designs and the thickened solid lines show three example designs. It can be seen that a wide-ranging design space was enabled without producing infeasible or difficult-to-fabricate variants.

The 128 CR 18:1 piston designs were simulated on Mira using the 20 bar indicated mean effective pressure (IMEP) conditions. Equation 2, along with the wf_i and limits shown in Table 3, were used to evaluate the performance and emissions of the engine. Figure 7 shows the top five CR 18:1 CFD-DoE piston designs along with the baseline piston E, and the engine performance parameters and emissions are presented in Table 4. The top five optimized designs perform significantly better than the baseline piston. ISFC savings up to 14% were obtained.

Regarding the emissions, significant reductions in the filter smoke number (FSN) (63%), specific hydrocarbon (sHC) (81%), and specific carbon monoxide (sCO) (92%) were achieved through this optimization process. In addition, specific NOx (sNOx) reductions up to 7.9% were also obtained here. Combining all the savings and reductions together, the merit values of the top five designs are significantly higher than the baseline one. Note that the merit values are mostly negative. This is due to the ISFC limit used in Eqn. 2.

The ISFC limit of 205 g/kWh combined with the relatively higher ISFC values of the CR 18:1 cases result in a negative merit function. This does not change any of the findings and conclusions reported here because the merit function is only used to sort the designs out. In fact, four different definitions of the merit function were tested in this work and they all resulted in the same order of the top 23 designs (not shown here).

As expected, the top five designs share some high-level characteristics such as the narrower piston bowl (smaller *lipRadius*) and lower center height (*centerDepth*). The best CFD-DoE design, D28, has a relatively higher *centerDepth*, however, it has a steeper slope, which pushes the piston surface away from the spray and flame. The heat losses, and the fuel and air mixing are the two main factors leading to the significant reductions in fuel consumption and emissions.

The ML-GGA approach was used here to further

Fig. 6 *The piston bowl geometry profiles for the 128 CR 18:1 design candidates.*

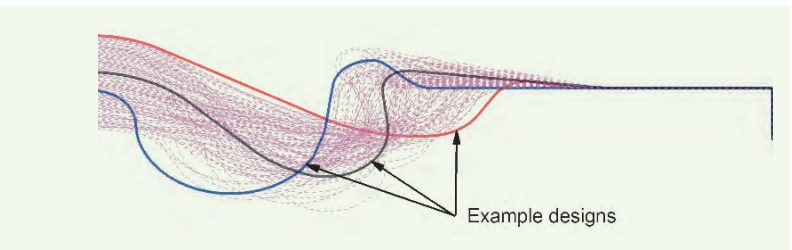

Fig. 7 *The top five CR 18:1 CFD-DoE piston designs along with the baseline piston E.*

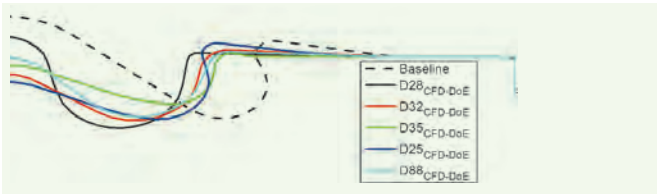

Table 4 *The engine performance results, parameters, and emissions for the top five CR 18:1 CFD-DoE and baseline piston E designs.*

	Baseline	CFD-DoE				
		D28	**D32**	**D35**	**D25**	**D88**
Merit	-2,116.63	65.14	-21.25	-21.29	-21.85	-48.54
ISFC (g/kWh)	239.01	205.53	206.86	206.86	206.87	207.28
ISFC saving (%)		14.01	13.45	13.45	13.45	13.28
MPRR (bar/CAD)	6.48	5.87	5.88	5.89	5.88	5.88
P_{max} (bar)	176.3	171.8	172.7	174.0	172.7	173.0
CA50 (CAD aTDC)	14.11	18.06	18.17	18.05	18.14	18.06
FSN	2.47	0.95	0.93	0.965	0.91	0.91
sNOx (g/kWh)	4.73	4.65	4.42	4.36	4.61	4.39
sHC (g/kWh)	11.53	2.15	2.50	2.66	2.24	2.61
sCO (g/kWh)	67.64	5.28	5.78	7.76	5.01	6.07

Fig. 8 *The utilized ML-GGA piston bowl geometry optimization scheme.*

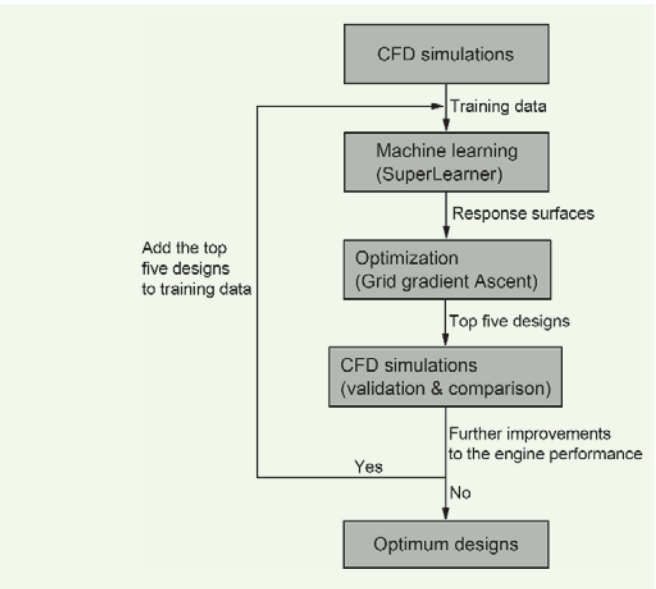

Fig. 9 *Top five performing CR 18:1 ML-GGA piston designs. The baseline E and the best ML-DoE D28 piston designs are also shown.*

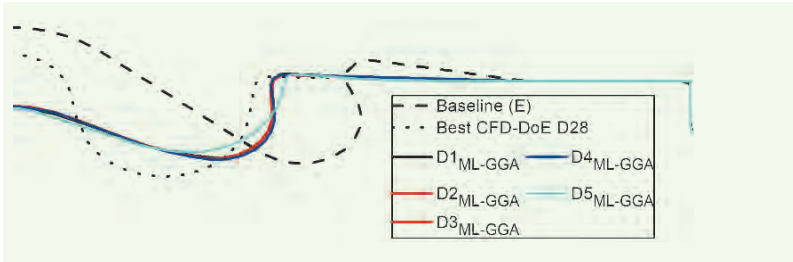

optimize the CR 17:1 and CR 18:1 piston geometries. Figure 8 shows the ML-GGA piston bowl geometry optimization scheme utilized. The CFD results from the CFD-DoE optimization were used here as the initial training data set for the ML model. The SuperLearner approach[20] was chosen to construct the relationships between the piston design variables and the engine output parameters. The SuperLearner approach calculates the optimal combination of a pool of prediction algorithms, such as the arithmetic mean (SL.mean), Lasso and Elastic-Net Regularized Generalized Linear Models (SL.gmlnet), Breiman and Cutler's Random Forests for Classification and Regression (SL.randomForest), support vector machines (SL.svm), extreme gradient boosting (Xgboost), linear regression models (SL.lm), Feed-Forward Neural Networks and Multinomial Log-Linear Models (SL.nnet). The optimal combination is a set of these multiple models with wf_i that minimize the cross-validated error.

The 128 piston designs mentioned earlier were used as initial training data for the ML model. For CR 18:1 ML-GGA optimization, four iterations were needed to obtain a converging solution, therefore, 20 additional designs were added to the training data set. The added designs all had high merit values and their addition

Table 5 *Performance results for the top five CR 18:1 ML-GGA, best CFD-DoE and baseline piston designs.*

	Baseline	Best CFD-DoE	ML-GGA				
		D28	D1	D2	D3	D4	D5
Merit	-2,116.63	65.14	172.20	161.82	139.10	128.71	98.20
ISFC (g/kWh)	239.01	205.53	203.88	204.04	204.39	204.55	205.02
ISFC saving (%) from baseline	—	14.01	14.70	14.63	14.48	14.42	14.22
ISFC saving (%) from best CFD-DoE D28	—	—	0.80	0.72	0.55	0.48	0.25
MPRR (bar/CAD)	6.48	5.87	5.88	5.87	5.87	5.88	5.88
P_{max} (bar)	176.3	171.8	173.1	172.8	172.8	172.8	173.1
CA50 (CAD aTDC)	14.11	18.06	17.60	17.73	17.74	17.72	17.60
FSN	2.47	0.95	0.91	0.87	0.87	0.88	0.95
sNOx (g/kWh)	4.73	4.65	4.72	4.72	4.72	4.70	4.76
sHC (g/kWh)	11.53	2.15	2.29	2.26	2.29	2.31	2.34
sCO (g/kWh)	67.64	5.28	5.99	5.11	5.00	5.19	6.82

Fig. 10 *The breakdown of ISFC savings with respect to the optimization method for the CR 18:1 piston geometries.*

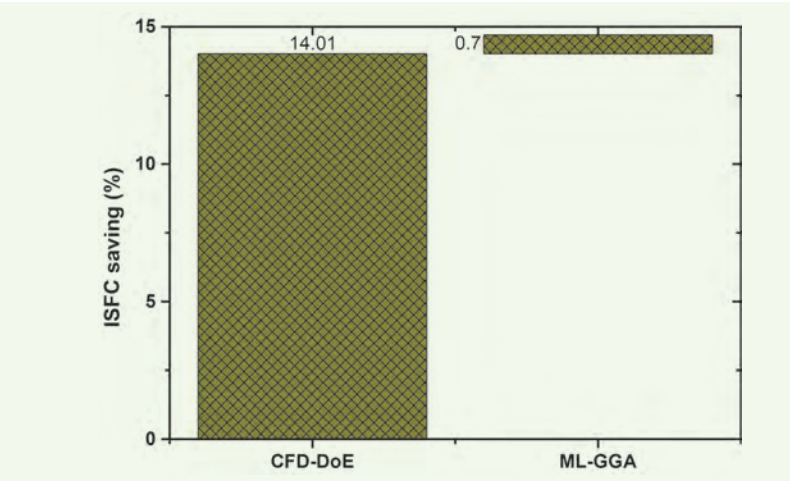

significantly improved the predictions at the regions where the optimum designs are.

Figure 9 shows the top five CR 18:1 ML-GGA piston designs along with the baseline E, and the best ML-DoE D28 pistons. The engine output parameters and merit values for these designs are presented in Table 5. The top four ML-GGA designs are very similar with minor differences in the piston bowl and center regions. Only $D5_{ML\text{-}GGA}$ has a slightly different profile. The top five designs have piston profiles that are different than the best CFD-DoE design. This is because there was a noticeable variation between the top five CFD-DoE designs, and ML-GGA fine-tuned the design parameters within the range covered by the top CFD-DoE designs. As a result, an additional 0.8% savings in ISFC was obtained from this optimization process.

In summary, substantial savings in ISFC and emissions with the optimized pistons compared to the baseline pistons were observed. Two optimization methods were used in this work and each resulted in different improvements to the engine performance. Here, a breakdown of the ISFC improvements with regard to the optimization method is performed. The ISFC improvements were calculated with respect to the worst design for each CR (piston E for CR 18:1). The cumulative ISFC savings for CR 18:1 was 14.7%.

Figure 10 shows the breakdown of ISFC savings with respect to the optimization method for the CR 18:1 piston geometries. As can be seen, the improvement in ISFC is mainly during the CFD-DoE optimization phase while the lowest contribution is for ML-GGA. This is expected because there was not much room for improvement after the CFD-DoE optimization. The additional ISFC savings from ML-GGA were obtained in a relatively short time compared to the CFD-DoE optimization process. The best performing CR 17:1 ($D1_{ML\text{-}GGA}$) and 18:1 ($D2_{ML\text{-}GGA}$) pistons are now being manufactured and will be tested once available. The findings will be reported in future articles.

Conclusions

In this work, a methodical approach for tackling engine optimization problems using ML is presented. Critical precautions, recommended algorithms and suitable optimization techniques are discussed. In addition, the combustion system of a light-duty GCI engine running on a market gasoline fuel with a RON of 91 was optimized using CFD and ML.

The focus of this study was to optimize the piston bowl geometry at CR 18:1 and this exercise was carried out at full load conditions (22 bar IMEP). The main findings from this work are summarized as:

1. First, a CFD-DoE optimization was completed where 128 piston bowl designs were evaluated. This optimization process yielded 14% improvements in the ISFC.
2. Afterward, an ML-GGA approach was utilized to further optimize the piston bowl design resulting in an additional 0.8% savings in the ISFC.
3. This two-step optimization exercise yielded significant improvements in the engine performance and emissions compared to the baseline piston bowl designs. The optimized piston bowl geometries produced significantly lower emissions compared to the baseline. Reductions in CO emissions up to 95% were obtained. Also, 85% and 70% reductions in hydrocarbon and soot emissions, respectively, were achieved from this optimization exercise.

Acknowledgments

The authors would like to acknowledge the funding support from the Fuel Technology Division at Saudi Aramco's R&DC.

Part of this work was presented at the ASME Internal Combustion Engine Fall Technical Meeting, Chicago, Illinois, October 21-23, 2019.

References

1. ExxonMobil: *Outlook for Energy: A View to 2040*, ExxonMobil: Texas, 2018.
2. Capuano, L.: *International Energy Outlook 2018,* U.S. Energy Information Administration Report, July 24, 2018, Washington, D.C., 21 p.
3. Kalghatgi, G.T.: "The Outlook for Fuels for Internal Combustion Engines," *International Journal of Engine Research*, Vol. 15, Issue 4, May 2014, pp. 383-398.
4. Kesgin, U.: "Genetic Algorithm and Artificial Neural Network for Engine Optimization of Efficiency and NOx Emission," *Fuel*, Vol. 83, Issues 7-8, May 2004, pp. 885-895.
5. Gen, M. and Cheng, R.: *Genetic Algorithms and Engineering Optimization*, 1st edition, John Wiley & Sons Inc., 2000, 512 p.
6. Manolas, D.A., Frangopoulos, C.A., Gialamas, T.P. and Tsahalis, D.T.: "Operation Optimization of an Industrial Cogeneration System by a Genetic Algorithm," *Energy Conversion and Management*, Vol. 38, Issues 15-17, October-November 1997, pp. 1625-1636.
7. Wong, K.I., Wong, P.K., Cheung. C.S. and Vong, C.M.: "Modeling and Optimization of Biodiesel Engine Performance Using Advanced Machine Learning Methods," *Energy*, Vol. 55, June 2013, pp. 519-528.

8. Probst, D.M., Senecal, P.K., Qian, P.Z., Xu, M.X., et al.: "Optimization and Uncertainty Analysis of a Diesel Engine Operating Point Using Computational Fluid Dynamics," *Journal of Engineering for Gas Turbines and Power*, Vol. 140, Issue 10, June 2018, pp. 102806-102815.

9. Bertram, A.M., Zhang, Q. and Kong, S-C.: "A Novel Particle Swarm and Genetic Algorithm Hybrid Method for Diesel Engine Performance Optimization," *International Journal of Engine Research*, Vol. 17, Issue 7, October 2015, pp. 732-747.

10. Zhang, Q., Ogren, R.M. and Kong, S-C.: "A Comparative Study of Biodiesel Engine Performance Optimization Using Enhanced Hybrid PSO-GA and Basic GA," *Applied Energy*, Vol. 165, March 2016, pp. 676-684.

11. Samadani, E., Shamekhi, A.H., Behroozi, M. and Chini, R.: "A Method for Pre-Calibration of DI Diesel Engine Emissions and Performance Using Neural Network and Multi-Objective Genetic Algorithm," *Iranian Journal of Chemistry and Chemical Engineering*, Vol. 28, Issue 4, December 2009, pp. 61-70.

12. Vaughan, A. and Bohac, S.V.: "A Cycle-to-Cycle Method to Predict HCCI Combustion Phasing," paper presented at the ASME 2013 Internal Combustion Engine Division Fall Technical Conference, Dearborn, Michigan, October 13-16, 2013.

13. Krijnsen, H.C., van Leeuwen, J.C., Bakker, R., van der Bleek, C.M., et al.: "Optimum NOx Abatement in Diesel Exhaust Using Inferential Feedforward Reductant Control," *Fuel*, Vol. 80, Issue 7, May 2001, pp. 1001-1008.

14. Malikopoulos, A.A., Assanis, D.N. and Papalambros, P.Y.: "Real-Time Self-Learning Optimization of Diesel Engine Calibration," *Journal of Engineering for Gas Turbines and Power*, Vol. 131, Issue 2, March 2009, pp. 022803-1 to 022803-7.

15. de Lucas, A., Duran, A., Carmona, M. and Lapuerta, M.: "Modeling Diesel Particulate Emissions with Neural Networks," *Fuel*, Vol. 80, Issue 4, March 2001, pp. 539-548.

16. Orfila, O., St. Pierre, G. and Messias, M.: "An Android-based Ecodriving Assistance System to Improve Safety and Efficiency of Internal Combustion Engine Passenger Cars," *Transportation Research Part C: Emerging Technologies*, Vol. 58, Part D, September 2015, pp. 772-782.

17. Bergmeir, P., Nitsche, C., Nonnast, J., Bargende, M., et al.: "Using Balanced Random Forests on Load Spectrum Data for Classifying Component Failures of a Hybrid Electric Vehicle Fleet," paper presented at the 13th International Conference on Machine Learning and Applications, Detroit, Michigan, December 3-6, 2014.

18. Rychetsky, M., Ortmann, S. and Glesner, M.: "Support Vector Approaches for Engine Knock Detection," paper presented at the International Joint Conference on Neural Networks, Washington, D.C., July 10-16, 1999.

19. Moiz, A.A., Pal, P., Probst, D.M., Pei, Y., et al.: "A Machine Learning-Genetic Algorithm (ML-GA) Approach for Rapid Optimization Using High-Performance Computing," *SAE International Journal of Commercial Vehicles*, Vol. 11, Issue 5, 2018, pp. 291-306.

20. Polley, E.C. and van der Laan, M.J.: "Super Learner in Prediction," *U.C. Berkeley Division of Biostatistics Working Paper Series*, Working Paper 266, May 2010.

21. Hanson, R., Curran, S., Wagner, R., Kokjohn, S., et al.: "Piston Bowl Optimization for RCCI Combustion in a Light-Duty Multi-Cylinder Engine," *SAE International Journal of Engines*, Vol. 5, Issue 2, 2012, pp. 286-299.

22. Wickman, D.D., Senecal, P.K. and Reitz, R.D.: "Diesel Engine Combustion Chamber Geometry Optimization Using Genetic Algorithms and Multidimensional Spray and Combustion Modeling," paper presented at the SAE World Congress Conference, Detroit, Michigan, March 5-8, 2001.

23. Polley, E.C., LeDell, E., Kennedy, C., Lendle, S., et al.: "Package 'SuperLearner'," 2018, 64 p., *https://cran.r-project.org/web/packages/SuperLearner/ SuperLearner.pdf*.

24. Bergmeir, C.N., Molina Cabrera, D. and Benítez Sánchez, J.M.: "Memetic Algorithms with Local Search Chains in R: The Rmalschains Package," *Journal of Statistical Software*, Vol. 75, Issue 4, December 2016, pp. 1-33.

25. Badra, J.A., Khaled, F., Tang, M., Pei, Y., et al.: "Engine Combustion System Optimization Using CFD and Machine Learning: A Methodological Approach," paper ICEF2019-7238, presented at the ASME Internal Combustion Engine Division Fall Technical Conference, Chicago, Illinois, October 20-23, 2019.

About the Authors

Dr. Jihad A. Badra

Ph.D. in Combustion Research in Mechanical Engineering, University of Sydney

Dr. Jihad A. Badra is the Engine Combustion Team Leader working in the Fuel Technology Division of Saudi Aramco's Research and Development Center. He joined Saudi Aramco in 2014 after working as a Postdoctoral Researcher in the Clean Combustion Research Center at King Abdullah University of Science and Technology (KAUST).

Jihad's research interest is in developing and optimizing internal combustion engine technologies with decreased net environmental impact. His current focus is on fuel formulation for advanced engines and engine modeling using computational fluid dynamics.

Jihad has authored or coauthored more than 50 peer-reviewed journal papers.

He received his B.S. degree in Mechanical Engineering from the University of Balamand, El-Koura, Lebanon, and his M.S. and Ph.D. degrees in Combustion Research in Mechanical Engineering from the University of Sydney, Sydney, Australia.

Dr. Fethi Khaled

Ph.D. in Mechanical Engineering, King Abdullah University of Science and Technology

Dr. Fethi Khaled is currently a Postdoctoral Fellow at the Université d'Orléans in Orleans, France, where he is studying the knock and pre-ignition propensity of hydrocarbons in the idealized rapid compression machine.

During his Ph.D. studies, Fethi's interests included the study of the fundamental kinetic properties of hydrocarbons that are relevant in todays' advanced combustion engines. In 2018, he attended a summer internship at Saudi Aramco, where Fethi had the opportunity to contribute in this work.

In 2013, he received his B.E. degree in Polytechnic Science from the Ecole Polytechnique de Tunisie, Carthage, Tunisia. In 2014, Fethi received his M.S. degree in Mechanical Engineering, and in 2018, he received his Ph.D. degree in Mechanical Engineering, both from King Abdullah University of Science and Technology (KAUST).

Dr. Meng Tang

Ph.D. in Mechanical Engineering-Engineering Mechanics, Michigan Technological University

Dr. Meng Tang is a Technical Specialist working with the Commercial Transport Research Team at the Aramco Americas (formally Aramco Services Company), Aramco Research Center-Detroit. His work includes investigating heavy-duty engine combustion and spray characteristics, and performing engine and fuels co-optimization using computational fluid dynamics simulations on high performance computing platforms.

Meng received his Ph.D. degree in Mechanical Engineering-Engineering Mechanics from Michigan Technological University, Houghton, MI, where he conducted research on the fundamental aspects of alternative fuel combustion using an optically accessible combustion vessel.

Dr. Yuanjiang Pei

Ph.D. in Mechanical Engineering, University of New South Wales

Dr. Yuanjiang Pei is a Technical Specialist at the Aramco Americas (formally Aramco Services Company (ASC)), Aramco Research Center-Detroit. He is currently working on the co-optimization of fuels and engines in pursuit of higher internal combustion engine efficiency.

Pei has more than 10 years of experience working in the engine research and automotive industry. He joined ASC in late 2015 after previously working more than 2 years on engine combustion modeling at Argonne National Laboratory, and 5 years on engine management system calibration and project management at Delphi.

Pei is actively involved in the organization of several international conferences, including the Society of Automotive Engineers (SAE) World Congress, the American Society of Mechanical Engineers (ASME) – Internal Combustion Engine Fall (ICEF) Conference, and the Engine Combustion Network (ECN) workshops. He also serves as a technical reviewer for numerous projects and journals.

Pei has authored more than 60 journal and peer-reviewed conference papers with more than 1,100 citations. He was recently presented the 2019 HPCwire Editors' Choice Award in the Best Use of High Performance Computing in Automotive, and the 2019 ASME Chairman's Distinguished Service Award for his research excellence.

Pei received his B.S. and M.S. degrees in Mechanical Engineering from Tianjin University, Tianjin, China. He received his Ph.D. degree in Mechanical Engineering from the University of New South Wales, Sydney, Australia. For his Ph.D. research, Pei received the Australian Leadership Award.

Dr. Janardhan Kodavasal

Ph.D. in Mechanical Engineering, University of Michigan

Dr. Janardhan Kodavasal is a Group Leader within the Advanced Systems Integration at Cummins Inc. located in Columbus, IN, where he manages a team of engineers supporting various engine programs. Janardhan also leads combustion, performance, and emissions development for Cummins' future medium-duty and heavy-duty products targeting low nitrogen oxides and carbon dioxide.

Prior to joining Cummins in 2018, he worked at the Argonne National Laboratory as a scientist where he initiated and led Argonne's efforts to apply machine learning to accelerate product development. Janardhan also led efforts to apply computational fluid dynamics and supercomputing to engine design.

He has published more than 25 journal and conference articles, which have been cited over 350 times. Janardhan is active in the Society of Automotive Engineers (SAE) and routinely chairs advanced combustion sessions focusing on topics such as partially premixed combustion ignition and homogeneous charge compression ignition.

He received his B.S degree Mechanical Engineering from the National Institute of Technology Karnataka, Surathkal, India. Janardhan received two M.S. degrees, one in Aerospace Engineering and the other in Mechanical Engineering from the University of Michigan, Ann Arbor, MI.

In 2013, he received his Ph.D. degree in Mechanical Engineering, focusing on advanced combustion, from the University of Michigan, Ann Arbor, MI. During his Ph.D. research, Janardhan worked at Lawrence Livermore National Laboratory in California, as well as at Bosch Gasoline Systems in Detroit.

Dr. Pinaki Pal

Ph.D. in Mechanical Engineering, University of Michigan

Dr. Pinaki Pal is a Research Scientist in the Energy Systems division at Argonne National Laboratory, Lemont, IL. His expertise lies in the areas of turbulent combustion modeling, computational fluid dynamics (CFD), machine learning, reduced order modeling, and high performance computing.

Pinaki's current research interests are detonation engines, abnormal combustion (knock, cyclic variability) in spark ignition engines, fuel engine interactions and co-optimization, alternative fuels, low temperature combustion, and nanoparticle synthesis.

He received his B.Tech degree in Mechanical Engineering from the Indian Institute of Technology, Kharagpur, India. Before joining Argonne, Pinaki received his Ph.D. degree in Mechanical Engineering from the University of Michigan, Ann Arbor, MI, with a specialization in turbulent combustion modeling and CFD for low temperature combustion applications in both internal combustion and gas turbine engines.

Dr. Opeoluwa Owoyele

Ph.D. in Mechanical Engineering, North Carolina State University

Dr. Opeoluwa Owoyele is a Postdoctoral Appointee in the Multiphysics Computations section within the Energy Systems division at Argonne National Laboratory, Lemont, IL. His research expertise involves the identification of lower dimensional manifolds to accelerate turbulent combustion simulations and the use of machine learning methods to develop predictive models and accelerate design optimization.

Opeoluwa's current research at Argonne entails the use of computational fluid dynamics, machine learning and active learning to accelerate the design optimization of internal combustion engines and the development of predictive models for turbulent combustion modeling using ensemble deep learning methods.

Before joining Argonne, he was part of the ORISE postgraduate program at the National Energy Technology Laboratory, Pittsburgh, PA, where he developed deep convolutional neural networks to obtain improved convergence of the pressure field in multiphase flow systems.

Opeoluwa received his Ph.D. degree in Mechanical Engineering from North Carolina State University, Raleigh, NC. His Ph.D. dissertation was focused on the simulation turbulent combustion in lower dimensional manifolds using principal component analysis.

Carsten Fütterer

M.S. in Energy and Process Engineering, Technical University of Berlin

Carsten Fütterer is a Computer Aided Engineering Applications Engineer at Friendship Systems AG, having been there since 2015. His main focus is the automotive and turbomachinery industry, where he supports customers creating high fidelity parametric geometry models, and assists during their optimization.

While working on his bachelor's thesis, Carsten had his first experience with computational fluid dynamics (CFD), while studying the fluid flow behavior of mixing vessels in biogas plants. At the beginning of his studies for his master's degree, Carsten studied one year abroad at the Queensland University of Technology in Australia. Back in Germany, he did an internship at CD-Adapco in Nürnberg, where he extended his CFD skills.

Carsten received his B.S. and M.S. degrees in Energy and Process Engineering from the Technical University of Berlin, Berlin, Germany. For his M.S. thesis, Carsten simulated the fluid flow in fixed bed reactors, including conjugate heat transfer and detailed reactions.

Mattia Brenner

M.S. in Naval Architecture and Ocean Engineering, Technical University of Berlin

Mattia Brenner is in charge of technical sales and business development at Friendship Systems AG. He joined the company in 2008, starting his career in the Engineering Department, working primarily on the optimization of ship hulls for better operational behavior and reduced fuel consumption.

After spending several years focused on customer support and research projects, including new — nonmaritime — applications, Mattia transitioned to his current role in business development.

In 2008, he received his M.S. degree in Naval Architecture and Ocean Engineering, from the Technical University Berlin, Berlin, Germany.

Dr. Aamir Farooq

Ph.D. in Mechanical Engineering, Stanford University

Dr. Aamir Farooq became an Assistant Professor at King Abdullah University of Science and Technology (KAUST), Thuwal, Saudi Arabia, in 2010. He later became an Associate Professor in 2016. Aamir is the principal investigator of the Chemical Kinetics and Laser Sensors Laboratory in the Clean Combustion Research Center at KAUST.

His research interests are in the areas of energy, chemical kinetics, spectroscopy, and laser-based sensors. Aamir's group carries out experimental chemical kinetics research using shock tubes, a rapid compression machine, and optical diagnostics.

He has worked extensively on novel spectroscopic strategies to develop optical sensors based on mid-infrared quantum cascade lasers for chemical, biomedical, and environment monitoring applications.

Aamir has authored over 100 refereed journal articles and has given invited talks at a number of international conferences. Recently, he was awarded the prestigious Hiroshi Tsuji Early Career Research Award by Elsevier and the Combustion Institute.

In 2010, Aamir received his Ph.D. degree in Mechanical Engineering from Stanford University, Stanford, CA.

Dr. Junseok Chang

Ph.D. in Mechanical Engineering, University of Michigan

Dr. Junseok Chang is a Science Specialist working in the Fuel Technology Division of Saudi Aramco's Research and Development Center, where he is currently a Team Leader of the Engine Combustion Team. Junseok manages a wide spectrum of fuel and engine programs from their early noble idea with basic research providers to their high readiness level technology demonstrations with multiple OEMs.

His research focuses on developing an advanced fuel engine system that helps to reduce wheel-to-wheel CO_2 emissions and provide an improved carbon footprint. Junseok has spent his entire career — 20 plus years — in the field of internal combustion engines, advanced fuel, and sustainable energy strategy development by use of extensive basic and applied research projects.

Prior to joining Saudi Aramco, he worked for General Motors' Research & Development Center, where he worked to develop GM's next generation lean burn engines and valve train systems. Junseok also worked with the startup company Transonic Combustion, which makes novel fuel injectors and fuel reformers. His main interest is to deploy an innovative research idea into the practical mobility solution in the transport sector by bridging the gap between physics and engineering.

Junseok was academically trained in the thermo-science and heat transfer of the internal combustion engine.

In 1999, he received his M.S. degree from Seoul National University, Seoul, Korea, and in 2004, Junseok received his Ph.D. degree in Mechanical Engineering from the University of Michigan, Ann Arbor, MI.

Reservoir Simulation Well Data Exchange toward Digital Transformation and Live Earth Models

Menhal A. Al-Ismael, Dr. Ali A. Al-Turki, and Abdulaziz M. Al-Darrab

Abstract / Automatic updates of simulation models with historical field performance and events are challenging and time-consuming tasks that reservoir engineers need to tackle, whether it is to maintain history matched reservoir models (evergreen assets), undertake a new calibration exercise, or update forecasting studies. The challenge takes another dimension with increasing complexity of field operations (production, injection, drilling, and workover), and well designs and configuration of downhole equipment.

This article presents an efficient workflow capitalizing on the Fourth Industrial Revolution digital twin principles to automate the process of seamlessly integrating and updating historical wells' information in reservoir simulation models. The objective of this workflow is to drive reservoir simulation toward capitalizing on digital transformation and the live Earth models' concept to revolutionize model calibration and history matching for superior quality of prediction with great confidence.

Well data digitization in this workflow was achieved through automating well data acquisition, well data quality control (QC) enforcement, and well modeling in interconnected simulation applications. The workflow minimizes human manual interaction with data, giving engineers the chance to focus more on reservoir engineering aspects of their given tasks.

The workflow consists of four steps. The first step is data acquisition in which various types of well data are collected. The second step is data QC in which data from different data sources is subjected to engineering and scientific measures, i.e., quality indices, which translate engineering knowledge and experience to detect possible data inconsistencies. The third and fourth steps cover exporting and importing relevant data within the reservoir simulation applications' portfolio where various data types are handled and managed seamlessly.

Data and event acquisition workflows were automated to provide seamless well data transfer between different data sources and reservoir simulation pre- and post-processing applications. The different types of well data were obtained through automatic collecting from data repositories, i.e., databases, petrophysical models, etc.

The QC procedures were automatically performed against deviation surveys, perforations, casing/tubing, flow meter, cores, formation tops and productivity/injectivity index. This helped in identifying data discrepancy, if any, including missing data entries and contradicting well events.

The automation of these workflows significantly reduced the time needed for well data transmission/update to the reservoir models, eliminated human errors associated with data entry or corrections, and helped keep the models up-to-date (evergreen). Incorporating the digital twin concepts enabled advanced automatic digitization of well information. It provided a data exchange solution that meets exploration and production requirements, and provided more effective and efficient methods of connecting diverse applications and data repositories.

Introduction

Reservoir simulation is one of the cornerstone processes in field development planning. It utilizes mathematical and physics-based formulations that describe the fluid flow behavior in oil and gas reservoirs. Reservoir engineers use reservoir simulation to understand how pressure and fluid saturations change with time to better assess development plans, along with recovery. Simulation models are built using a variety of data such as seismic, logs, fluid characteristics, petrophysical properties, etc.

In addition, historical field and well performances are crucial inputs to maintain and history match numerical reservoir simulation models. A well-executed history matched reservoir simulation model can be used to assess development scenarios, estimate recovery, and develop business plans to enable sound operational and strategic decisions. To improve the predictability of the reservoir simulation models, a greater amount of time and effort is put into data gathering and quality checking the field data, as well as model calibration

and history matching. It does not stop there; this effort continues to maintain the simulation model by updating historical data and events, such as incorporating new rates (allocations), pressure data of the existing wells, or accommodating recently drilled and completed wells.

The inclusion of recently acquired data might require reservoir engineers to re-calibrate the model or start a re-history matching effort, specifically if there is a good amount of historical data or major activities/events undertaken in the field. Therefore, maintaining the simulation model — evergreen digital replica — is an important and on-going activity that requires a lot of effort, including collecting historical data and events, incorporating the data in the existing models, and performing model calibration and history matching.

Massive amounts of well data gathered from onshore and offshore oil and gas fields are available from different data sources, which is captured one of several ways in numerical reservoir simulation models. There are many data types describing different well configurations and operational constraints, which is of key importance for building and maintaining the reservoir simulation models. Reservoir engineers working on updating or history matching large fields have to handle massive volumes of data from data gathering, quality checking, and preparing the data in the right format for different reservoir simulation processes. The challenge of integrating this amount of data in simulation models increases with the complexity of well designs and configurations as well as field operational constraints — such as conventional completion practices or advanced and smart completion technology.

Quality of historical well data is another challenge in this process, which is a major factor impacting model uncertainty. The quality of well data varies between the different data types, such as fields, measurement frequency, and workover activities. Each well's data type is collected and measured differently, where manual procedures might be involved in the process, which could potentially introduce human errors or bias.

Literature Review

Data validation and management in the oil and gas industry has been thoroughly discussed in other literature. A number of discussions have placed a focus on wells and reservoir simulation related data. Shideed (2005)[1] highlighted that different database management systems were used to store and maintain the huge volume of well data and to incorporate the latest technology for centralizing, securing, and making efficient use of the data. The gathered well data includes completion data, production/injection, workovers, perforations, casing, well tests, surveys, logs, cores, stratigraphic tops, seismic, pressure-volume-temperature, etc.

Availing this data is very important to allow engineers to perform their different activities in exploration, drilling, production and simulation. Shideed (2005)[1] also highlighted different workflows for maintaining data quality, including data entry/update forms where edit checks and rules are applied, in addition to data validations against the Oracle® dictionary. It also highlighted the challenge of data consistency, completeness, and reliability after the data entry/update phase.

Al-Ismael et al. (2014)[2] presented a system for extracting and validating well information from the data repositories for reservoir simulation purposes. The work demonstrated different quality control (QC) measures for a well's data validations and for detecting data inconsistencies. The focus was to provide one central gateway to historical well data to simplify the process of retrieving data from the data repositories. It provided the first step toward the integration between pre- and post-processing simulation applications.

Al-Ismael et al. (2014)[3] presented a well completion data adjustment workflow with the purpose of adapting a well's data for reservoir simulation applications. It focused on application customizations to support advanced or old practices of well completion. The work highlighted that having correct data is not enough for having it utilized. Moreover, another step to translate this data into the pre-processing application is required.

Al-Zahrani et al. (2015)[4] presented another workflow for guiding engineers through the QC process during the construction of the simulation models. This effort covered most of the data required for building simulation models. The presented workflow walks engineers through a set of QC steps for different data types, including well data in addition to the geological model. The workflow consists of a number of QC steps to ensure data consistency between the well's completion, and the 3D grid.

All the work discussed in these articles focus on data validation during data entry or after loading in the pre-processing applications. Subsequently, the work in this article focuses on applying additional data validation and scanning procedures before exporting for simulation purposes. It also presents an automated process for integration and updating historical wells' information in reservoir simulation models.

Engineering and Scientific Measures of Different Well Data Types

Numerical reservoir simulation encompasses different objects to form a simulation model. These different objects — rock physical properties, fluids quantities, well specifications, etc. — are obtained from different data sources in different formats with varying ranges of uncertainty. This makes it challenging to manually perform tasks, like building new reservoir simulation models or maintaining existing ones (evergreen). For this reason, different workflows are established to automate different processes for data acquisition, building, and updating simulation models.

This article focuses on historical well information, which is a critical segment in simulation modeling. Wells are the most critical and challenging asset in oil and gas simulation models in which they express the fluid production and injection, and therefore, elicit fluid dynamics within the simulation model. To describe wells in a simulation model, various types of data

are needed in which each data type provides specific measures and comes from different data sources. In addition, similar to any type of data, well data validations and QC are important, which have an impact with great significance on simulation results.

Well Data Types

Reservoir simulators require historical production and injection rates to match its numerically calculated reservoir energy, along with the historical rates from the well's and the field's performance. The simulator also requires well perforations and open hole sections discretized into the resolution of the simulation model. In addition, well events such as plugs, squeezes, and re-perforations are required to maintain the historical set of activities performed specifically on the wells, and the field in general. This kind of data describes the interaction between the wells and the reservoir, and defines entry sections for fluid to go in or out of the reservoir. This data is, usually, available in relational databases in the form of a continuous space, i.e., XYZ UTM coordinates, where X, Y, and Z define the three axes for the 3D continuous space.

Perforations, open hole sections, plugs, and squeezes are stored in the data repositories with their actual depths in reference to subsea. Subsequently, since numerical reservoir simulation discretizes the reservoir to solve the fluid flow equations, the step of pre-processing of well-related data is required to translate their locations from measured depth and true vertical depth to a discrete representation using the IJK mesh format. I, J, and K define the three axes for the 3D discretized grid space.

Figure 1 depicts an example of a well trajectory and perforations when represented in a continuous 3D XYZ space. On the other hand, Fig. 2 depicts the very same well, but represented in a discrete 3D IJK. This demonstrates an example of how well events are transformed from one space (domain) to another, i.e., from data repositories to pre-simulation process, and finally, to the reservoir simulation models.

Although, the main historical wells' information required by the simulator includes the production and injection rates, and perforation sections, there are many other well data types that are required to be integrated, and constantly updated to achieve valid and evergreen simulation model input data. This includes deviation surveys, which define the well's trajectory. The deviation surveys are required to see the intersections of wells with the grid cells in the simulation model. The preprocessor identifies the intersected grid cells with perforations. It also calculates the ratio factor at each perforated grid cell to indicate how much of that grid cell is really perforated. The ratio factor is required by the simulator to minimize the loss of details as a result of discretization.

Historical casing and tubing data are also required when modeling wells with advanced completion, including smart control valves and equalizers. Those wells are referred to as complex wells, due to the advanced downhole equipment and complex completions[5] as well as segmentation in modeling. Complex wells are defined differently in reservoir simulation models in which each well is multisegmented from the wellbore all the way to the surface. This is to enable more accurate pressure drop calculations, taking into account frictional losses, gravity, and smart completion nozzle restrictions, and so on. Complex wells' historical data has to be accurately incorporated into the preprocessor, including casing, liners, tubing, packers, inflow control valves, and inflow control devices (ICD). Each data type of these has a number of important parameters, which are required by the simulator such as depths, diameters, and nozzle sizes.

Formation tops are another piece of important well information for reservoir simulation models, which are used to validate the subsurface formations and perform stratigraphic investigations. Formation tops are interpreted from well logs and are used to quality check seismic surfaces and geology. Furthermore, history matching involves analyzing more historical wells' information such as repeated formation tests, production logging tool, core data, and productivity and

Fig. 1 *Well trajectory and perforations represented in a continuous 3D XYZ form in a preprocessor.*

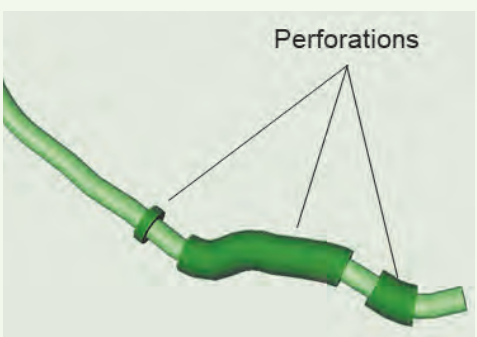

Fig. 2 *Perforations of the well represented in a discrete 3D IJK form in a preprocessor.*

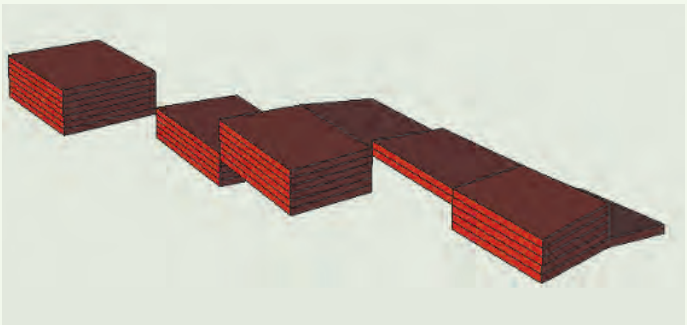

injectivity index data. This type of data is crucial for improving the history match quality and understanding the well's flow behavior in the wellbore.

Data QC Workflow

Each data type previously mentioned is associated with some level of uncertainty. Various types of tools are used to collect the data from the field, followed by human intervention, where some data are entered manually before the data is transferred from the field to the central repository. Some of the data requires interpretation before availing it for reservoir engineers — for consumption by different engineering and scientific processes. The data is then collected from the repository and incorporated in pre-processing tools for analysis and preparation — to be consumed by the numerical reservoir simulation models. This journey of cross-domain data transmission has multiple layers of processing, which can cause data alteration or loss, due to human errors or technology incompatibilities. For that reason, data has to be validated through a set of QC procedures.

Working on giant reservoirs involving thousands of wells and multiple data repositories, makes it impossible to manually perform a check of each well's data. The workflow discussed in this article consists of a QC module that automatically validates the different well data types prior to collecting them from the data repository.

The methodology that the QC module uses for validating the well's data consists of two main layers. The first layer compares data between different data sources. If any data type has information in multiple data sources, the workflow ensures consistency by comparing the specifications. The second layer involves validating the data against a set of rules, expected data ranges, and thresholds to ensure that the values are reasonable, excluding any outliers.

Each data type has its own set of QC rules and acceptance criteria. Some data, like deviation surveys, have a very dense frequency in the data repository, reaching thousands of records for one well. The module provides efficient cross-checks on this massive amount of data, and it detects any possible data issue before moving forward with using the data in the simulation model.

Validating deviation surveys is one example of well data QC. For instance, one of the validation checks for well trajectories is to compare the start depth in the deviation survey table and the wellhead point in the wellhead's table. In addition, repetition of the trajectory points or unexpected gaps between two consecutive trajectory points are also detected by the workflow. Moreover, a sudden change in drift angle or dogleg severity is checked and flagged. Another example is validating the casing and tubing data. The length of casing and tubing strings is validated against the addition of accessories — any pipe or completion section composing the casing or the tubing lengths — with each casing or tubing.

These accessories are also validated by checking their depths, ensuring that there is no overlapping, and checking that their outer diameter is greater than their inner diameter. Some other examples of QC checks are to ensure the correct assignment of the completions to their respective lateral, check the length of completion accessories, and ensure that the tubing removal date is not greater than the landing date of the next tubing. In addition, one important data type that is also validated is the perforation data. For example, one of the validation checks in perforations is by comparing different repositories to ensure the inclusion of all perforations, along with accurate lateral assignments. Similar types of QC checks and rules are applied on the different types of well data, including production and injection rates, real-time data, flow meters, productivity and injectivity, cores, formation tops, etc.

Figures 3 and 4 demonstrate an example of a well with missing perforations. Figure 3 illustrates a squeezed perforation isolating the wellbore from the formation.

Fig. 3 *Well section of a cased wellbore with a squeezed perforation.*

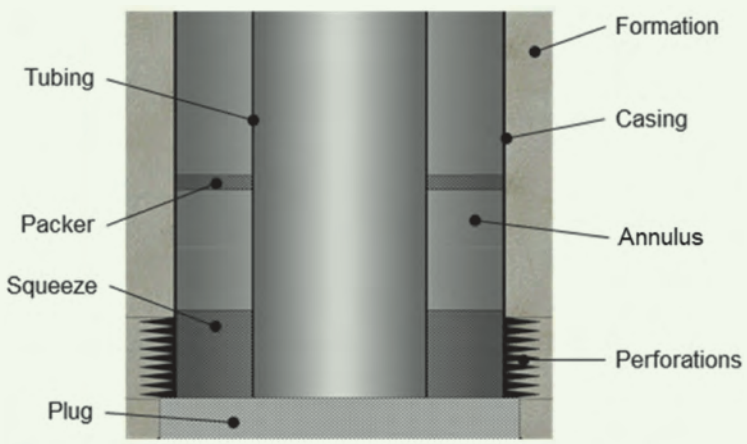

Fig. 4 *Well section of a cased wellbore with a squeezed perforation and a new perforation event added.*

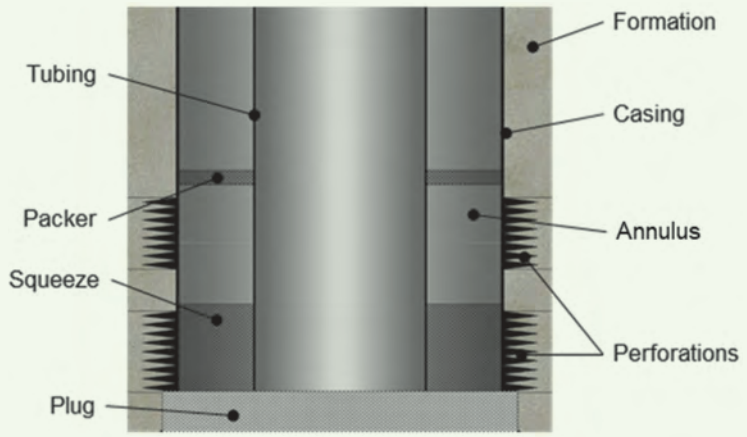

Subsequently, Fig. 4 illustrates the same well, but with adding another perforation after the squeeze event. This additional perforation in Fig. 4, if missed, will cause inaccurate representation of the well, causing inaccurate data in the simulation model. Such missing data issues can be detected by the data's QC workflow, simply by checking the production and injection rate of the well. A totally plugged well should have no production; however, the well production profile could tell otherwise, which will indicate missing perforations. The workflow prepares a report with detailed analysis and submits it to the data management for further review, and for taking the proper course of action(s).

Figure 5 shows a schematic of yet another potential data inaccuracy, and the implications of having inaccurate well input data in the simulation model. The horizontal well in this example was put in production as an open hole until the water cut reached the operational limits of the acceptable water cut. A workover job was performed to control water production by placing ICDs to equalize the production and minimize the water cut. Updating the simulation model with the workover event will give accurate representation of the well by placing the ICDs in their right locations (XYZ UTM

Fig. 5 *Well section of a historical well before and after workover.*

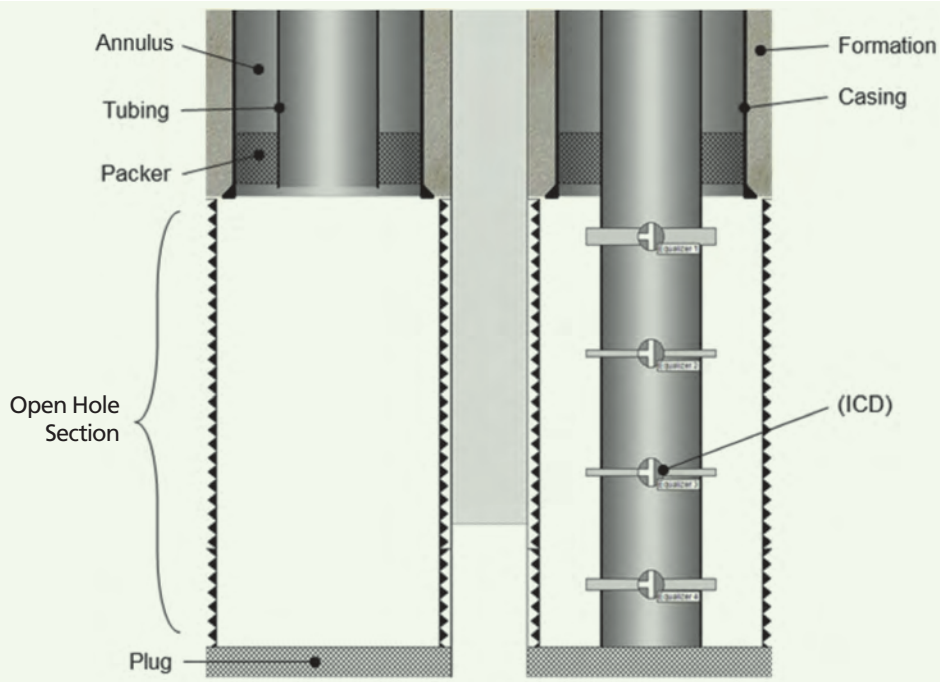

coordinates), and using their correct specifications.

Simulation results in Fig. 6 show the impact of accurately updating the simulation model on the water cut, which if not performed properly, will mislead the understanding of the well behavior and might cause some unwanted consequences.

Fig. 6 *Water cut with and without updating the completion data in the simulation model.*

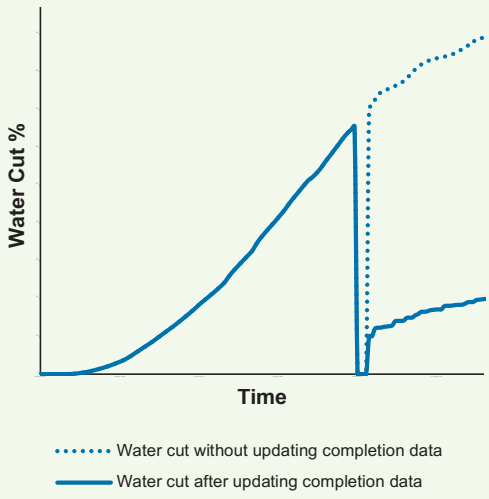

Automation of Simulation Well Data Transfer through an Integrated Framework

Simulation well information is retrieved from the data repository using the workflow described in this article. The workflow provides different levels of access to different repository schemas, preserving an engineer's access and role privileges.

It enables various engineers with different roles and different levels of access to utilize the simulation well information data into their different tasks. The workflow provides two ways to transfer data: (1) conventional data export and/or import, and (2) automated data transmission.

Conventional Workflow for Transferring Well Data from Repositories to Simulation Applications

This workflow provides the engineer with an interface to the data repositories enabling accessing, retrieving, formatting, and checking of the data in various formats, which can be read by all pre- and post-processing and simulation applications. The workflow starts by accessing the application by providing access credentials and then going through several steps to extract the required data in a certain format. After that, the data

Fig. 7 *The conventional workflow of transferring simulation well data.*

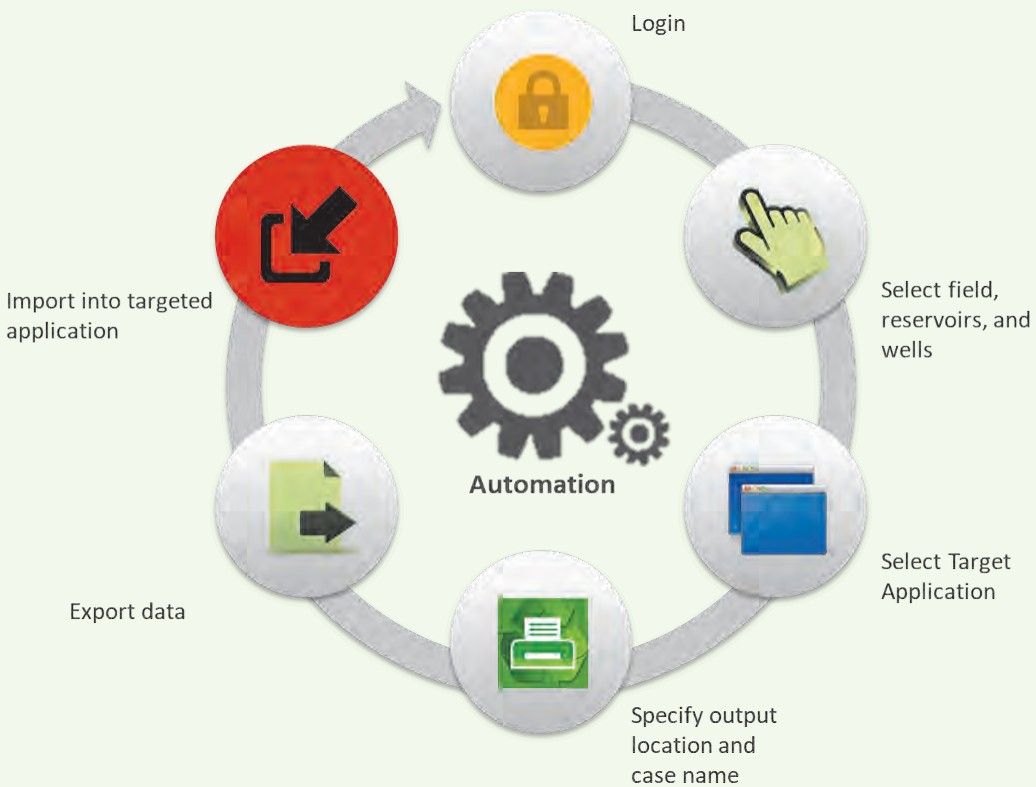

needs to be loaded into applications where the user goes through different procedures for each data type, and for each application. The workflow has a powerful engine that is accessed through a user interface. Figure 7 is a diagram of the conventional workflow for transferring simulation well data.

Automation of Simulation Well Data Transfer

To make efficient utilization of this engine, backend services were developed to expose the functionalities of the workflow to other applications through seamless communication. This workflow provides a new automated way of accessing simulation well information. It establishes a new framework that automates well data transmission to enable users to transfer data seamlessly between reservoir simulation applications through backend services.

The framework provides an integration solution that automates the acquisition of the well data, and the export and import processes. Also, the framework is meant for creating a data exchange solution that meets the specialized needs of exploration and production professionals, providing a more effective and efficient method of connecting diverse applications and data repositories.

The backend services were developed to allow the pre-processing applications to communicate with the different data sources to load new information, or update existing historical wells. The framework provides an integrated solution that automates updating simulation models with minimal human intervention.

Figure 8 shows the interaction between the backend services, data repositories, and different applications. This framework has a great impact on the time required for updating a wells' information in the simulation

Fig. 8 *Backend services' interaction with the data repositories and the different applications.*

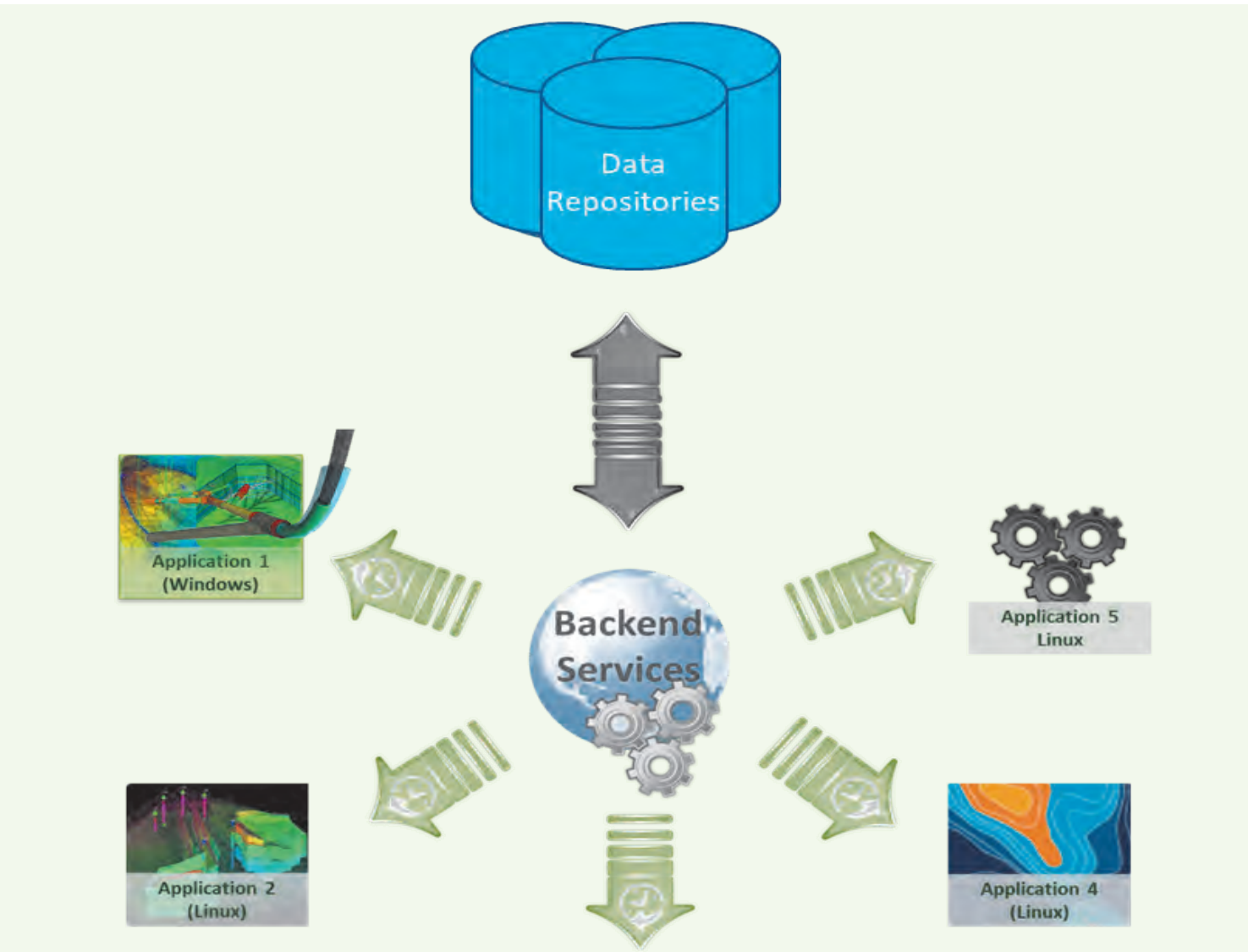

models. It avoids the need of accessing multiple applications and performing multiple operations to export and import data. In addition, engineers do not need to worry about the different file formats that are used by different applications.

Additionally, the framework avoids the need of manual editing and dealing with huge files, which sequentially prevents human errors and guarantees accurate well data updates, thereby helping to improve the overall accuracy and confidence of the simulation results. Furthermore, the seamless communication uses advanced data security and management that prevents exposing flat files of the wells' information.

Conclusions

Nowadays, reservoir simulation models are capturing detailed and complex geological features with higher resolution, in addition to incorporating detailed wells and field complicated operational constraints. This advancement includes supporting detailed wellbore completion and advanced technologies.

This article presented a workflow that helped to bridge the gap between the digital reservoir models and the physical reservoir. In addition, the article discussed the importance of data QC and validation, and how the workflow employs technology to ensure reliable, usable, complete and error-free well data to the simulator is provided. The efficient workflow demonstrated capitalizes on the Fourth Industrial Revolution digital twin principles to automate the process of seamlessly integrating and updating historical wells' information in reservoir simulation models. This is to drive reservoir simulation toward the adaptation of digital transformation and live Earth model concepts.

Acknowledgments

This article was presented at the International Petroleum Technology Conference, Dhahran, Saudi Arabia, January 13-15, 2020.

References

1. Shideed, M.A.: "Creative Utilization for Oracle Database to Meet Petroleum Engineering's Needs," SPE paper 93279, presented at the SPE Middle East Oil and Gas Show and Conference, Manama, Kingdom of Bahrain, March 12-15, 2005.

2. Al-Ismael, M.A., Al-Khawaja, H.A., Al-Quhaidan, Y.A., Nooruddin, H.A., et al.: "Automation of Well Modeling and Data Validation for Reservoir Simulation," IPTC paper 17541, presented at the International Petroleum Technology Conference, Doha, Qatar, January 19-22, 2014.

3. Al-Ismael, M., Al-Khawaja, H., Al-Nahdi, U. and Akhtar, M.N.: "Well Completion Data Adjustment Workflow for Reservoir Simulation," IPTC paper 17734, presented at the International Petroleum Technology Conference, Kuala Lumpur, Malaysia, December 10-12, 2014.

4. Al-Zahrani, T., Al-Mulla, M. and Al-Nuaim, M.: "Automatic Well Completions and Reservoir Grid Data Quality Assurance for Reservoir Simulation Models," SPE paper 175623, presented at the SPE Reservoir Characterization and Simulation Conference and Exhibition, Abu Dhabi, UAE, September 14-16, 2015.

5. Shenawi, S., Hidayat, W., Shammari, M., Nasser, K., et al.: "Application of a Newly Developed Workflow to Design and Optimize MRC and Smart Well Completions," SPE paper 164212, presented at the SPE Middle East Oil and Gas Show and Conference, Manama, Kingdom of Bahrain, March 10-13, 2013.

About the Authors

Menhal A. Al-Ismael

M.S. in Petroleum Engineering, King Fahd University of Petroleum and Minerals

Menhal A. Al-Ismael is a Petroleum Engineering Systems Analyst working in the Simulation Systems Division of Saudi Aramco's Petroleum Engineering Applications Services Department, where he provides solutions and system support to reservoir simulation studies.

Menhal has more than 10 years of experience in petroleum engineering systems support, working on many projects in the area of field development planning and optimization.

He is a Society of Petroleum Engineers (SPE) Certified Petroleum Engineer.

Menhal received his B.S. degree in Information and Computer Science, and his M.S. degree in Petroleum Engineering, both from King Fahd University of Petroleum and Minerals (KFUPM), Dhahran, Saudi Arabia.

Dr. Ali A. Al-Turki

Ph.D. in Petroleum Engineering, University of Calgary

Dr. Ali A. Al-Turki is a Petroleum Engineering Systems Specialist working in the Simulation Systems Division of Saudi Aramco's Petroleum Engineering Applications Services Department. He has been with Saudi Aramco for the past 21 years.

Ali's research interests include multiphase flow in fractures, thermal (SAGD) and thermal solvent (ES-SAGD) recovery processes, assisted history matching methodologies, uncertainty quantification and management, and high performance computing.

He is a Society of Petroleum Engineers (SPE) Certified Petroleum Engineer.

Ali is the author and coauthor many technical papers, along with a number of patents.

He received his B.S. degree in Computer Science from King Fahd University of Petroleum and Minerals (KFUPM) Dhahran, Saudi Arabia. Ali received both his M.S. and Ph.D. degrees in Petroleum Engineering from the University of Calgary, Alberta, Canada.

Abdulaziz M. Al-Darrab

M.S. in Petroleum Engineering, University of Southern California

Abdulaziz M. Al-Darrab is a Petroleum Engineering Systems Analyst working in the Simulation Systems Division of Saudi Aramco's Petroleum Engineering Applications Services Department. He has more than 13 years of experience in petroleum engineering systems, providing solutions and system support to reservoir simulation engineers. Abdulaziz has worked on many projects in the area of post-processing and 3D visualization, and high performance computing.

He is a Society of Petroleum Engineers (SPE) Certified Petroleum Engineer.

Abdulaziz received his B.S. degree in Software Engineering from King Fahd University of Petroleum and Minerals (KFUPM), Dhahran, Saudi Arabia. He received his M.S. degree in Petroleum Engineering from the University of Southern California, Los Angeles, CA.

Laser Perforation: The Smart Completion

Dr. Sameeh I. Batarseh, Dr. Damian P. San-Roman-Alerigi, Abdullah M. Al-Harith, and Dr. Haitham A. Othman

Abstract /

Perforation is the commonly used well completion technology to establish communication between the wellbore and hydrocarbon-bearing formations — this is critical for optimal production. The proposed new well completion in perforation technology utilizes high power laser energy. The technology attracted the oil and gas industry to its unique properties, such as it's nonexplosive-based perforation technology with precise control over the perforated tunnel's shape, size, and geometry. The laser energy also creates permeability in the perforated tunnel. The successful research effort led to field deployment strategy in the next two years. The laser completion system consists of the laser source to generate the energy, which is mounted on a coiled tubing unit on the surface, with a fiber optic cable to transmit the energy to the downhole target, and to the laser perforation tool. The principle of the tool is based on combining optical and mechanical components. The alignment of the optics inside the tool provides the ability to control and generate different beam shapes and sizes; these create several perforated shots in any direction.

A comparison was made between the perforations made with shaped charges and the laser. The test used the same conditions and rock types. Pre- and post-perforation measurements were conducted for comparison. The tunnel that is perforated by the high power laser is clean with no compaction, deformation, or melt. The result also shows the same in all rock types with improvement in the permeability along the perforated tunnels. A detailed analysis was carried out using different methods, such as imaging and thermal analysis.

High power lasers provide a controllable heat source while penetrating the formation that enhances flow properties, especially in a tight formation. Continuous work over the past two decades have proven that laser perforation can create large perforation tunnels with a large diameter. Laser perforation was applied on all types of rocks, including unconventional tight sands.

The potential of this technology is that a laser can be the next new smart perforation generation that will change current well perforation. The state-of-the-art high power laser technology in a downhole perforation provides an innovative and safe nonexplosive technology. Precision in controlling the power, orientation, and the shape of the perforation beam are some of the properties of the technology that made it attractive for downhole applications.

Introduction

Perforations create a tunnel that connects the wellbore and hydrocarbon-bearing formations. The geological, mechanical, and morphological properties of this channel determine flow performance and directly impacts production. Experimental tests have shown that productivity increases in direct relation with the perforation length and diameter; it is also affected by the hydraulic pressure differential, density, angle, and phasing, albeit nonlinearly. Therefore, productivity can be significantly improved by optimizing these variables[1, 2]. An ideal perforation technology would create a long and wide channel with positive skin; this is a challenge. Table 1 summarizes some of the perforation techniques commercially available and their critical factors.

The leading technique in field operations is the use of shaped charge perforators. The method detonates explosive charges to create tunnels that act as conduits for the hydrocarbons. The shape of the explosive container is designed — or shaped — to optimize the energy flow of the explosion toward the target; however, creating deep and large perforations with this method has several challenges. The explosive and liner of the shaped charge may yield either a deep or large diameter perforation, not both. A deep perforation is desired, because it bypasses the damaged zone caused by drilling; whereas, a large hole is desired to decrease the hydraulic differential pressure and produce more hydrocarbons.

Explosive-based processes compress the rock and generate a shockwave, which compacts the rock and creates a crushed zone around the tunnel. This crushed volume has lower porosity and permeability, Fig. 1. Experimental results showed that in this volume, the permeability is 65% to 80% lower than in the virgin rock, and porosity diminishing between 10% to 50%[5, 6].

Figure 2 presents a comparison of the physical differences between the crushed zone and the virgin rock[5]. The

Table 1 *A summary of commercially available perforation methods and critical factors affecting their performance.*

Technology	Description	Critical Factors
Shaped charge perforator	An explosive-based method shaped to focus the explosion's energy. The charge pierces through casing, cement, and formation at high energy (pressure reaches up to 15 million psi). The process generates a shockwave that damages and compacts the volume around the perforation tunnel[3].	• Charge design • Geomechanical stress states • Formation properties • Perforation diameter • Penetration depth • Formation plasticity • Completion design
Bullet perforator	An explosive-based method similar to shaped charges but with limited energy. It is used in formations with high plasticity. Because of its design and application, the perforation density is limited[3].	
Hydro-jet perforator	Pressure based method. It uses a water jet at high-pressure (20,000 psi) to erode the target and create a tunnel in an open hole. It causes low damage, but has limited use due to friction pressure drop and back pressure, which significantly reduces the jet's energy[3]. It has been recommended for open hole wells.	• Job depth • Back pressure • Geomechanical stress states • Penetration depth • Completion design
Abrasive perforator	Erosion method that uses high volumes of abrasive fluids to erode the target and create a tunnel. It has limited performance due to friction pressure drop, back pressure, and cavitation. The abrasive material can be designed to target a specific material or formation; e.g., carbonate, steel, or cement, among others[4].	

Fig. 1 *Comparison of the porosity change between the crushed zone (bottom left) and virgin rock (bottom right) for a perforated rock sample[5]. The porosity in the crushed zone is approximately 10.5% compared to 21% in the virgin zone of the rock sample. These images and data represent the whole area around the perforation tunnel.*

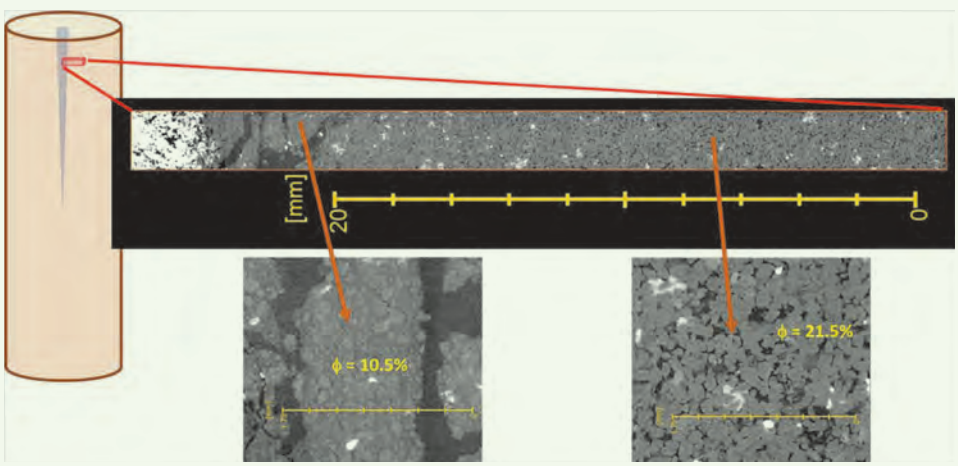

results show the perforated rock has been compacted. The reduction of permeability and porosity affects hydrocarbon production. It hinders injection and production capabilities, and negatively affects fracturing operations. Therefore, explosive based perforations may require cleanup to remove the damage and ensure hydraulic conductivity. The alternative is to mitigate or bypass the crushed zone by perforating underbalanced, with extreme overbalance, or performing an acid wash across the perforations, among other methods.

The morphology (depth, diameter, and shape) of the perforation depends on the formation stresses and compressive strength. One laboratory study found that the depth of perforation using shaped charges is inversely proportional to compressive strength and effective stress[7]. For example, the depth of perforation dropped

Fig. 2 *Comparison of the compaction between the crushed zone (a), and the virgin rock (b)[5].*

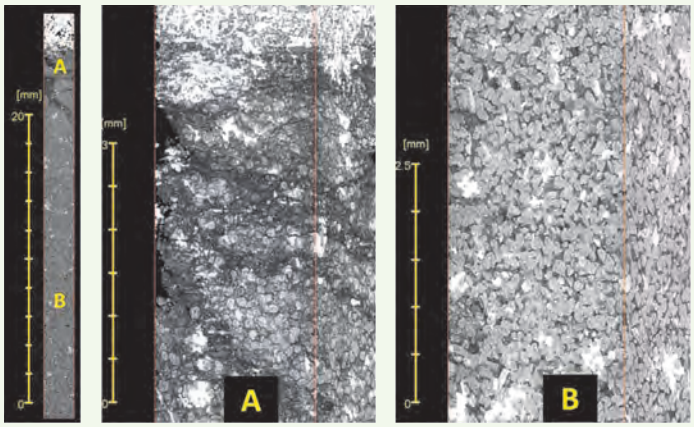

30% in Berea sandstone (BG) when the stress increased from 200 psi to around 5,000 psi. In dolomite, the depth of perforation fell by 47% when applying the same test conditions[7].

Another laboratory study replicated in situ conditions of stress and found that the depth of perforation of shaped charges is greatly influenced by stresses normal to the direction of perforation[8]. The statistical analysis showed that the correlation between the perpendicular stresses is 49% and 39%, respectively; the vertical stress contributed only 12%. The diameter of the perforation also depends on the stresses and directly relates to the damage volume; however, it should be large enough to prevent proppant from bridging in the entrance[9]. A solution is to decrease the charge size and increase the density of shots[3], which may result in additional damage and cleanup requirements.

Laser Perforation

Laser is a technology that utilizes the power of light to perforate rocks; the laser energy absorbed by the rock transforms into heat, and this is used to drive different thermal processes, such as ablation, dissociation, calcination, melting, or even sublimation. Several experimental tests on different rock types showed that laser perforation creates a tunnel with improved permeability and porosity, which yields higher flow and production[10].

The technology is non-damaging, nonexplosive, and can create various perforation geometries, in size and shape. Consequently, it reduces several logistics and safety concerns regarding transportation, storage, and deployment.

In the field, the laser source is mounted on a coiled tubing unit. The laser will be transmitted downhole via fiber optics to the optical bottom-hole assembly (oBHA). The oBHA combines electronic, optical, and mechanical components to control the beam and create the desired perforation job.

The tool also eliminates tripping since the laser is controlled and enabled from the surface. Once the system is inside the well, it can perform multiple jobs concurrently in the same location, or serially along the well. The only caveat to parallel job performance is the availability of laser energy.

Laser technology offers versatility and the opportunity to develop and integrate smart hybrid systems for perforation. This is already a reality in laser manufacturing where robots, artificial intelligence, advanced materials, and sensing combine in hybrid laser tools with unique performance and capabilities[11-13]. Similarly, smart (laser) perforation tools are expected to provide unprecedented control of the perforation's design, including geometry (depth, diameter, and shape), phasing, orientation, and density.

Therefore, it is vital to analyze and model laser-rock and laser tool formation interaction across a wide range of settings, both in situ and in the lab. For downhole, it is equally essential to develop sensing feedback loops that guide real-time adaptation and optimization through reinforcement learning[14, 15]. Sensing is needed because the process parameters change with the rock type and environment properties[16-18]. The combination of these systems together with the versatility of laser begets a tool that can adapt and possibly operate in any subsurface condition, and target every formation.

Optimization

The optimization process begins in the laboratory. There the interaction between the laser, rock, and different system's components are analyzed using different parameters, sensors, and rock types. For example, in one optimization test the laser was programmed to create several thousands of shots with different parameters in the BG sample and the Yellow limestone (LSSY) sample from a Saudi quarry, Fig. 3.

Statistical analysis of the results provides a comprehensive insight into the interaction, and enables discovery of important relations. The fundamental statistics for this particular experiment are summarized in Table

Fig. 3 *Example of multiple perforations made on the LSSY sample for optimization and development.*

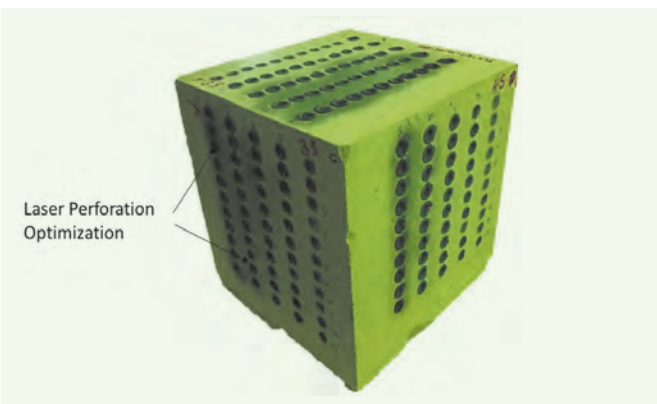

2 and Fig. 4. The data in the distribution shows that it is possible to attain different results, depending on the parameter settings.

The combined data is then used to study the correlation between the system parameters and the measured variables, Fig. 5.

The correlation analysis shows that there is an intricate dependence between the target and system variables. The relation is not linear and may involve many physical parameters[18, 19]. The results also evince the relative importance of some variables for perforation in different rocks in this experiment. For example, the distance between the output nozzle and the rock has no significant impact on the process in the LSSY, but it is somewhat crucial in the BG samples.

The full optimization process needs to account for

Table 2 *The mean, standard deviation, and median of volume of perforation, depth of perforation, and rate of perforation based on multiparameter shots in the BG and LSSY samples.*

	Variable	Unit	BG	LSSY
Mean	Volume of perforation	mm^3	1,597.8	716.4
	Depth of perforation	mm	17.4	13.1
	Rate of perforation	mm/s	2.7	4.6
Standard Deviation	Volume of perforation	mm^3	1,745.9	1,135.5
	Depth of perforation	mm	9.4	9.2
	Rate of perforation	mm/s	1	2.5
Median	Volume of perforation	mm^3	881.9	334
	Depth of perforation	mm	15.1	10.7
	Rate of perforation	mm/s	2.7	4.7

Fig. 4 *Distribution density of different target variables for gray BG and LSSY after laser perforation tests. The lines show the position of the mean (dashed) and median (dotted) for each rock, Table 1.*

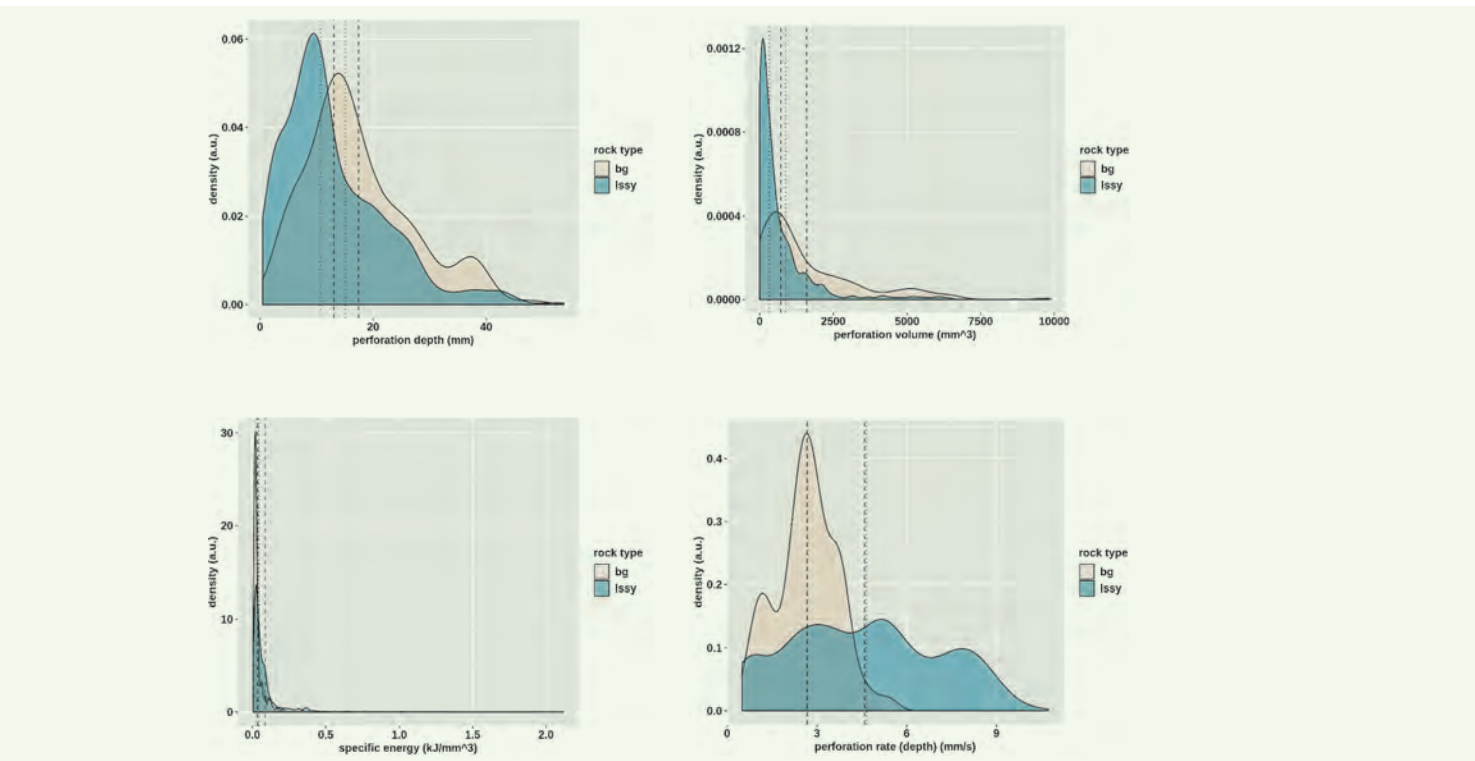

Fig. 5 *Spearman's rank correlation between target and system variables for complete data (top), BG (middle), and LSSY (bottom). Target variables are: perforation depth (perf.l), rate of perforation (perf.rl), and specific energy (perf.se). The system variables are: beam energy (beam.e), power (beam.p), laser on time (beam.t), and the distance between the purge output and the target (separation).*

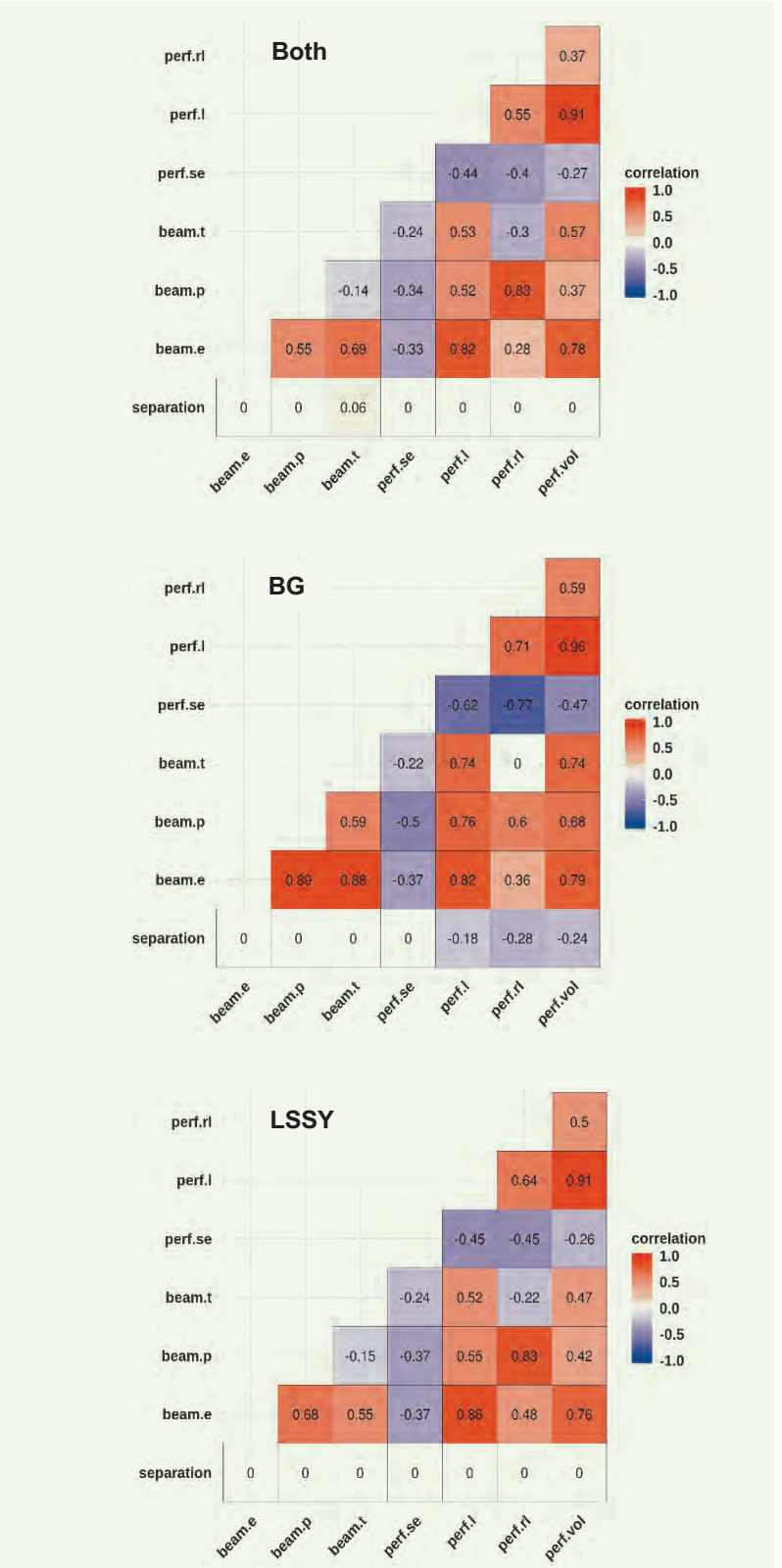

this and enable prediction in a complex environment. A potential solution for reliable optimization is to use conditional decision trees for the target (depth of perforation or volume of the perforation) and the domain variables (beam energy, separation, and rock type). The results are generated by the recursive partition of the domain[20]. The model provides a fast and reliable prediction on the behavior of the target variable. Figures 6 to 8 show the regression models, which are built using 70% of the experimental data and tested on the remaining set.

The results show that there are critical combinations of beam power and exposure time that lead to optimal results. These models, however, are the beginning of the development of smart laser perforation tools. In the field, the system would likely use a combination of deep learning and reinforcement learning to consider the information provided by different sensors (dynamic data), the known information (well logs, static data), and desired perforation design (target). This process would allow the system to learn and become more efficient over time. This neural engine would drive different components to manipulate the beam and provide the geometry and design desired.

Geometry

The shape and geometry of the perforated tunnel are critical for stability, sanding, and flow, among others. Laser perforation enables the controlled optimization of the tunnel to enhance production and flow. The shape and the geometry of the laser perforation can be manipulated using diffractive, refractive, and scattering optics[16, 21].

The optical systems for subsurface application will be based on lenses, mirrors, and prisms to control the beam. These are combined to create different optical systems for subsurface operations; including optical heads to focus, de-focus, collimate and expand, or contract the beam. They also serve to control the beam through the subsurface medium. The material in the optical path also affects the beam path; these vary from elongating the optical path to scattering, absorption, and nonlinear responses. Therefore, the system must be able to accommodate different conditions and control the optics to attain the desired effect[21]. The combined effect of the optical tool and the optimization process is a clean and long laser perforation. Figure 9 shows the picture and computed tomography (CT) scan of the optimized process in a LSSY sample. In this experiment, the laser beam was set to provide the longest tunnel through the sample.

The beam control also enables the creation of various perforation shapes — transversal to the direction of the perforation. This is important for flow and geomechanical stability[18]. When the tool creates a tunnel in the formation the stress around the tunnel will affect its stability, which may collapse depending on the stress state of the formation; e.g., if the maximum horizontal stress in the reservoir exceeds the strength of the tunnel. In this case, the laser perforation process can create a perforation explicitly shaped to counteract

Fig. 6 *A conditional decision tree for the full data set of both rocks. The tree exemplifies the global optimization procedure.*

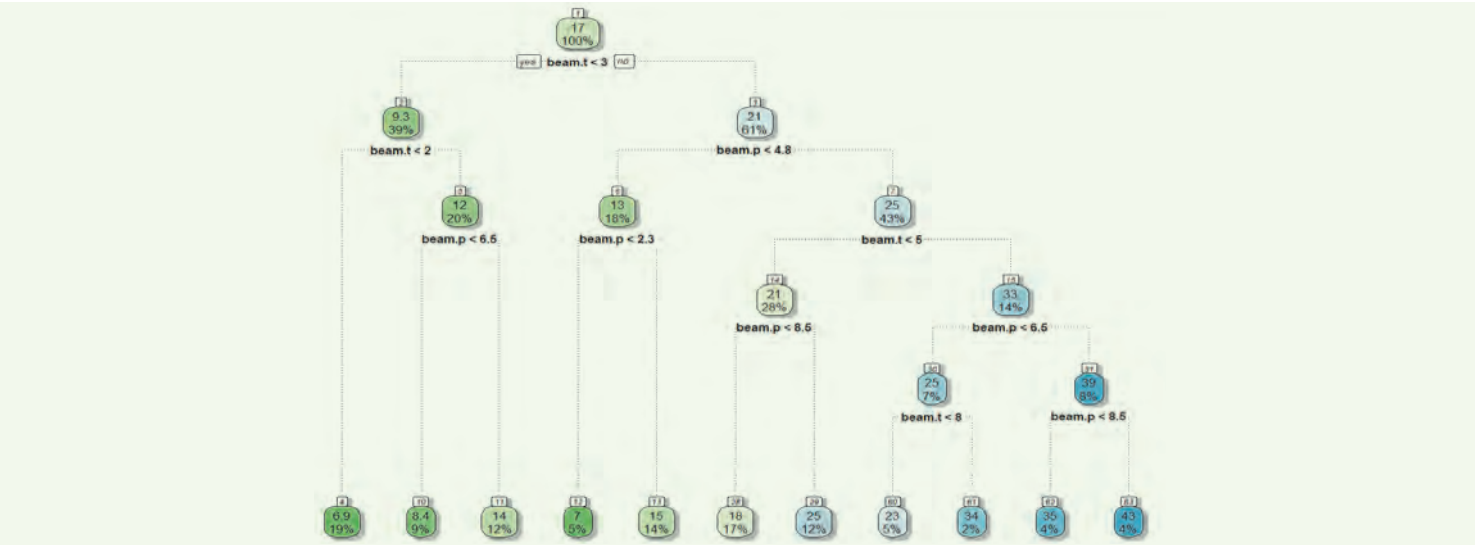

Fig. 7 *A conditional decision tree for the target variable perforation depth (perf.l). The data corresponds to the BG sample. The tree exemplifies a possible optimization path for this rock under the test's experimental conditions.*

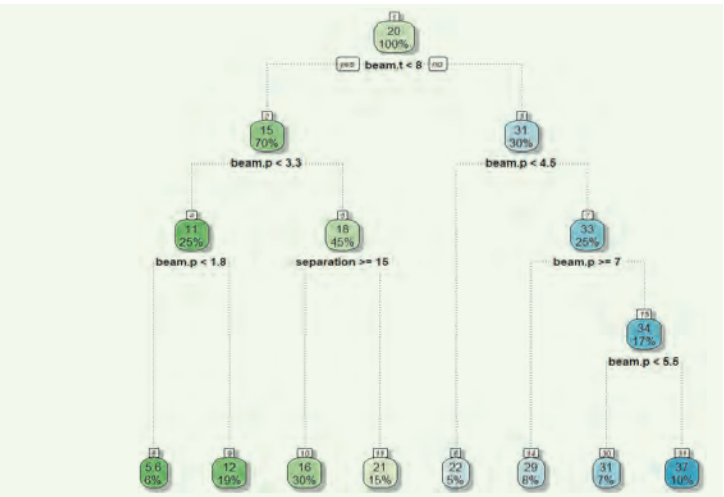

Fig. 8 *A conditional decision tree for the target variable perforation depth (perf.l). The data corresponds to the LSSY sample. The tree exemplifies a possible optimization path for this rock under the test's experimental conditions.*

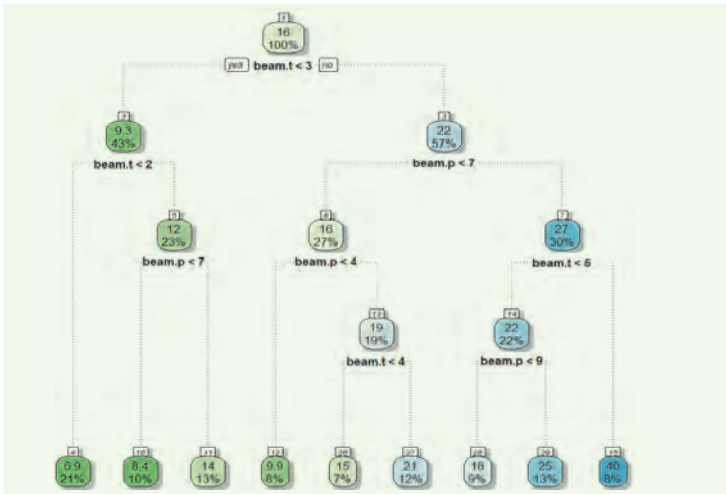

the state of stresses.

Figure 10 shows an example of a perforation designed with an oval shape. This type of perforation can be applied where the long hole axis is parallel to the stress, which will prevent the hole from collapsing.

Depth

Laser perforation can be applied to any rock. The process can pierce through and perforate unconsolidated sand, limestone, carbonate, or granite. Figure 11 shows a deep perforation in an unconsolidated sand core. The optimization process and optical package create different perforation lengths. The optimization process previously discussed uses this data to find the optimal variable settings to generate a long perforation.

Deep tunnels can be obtained by turning the laser for more time or increasing the power, an example of the depth of perforation as a function of energy is presented in Fig. 12. Deeper tunnels are crucial to bypass near wellbore damage.

Orientation

The optical system can also orient the beam in different directions, bringing the opportunity to control the radial (phasing) and azimuthal angles as necessary. The orientation of the tunnel can enable different flow

Fig. 9 *A CT scan showing the laser perforation before and after in a LSSY rock sample. The pictures show a photo of the top region of the rock (a), the CT scan before perforation (b), and after laser perforation (c). The sample's dimensions are 20 cm long, by 10 cm wide, and 10 cm in height.*

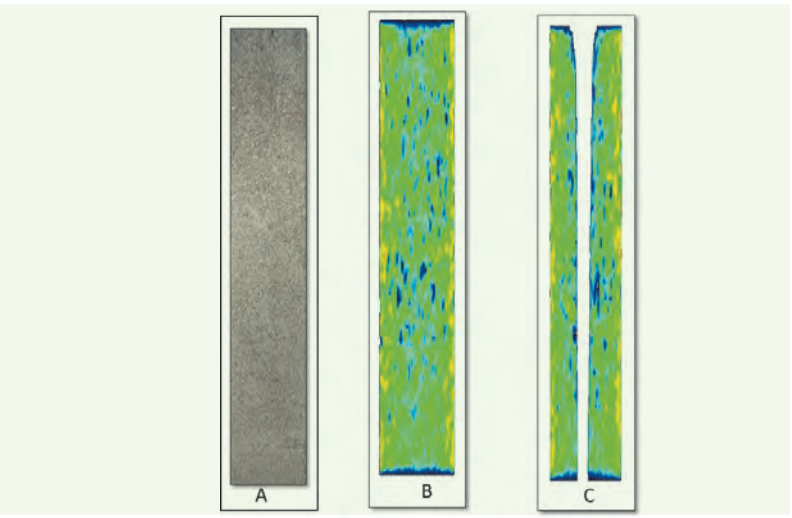

patterns from the formation into the wellbore; e.g., tunnels at opposite angles can be used to improve drainage and capillary effects. There is no limit to the number of perforations the laser can create. Figure 13 is an example of a dual perforated tunnel in an unconsolidated sand core.

Geological Heterogeneity

Laser perforation is a thermal process that is independent of the rock type, stress, hardness, fractures, lamination, or any heterogeneity. The beam penetrates in a straight line and creates a clean and symmetrical tunnel. The perforation's geometry is not directly affected by the geomechanical state of stresses or material heterogeneity.

Figure 14 presents the CT images before and after laser perforation on a highly laminated shale sample, typical of unconventional reservoirs. The perforation is symmetrical and uniform along the core; it goes through the laminations without changes in direction and transversal geometry.

Figure 15 shows another example of laser perforation through a calcite intrusion in the LSSY sample; in this case, the intrusion was weaker than the rock and the laser was able to penetrate through it, creating a symmetrical tunnel.

Enhanced

The heat generated during the laser perforation process can be controlled in some instances to modify the physical and chemical structure of the rock around it. For example, in one experiment, the laser perforation generated fractures by creating thermal shocks. The temperature delivered to the rock samples varies depending on the laser power, time, and physical properties.

Figure 16 depicts an example of the temperature distributions in a shale sample during laser perforation. The image was captured using a special mid-infrared camera. The results showed the temperature reached up to 2,000 °C in the first two seconds of exposure to a 5 kW beam (10 kJ). The temperature distribution in the rock can also be controlled through the purge gas assist. The net result is the generation of sharp temperature gradients that can fracture the rock, collapse clays, and dissociate minerals. The process depends on the

Fig. 10 *A CT scan of a laser perforation with an oval shape (transversal) in an unconsolidated sandstone core. The sample's dimensions are 10 cm in diameter by 15 cm in length.*

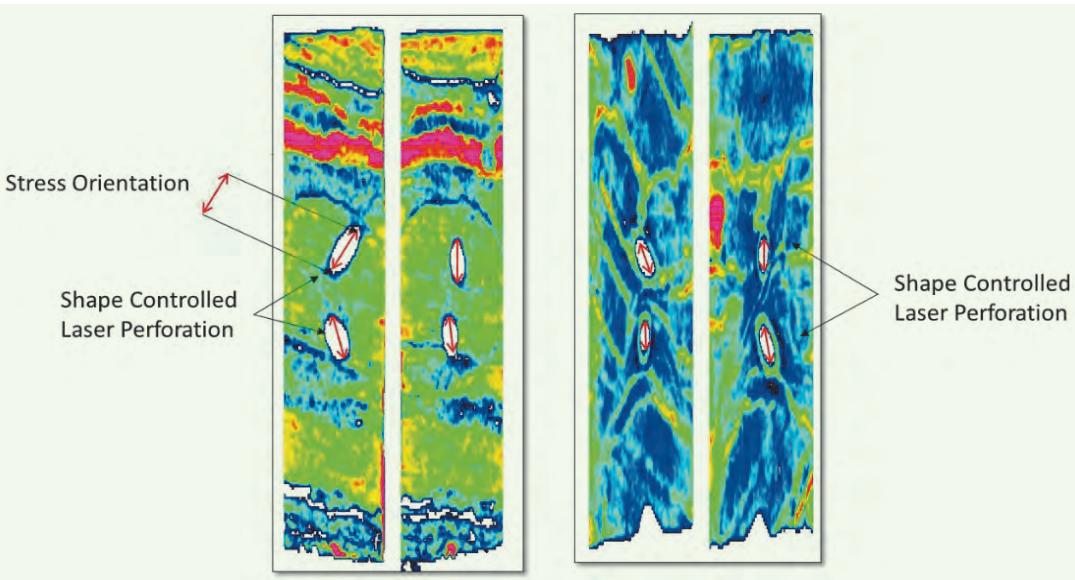

Fig. 11 *A CT scan of the laser perforation in unconsolidated sand. The transfer function in the reconstructed image has been modified to show the low-density range. The sample's dimensions are 10 cm in diameter by 10 cm in length.*

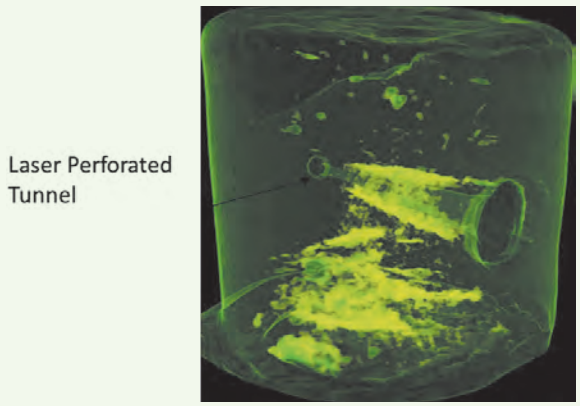

Fig. 12 *A density plot of the perforation depth as a function of the beam power and period of time for the LSSY sample.*

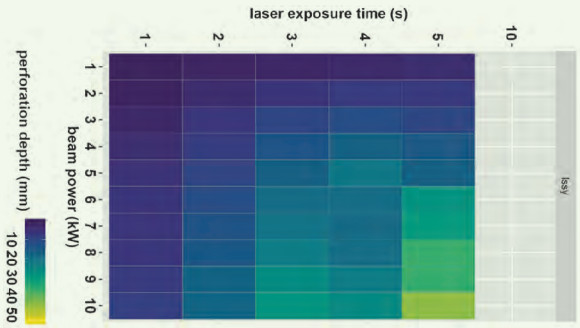

Fig. 13 *A CT scan of multilaser perforation in an unconsolidated sand core. The transfer function in the reconstructed image has been modified to show the low-density range. The sample's dimensions are 10 cm in diameter by 10 cm in length.*

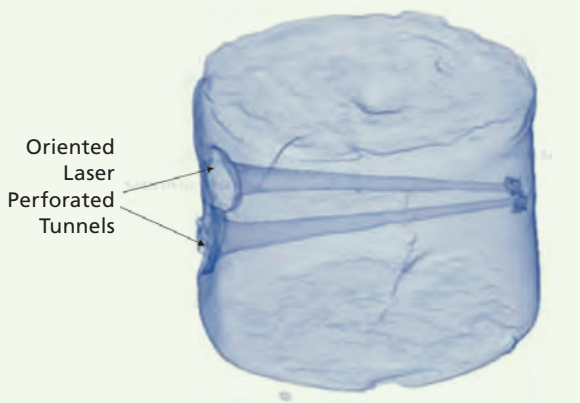

Fig. 14 *A CT scan of a shale sample before (left) and after laser perforation (right). The sample is highly laminated. The transfer function in the reconstructed image has been modified to show the wide density range, and then cut to show the perforation hole. The sample's dimensions are 10 cm in diameter and 30 cm in length.*

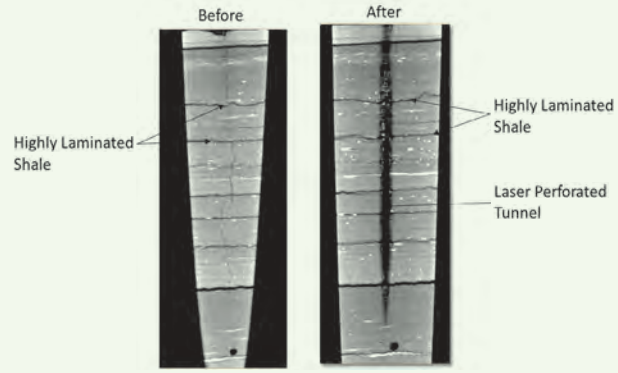

Fig. 15 *An image of a laser perforation through a calcite intrusion in the LSSY sample. The image shows the laser perforation cutting through an intrusion without affecting the perforation's path.*

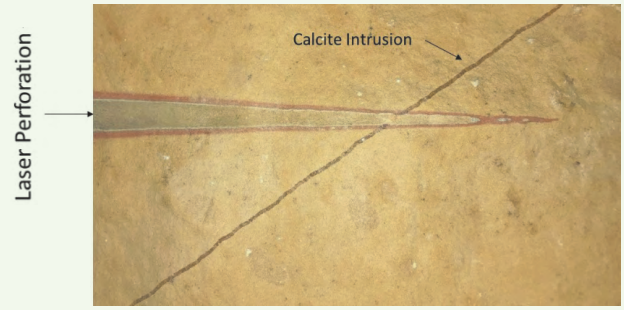

Fig. 16 *High-speed thermographic image of the temperature distribution during laser perforation of a shale sample.*

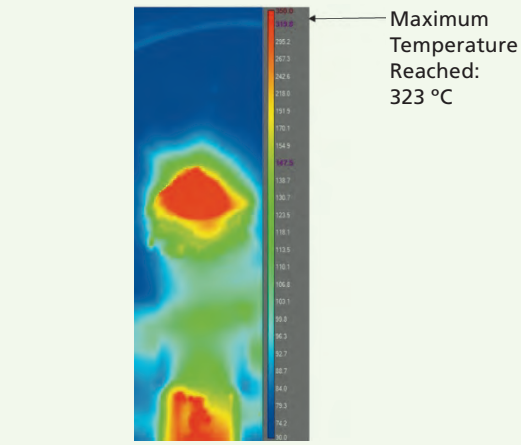

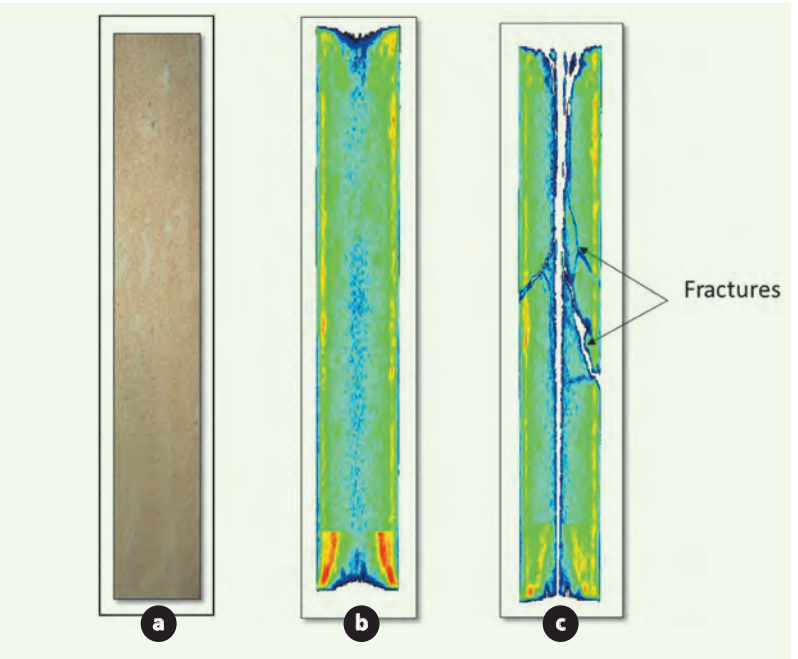

Fig. 17 *A CT scan showing the laser perforation and fracturing before and after in a LSSY sample. The pictures show a photo of the top region of the rock (a), the CT scan before perforation (b), and after laser perforation (c). The sample's dimensions are 20 cm long, by 10 cm wide, and 10 cm in height.*

temperature and the mineralogy of the sample[18, 22].

Figure 17 shows a perforation with fractures in a LSSY sample. The fractures developed along the tunnel. These fractures are desirable to maximize reservoir contact and improve flow and production. If fractures are not desired, due to stability issues, then this can be controlled by reducing the laser exposure time, beam power, and purging media.

Conclusions

High power lasers provide a controllable heat source that can penetrate the formation and enhance the rock's flow-related properties, especially in tight formations. In-depth analysis confirms that lasers create a controllable and undamaged perforated tunnel in different formations. The versatility of the laser perforation enables the smart completion; the tool's parameters can be adapted to work in multiple targets and designs. The nature of the laser also ensures that there are few deployment conditions.

This study presented the statistical analysis of the tool's performance in two different rock types at ambient conditions and derived an optimization path using conditional regression trees. The study used lab data from over 1,200 laser perforation shots on LSSY and BG samples; additional analyses are underway for other rock types; e.g., shales, laminated sandstone, and unconsolidated sand.

The results showed that there are different conditions to produce global optimal parameters to create a deep perforation. In the subsurface, the combination of this optimization process will serve as a starting point for reinforcement learning. The downhole system will incorporate sensors to provide a feedback loop that guides real-time adaptation and optimization through reinforcement learning. The combination of these systems together with the versatility of the laser will enable the tool to operate in any subsurface condition and target every formation.

The technology was used to create different perforation designs. The CT scans showed the quality of the perforated tunnel without melt, and undamaged. The CT images also showed that the laser could create fractures in the tunnel if required. This provides the opportunity to create enhanced perforation designs. Additional CT images demonstrated that the tool could create tunnels with different orientations and shapes, both with precise control. These perforation tunnels were made in heterogeneous formations, tight, and highly laminated.

The result of the analyses showed that the geometry of the laser perforation is independent of stress, formation, structure, and strength. These results prove that the harder the rock is, the better the laser rock interaction; this is due to higher density, which brings more effective heat transfer, and therefore better penetration.

Laser perforation is a promising technology that has the potential to change the current practice. This tool has the ability to perform unlimited oriented shoots as the laser operates by turning on and off a switch. This eliminates the need for tripping, loading and unloading the gun, any misfiring, and the handling of explosives. In addition, the logistics, safety, storage and transportation are easy.

Acknowledgments

This article was presented at the Abu Dhabi International Petroleum Exhibition and Conference, Abu Dhabi, UAE, November 11-14, 2019.

References

1. Eberhard, M.J. and Schlosser, D.E.: "Current Use of Limited-Entry Hydraulic Fracturing in the Codell/Niobrara Formations — DJ Basin," SPE paper 29553, presented at the Low Permeability Reservoirs Symposium, Denver, Colorado, March 19-22, 1995.

2. Tariq, S.M.: "Evaluation of Flow Characteristics of Perforations, including Nonlinear Effects with the Finite-Element Method," *SPE Production Engineering*, Vol. 2, Issue 2, May 1987, pp. 104-112.

3. Rastegar, R., Munawar, M., Nowowiejski, D., Granberg, S., et al.: "Mitigating Formation Damage by Using Completion with Built-in-Casing Perforations Instead of Perforation with Explosive Charges," SPE paper 174251, presented at the SPE European Formation Damage Conference and Exhibition, Budapest, Hungary, June 3-5, 2015.

4. McCauley, T.V.: "Backsurging and Abrasive Perforation to Improve Perforation Performance," *Journal of Petroleum Technology*, Vol. 24, Issue 10, October 1972, pp. 1207-1212.

5. Grove, B., Grader, A., Derzhi, N. and McGregor, J.: "Perforation Damage, Cleanup, and Inflow Performance: Advances in Diagnostics and Characterization," SPE paper 195019, presented at the SPE Middle East Oil and Gas

Show and Conference, Manama, Kingdom of Bahrain, March 18-21, 2019.

6. Walton, I.C.: "Optimum Underbalance for the Removal of Perforation Damage," SPE paper 63108, presented at the SPE Annual Technical Conference and Exhibition, Dallas, Texas, October 1-4, 2000.

7. Saucier, R.J. and Lands Jr., J.F.: "A Laboratory Study of Perforations in Stressed Formation Rocks," *Journal of Petroleum Technology*, Vol. 30, Issue 9, September 1978, pp. 1347-1353.

8. Norouzi, P., Hashemolhosseini, H. and Baghbanan, A.: "Stress-Dependent Perforation in Carbonate Rocks: An Experimental Study," *SPE Drilling & Completion*, Vol. 33, Issue 3, September 2018, pp. 209-219.

9. Gruesbeck, C. and Collins, R.E.: "Particle Transport through Perforationism," *Society of Petroleum Engineers Journal*, Vol. 22, Issue 6, December 1982, pp. 857-865.

10. Batarseh, S.I., Graves, R., Al Obaid, O., Al Hartih, A., et al.: "High Power Laser Technology in Downhole Applications, Reshaping the Industry," SPE paper 188507, presented at the Abu Dhabi International Petroleum Exhibition and Conference, Abu Dhabi, UAE, November 13-16, 2017.

11. Galbraith, C.: "Laser Welding and Smart Manufacturing," *Industrial Laser Solutions for Manufacturing*, July/August 2019, pp. 14-16.

12. Naeem, M.: "Advanced Control of Laser Material Processing Provides Smart Techniques for Cutting, Welding, and Drilling," *Industrial Laser Solutions for Manufacturing*, February 2016, *https://www.industrial-lasers.com/home/article/16486667/advanced-control-of-laser-material-processing-provides-smart-techniques-for-cutting-welding-and-drilling.*

13. Rockstroh, T.J., Scheidt, D. and Ash, C.: "Advances in Laser Drilling of Turbine Airfoils," *Industrial Laser Solutions for Manufacturing,* Vol. 17, Issue 8, August 2002.

14. Liu, S., Wang, X., Liu, M. and Zhu, J.: "Toward Better Analysis of Machine Learning Models: A Visual Analytics Perspective," *Visual Informatics*, Vol. 1, Issue 1, March 2017, pp. 48-56.

15. San-Roman-Alerigi, D.P., Batatseh, S.I., Li, W. and Othman, H.: "Machine Learning and the Analysis of High Power Electromagnetic Interaction with Subsurface Matter," SPE paper 195118, presented at the SPE Middle East Oil and Gas Show and Conference, Manama, Kingdom of Bahrain, March 18-21, 2019.

16. Batarseh, S.I., San-Roman-Alerigi, D.P., Al Obaid, O. and Othman, H.A.: "Laser Gun: The Next Perforation Technology," SPE paper 194775, presented at the SPE Middle East Oil and Gas Show and Conference, Manama, Kingdom of Bahrain, March 18-21, 2019.

17. Batarseh, S.I., Graves, R., San-Roman-Alerigi, D.P. and Chand, K.: "Laser Perforation: Lab to the Field," SPE paper 188729, presented at the Abu Dhabi International Petroleum Exhibition and Conference, Abu Dhabi, UAE, November 13-16, 2017.

18. Salehi, I.A., Gahan, B.C. and Batarseh, S.I.: "Laser Drilling — Drilling with the Power of Light: Final Report," Department of Energy (DOE) Report, February 2007, 318 p.

19. San-Roman-Alerigi, D.P., Batarseh, S.I. and Han, Y.: "Numerical Modeling of Thermal and Mechanical Effects in Laser-Rock Interaction — An Overview," paper presented at the 50th U.S. Rock Mechanics/Geomechanics Symposium, Houston, Texas, June 26-29, 2016.

20. Loh, K., Omrani, P.S. and van der Linden, R.: "Deep Learning and Data Assimilation for Real-Time Production Prediction in Natural Gas Wells," arXiv:1802.05141v2 [cs. LG], February 2018.

21. Batarseh, S.I., San-Roman-Alerigi, D.P., Reece, J. and Othman, H.A.: "Downhole High Power Laser Tools Development and Evolutions," SPE paper 193064, presented at the Abu Dhabi International Petroleum Exhibition and Conference, Abu Dhabi, UAE, November 12-15, 2018.

22. Graves, R.M., Batarseh, S.I., Parker, R.A. and Gahan, B.C.: "Temperatures Induced by High Power Lasers: Effects on Reservoir Rock Strength and Mechanical Properties," SPE paper 78154, presented at the SPE/ISRM Rock Mechanics Conference, Irving, Texas, October 20-23, 2002.

About the Authors

Dr. Sameeh I. Batarseh

Ph.D. in Petroleum Engineering, Colorado School of Mines

Dr. Sameeh I. Batarseh is a Petroleum Engineering Consultant working with the Production Technology Team of Saudi Aramco's Exploration and Petroleum Engineering Center – Advanced Research Center (EXPEC ARC). Currently, he is the Focus Area Champion of the Unconventional Resources leading the High-Power Laser Program. Sameeh's area of interest is to develop an in situ laser application in drilling, perforation and fracturing, among many other applications with a focus on unconventional reservoirs.

He is an active member of the Society of Petroleum Engineers (SPE), serving the society for several years while holding different positions, including sitting on the SPE Executive Advisory Committee, chairing the Program Committee and serving as session chair. He was also the board and vice chairman for the Western Region USA San Joaquin Valley. Sameeh's service is recognized worldwide as he received the SPE President Section Award of Excellence, Regional Service Award, and is a SPE Distinguished Lecturer. He has organized over 54 SPE technical workshops.

Sameeh has authored or coauthored more than 74 articles with high-impact publications, and has an H-Index of 36. He holds 48 patents (16 granted patents and has 32 patents in progress).

Sameeh received his Ph.D. degree in Petroleum Engineering from the Colorado School of Mines, Golden, CO.

Dr. Damian P. San-Roman-Alerigi

Ph.D. in Electrical Engineering, King Abdullah University of Science and Technology

Dr. Damian P. San-Roman-Alerigi is a Petroleum Scientist working with the Production Technology Team of Saudi Aramco's Exploration and Petroleum Engineering Center – Advanced Research Center (EXPEC ARC). His focus is on developing the next generation of subsurface photonic and electromagnetic tools.

Damian's previous research focused on the interaction of waves with complex media and its application to subsurface technologies. His work encompasses different areas of science and engineering, from oil and gas to applied mathematics. He has published papers in various international journals and conferences around the world.

Damian received his B.S. degree in Physics from the National Autonomous University of Mexico, Mexico City, Mexico. In 2008, he enrolled in King Abdullah University of Science and Technology (KAUST) as a founding class student where he completed his M.S. degree in 2010, and his Ph.D. degree in 2014, both in Electrical Engineering.

Abdullah M. Al-Harith

B.S. in Chemistry, University of Indianapolis

Abdullah M. Al-Harith is a Laboratory Technician Specialist working in the Production Technology Division of Saudi Aramco's Exploration and Petroleum Engineering Center – Advanced Research Center (EXPEC ARC). He has more than 15 years of experience working in different laboratory studies focusing on production enhancement technologies and research, specifically in stimulation and formation damages studies. In addition, Abdullah works on different unconventional resources research, including water treatment, microwave, laser and acoustic studies to increase oil recovery.

He received his A.S. degree in Industrial Laboratory Techniques from Jubail Industrial College, Jubail, Saudi Arabia. Abdullah received his B.S. degree in Chemistry from the University of Indianapolis, Indianapolis, IN.

Dr. Haitham A. Othman

Ph.D. in Petroleum Engineering, Texas Tech University

Dr. Haitham A. Othman is a Petroleum Engineer working with the Production Technology Team of Saudi Aramco's Exploration and Petroleum Engineering Center – Advanced Research Center (EXPEC ARC). Upon graduation in 2015, Haitham joined the High Power Laser Team. He is working on developing tools and methods for high power laser applications to tackle several Upstream production challenges.

Haitham has published several technical papers in international conferences.

He received his Ph.D. degree in Petroleum Engineering from Texas Tech University, Lubbock, TX.

Evaluation of an ENP Coating Material for Downhole Corrosion and Scale Protection in Sour Gas Wells

Dr. Tao Chen, Dr. Feng Liang, Dr. Fauken F. Chang, and Dr. Qiwei Wang

Abstract / An advanced downhole corrosion and scale monitoring (DCSM) tool was designed and developed to effectively monitor corrosion and scaling in high temperature sour gas wells. Several exchangeable, coated metal coupons were installed on the tool to evaluate the performance of the coating material. The tool was retrieved for post-laboratory analysis after three months of exposure to reservoir conditions.

The retrieved coupons were thoroughly characterized to assess the coating performance and to understand the corrosion and scaling mechanisms. X-ray diffraction (XRD) was used to analyze the composition of the coupon surface. Both scanning electron microscope (SEM) and energy dispersive X-ray spectrometer (EDS) analyses were performed to characterize the morphology and mineralogical changes of the coupon's surface. A surface profilometer was used to quantify the size, height, and depth of the coating surface.

The results showed that a thin layer — ~90 µm in thickness — composed of nickel (Ni) and sulfur (S), was formed on the surface of the coated coupon. A slight weight loss of the coated coupon was observed, which might be due to the combination of the effects of the reaction of the coating material with hydrogen sulfide (H_2S) — weight gain — and the abrasion of part of the outer layer from the surface — weight loss.

Overall, the field-test demonstrated that this newly developed coating material is able to effectively protect the metal coupon against corrosion and iron sulfide (FeS) scaling. The abrasion of the formed surface layer of millerite or nickel sulfide (NiS) scale might be a concern for long-term field application.

Introduction

Corrosion and scale deposition are common flow assurance issues in sour gas wells. Iron sulfide (FeS) deposition is an exotic scale deposited during oil and gas production, especially for deep sour gas wells producing from high-pressure, high temperature (HPHT) reservoirs. It can cause a flow assurance problem, such as the restriction of downhole surveillance and intervention[1-4].

Over the past few decades, great efforts have been made to understand the mechanisms and mitigation strategies of FeS deposition in downhole tubulars. Our previous study concluded that FeS surface deposition during the production stage is a corrosion induced scale issue[5]. The iron released from the tubing, due to corrosion during the production stage, is a source of FeS deposition in the tubular and surface facilities. The iron released from the tubing reacts with sulfide, and forms FeS surface deposition[5].

No metal is immune to corrosion in all environments. Through monitoring and understanding the environmental conditions that are the cause of corrosion, changing the metal type or applying coating materials to the metals can lead to significant reductions in corrosion, and further reduce FeS deposition in sour gas wells.

A newly developed electroless nickel-phosphorus (ENP) coating material was developed to reduce the corrosion induced FeS scale formation[6]. The ENP coating has several key advantages to provide corrosion resistance for sour oil and gas applications. These include a level of phosphorus imparting superior corrosion resistance in a sour gas environment, a tailored phosphorus level providing a range of super hydrophobic microstructures, and a second material introduced and embedded in the ENP coating during the coating process to impart the desired properties, such as wear- and erosion-resistance[6].

Figure 1 shows the surface profile of an ENP coated T-95 metal coupon. The peak-to-valley height for the surface profile of the ENP coated coupon was analyzed to understand the morphologies of the coating surface. The ENP coating was covered with nano-nodular structures, which were about 70 µm to 120 µm in diameter, and 5 µm to 10 µm in height, Fig. 1f. It was designed to enhance the hydrophobicity of the surface

Fig. 1 *The surface profile of an ENP coated T-95 coupon — general surface morphology analysis: (a) photograph of sliced metal coupon; (b) surface scan of 6 mm x 6 mm area (scan step was 2.6 µm); (c) fattened surface of image Fig. 1b; (d) magnified scan image of the blue-squared area in Fig. 1c (2 x 2 mm); (e) magnified scan image of the blue-squared area in Fig. 1d; and (f) height profile along the red line in Fig. 1e.*

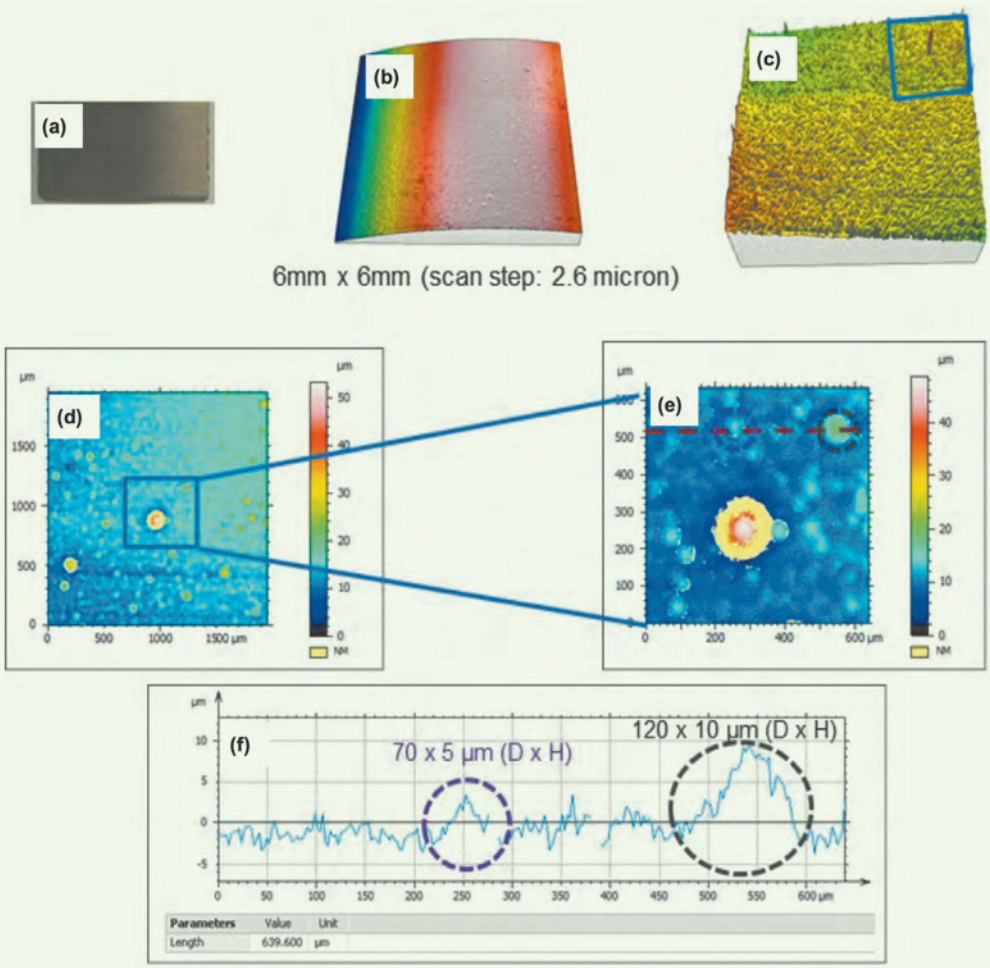

to minimize the corrosion to the metal surface and the induced scale deposition by reducing their contact and adherence to the coating surface[6].

The ENP coated coupons were tested in a rotating cage apparatus in a laboratory under a HPHT hydrogen sulfide (H_2S) atmosphere. The ENP coatings have shown effective prevention of the corrosion induced FeS scale deposition under laboratory test conditions, in comparison to the uncoated coupons, which scaled heavily under the same testing conditions. It also showed that the ENP coated coupon formed a tenacious, micro- to nano-crystalline Ni_3S_2 (Hazelwoodite) scale that has a very low affinity for FeS adhesion[6].

Although these laboratory tests were conducted using conditions such as temperature and pressure from the field, it is still very challenging to correlate the laboratory results to the real field conditions since it is difficult to simulate the actual environment and downhole multiphase flow regime in the laboratory. Monitoring the performance of the new coating materials under real downhole conditions is still essential for their development and quantification.

This article presents the analysis of the corrosion and scale formation for ENP coating materials after their exposure in a sour gas well using a downhole corrosion and scale monitoring (DCSM) tool for three months.

Experimental Procedure

A newly developed DCSM tool was designed and developed for measuring the corrosion and scale formation of the coating material under downhole conditions in sour gas wells. Figure 2 is an image of the DCSM tool arrangement.

The DCSM tool includes two body segments. The upper body segment is a gauge hanger — an elongated member with an axial protrusion — which allows the downhole devices to be securely anchored in the wellbore. The gauge hanger can be set and retrieved using conventional slick lines. The lower body segment is composed of metal coupons and a coupon holder, with threads on the top to connect to the upper body segment.

Fig. 2 *The arrangement of the DCSM tool.*

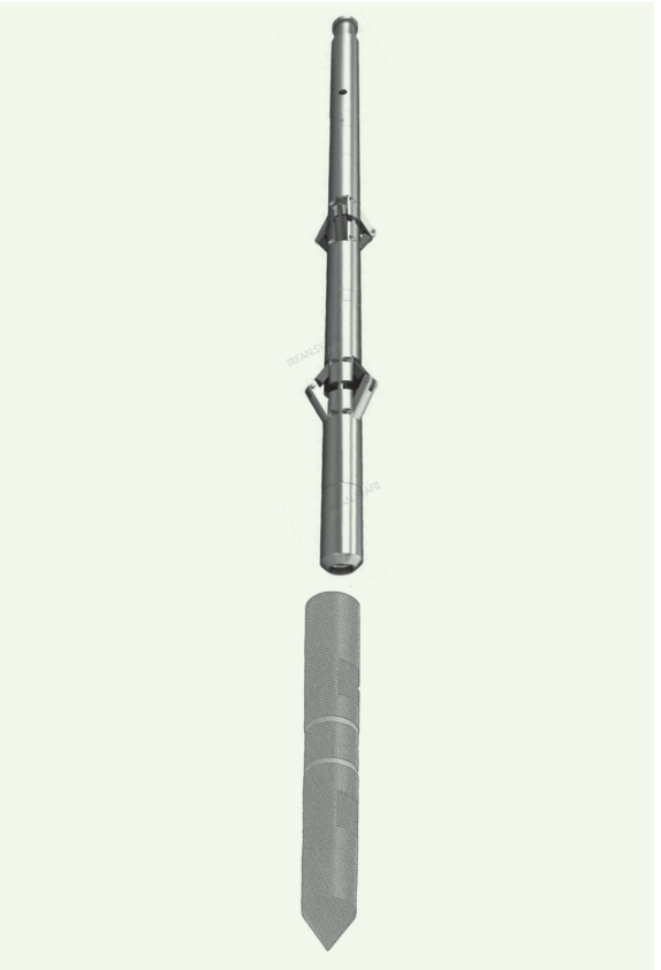

Several exchangeable metal coupons can be deployed on the tool to measure the rate of corrosion. This design represents significant improvements over the current industrial technology by directly measuring corrosion, scale deposition, and coating performance in real downhole conditions by using coupons made with identical metallurgy as the production tubing or coated coupons. The outer diameter of the metal coupons are the same as the coupon holder segments, and the metal coupon surface is exposed to similar flow regimes as the completion tubing to closely simulate the corrosion and scaling conditions. The concept of the tool development was approved, beginning with the laboratory design to the manufacturing process, and then on to field-testing.

The testing of the ENP coating material using the DCSM tool was carried out in a typical sour gas well, which contains ~5% H_2S and a 3% carbon dioxide gas stream at a temperature of ~125 °C, and a pressure of ~5,000 psi. The well has experienced severe FeS deposition in downhole tubulars. The metal test coupons attached to the DCSM tool were made with ENP coated T-95 carbon steel. After three months of exposure downhole, the DCSM tool was retrieved and the ENP coated metal coupon was taken out for post-laboratory analysis.

To understand the corrosion and scaling mechanisms, advanced analytical methods were performed on the retrieved ENP coated T-95 coupons, including weight change measurement, scanning electron microscope (SEM), energy dispersive X-ray spectrometer (EDS), X-ray diffraction (XRD), and surface profile measurement.

A ZEISS SIGMA HD-VP SEM was used for analyzing the morphologies of the inorganic scale deposition. An electron beam of approximately 15 kV scanned across a sample's surface. When the electrons strike the sample, a variety of signals, such as backscattered electrons, secondary electrons or X-rays from the interaction between the material and the electron beam are generated.

The detection of specific signals produces an image or a sample's elemental composition. A Bruker EDS was used to collect X-rays generated by the interaction. All elements — above a certain detection threshold — on the surface of the DCSM test coupons down to the atomic number of carbon, can be detected. The spectra are de-convolved in real time and chemical compositions were acquired. Both qualitative and quantitative analyses were performed.

A Bruker D8 Advance XRD was used to study the mineral composition of scale deposited on the surface of the DCSM test coupon. The Cu Kα X-rays (1.5418 Angstrom) were diffracted by the crystalline phases in the specimen according to Bragg's law ($\lambda = 2d \sin \theta$, where λ is the wavelength of the X-rays, d is the spacing between atomic planes in the crystalline phase, and 2θ is the angle between the incident and diffracted X-rays). The intensity of the diffracted X-rays was measured as a function of the diffraction angle and the specimen's orientation. The resulting diffraction pattern was loaded into Bruker's Diffrac-Eva (analytical) software, and the specimen's crystalline phases were identified against the International Center for Diffraction Data's PDF-4 database.

The measurement of the peak-to-valley height for the surface profile of test coupons is an important parameter to understand the morphologies of the scale surface. The surface of the coupon was scanned using a Nanovea PS50 profilometer, which was designed with leading edge chromatic confocal optical technology (axial chromatism) — compliant with the guidelines of both the International Organization for Standardization and the American Society for Testing and Materials International. The technique measures a physical wavelength directly related to a specific height without using complex algorithms.

Results

Figure 3a shows the photographs of the bare T-95 carbon steel coupon; Fig. 3b shows the ENP coated T-95 coupon before field application; and Fig. 3c

Fig. 3 *Photographs of the T-95 coupons: (a) T-95 carbon steel coupon; (b) The ENP coated T-95 coupon before field application; and (c) The ENP coated T-95 coupon retrieved after three-months of field exposure.*

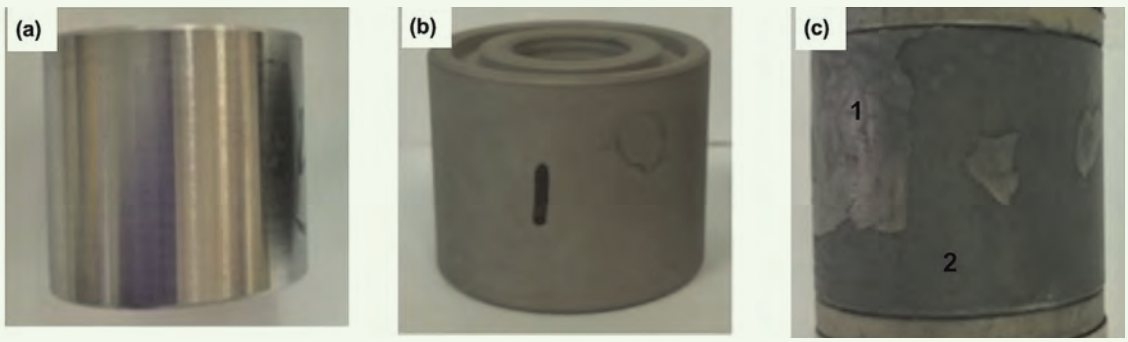

shows the ENP coated T-95 coupon retrieved after three-months of exposure in the field. The bare T-95 carbon steel coupon was shining without any deposition or corrosion. The surface of the ENP coated coupon appeared gray in color, and the coating seems to be uniform by visual inspection. The main body of the retrieved ENP coated T-95 coupon after three-months of field exposure was a darker shade with scattered top layers on the surface. It seems that most of the top layer (Layer 1, Fig. 3c) was abraded, and a darker second layer (Layer 2, Fig. 3c) was exposed to the surface.

The weight of the ENP coated T-95 coupon before and after field application is presented in Table 1. A slight weight loss of 0.229 g was calculated after the field application. The overall weight change may be due to the combination effects of two physical/chemical changes, the weight loss caused by corrosion/abrasion and the weight gain caused by the deposit formed on the surface of the ENP coated coupon.

The diameter of the T-95 carbon steel coupon and the ENP coated T-95 coupon were measured before and after three months of field exposure, Table 2. The diameter of the T-95 carbon steel coupon and the ENP coated coupon were 1.2300" and 1.2405", respectively. The calculated thickness of the ENP coating was about 0.0053" (133 µm), which was half of the diameter change. Two surface layers, the top surface and the secondary surface layers, were observed on the ENP coated coupon after the three-month field application.

The diameter of Layer 1 was 1.2445", 0.0040" (102 µm) more than the ENP coated coupon before the field application, which indicates that an approximate 0.0020" (51 µm) surface deposit formed onto the ENP coated coupon after the three-month field application. The diameter of Layer 2 was 1.2395", which was 0.0010" (25 µm) less than the ENP coated coupon before field application. This could be due to the removal of the top surface layer of the ENP coated coupon during the three-month field exposure.

Figure 4 shows the surface profile of the ENP coated coupon after the three-month field exposure. Similar to what was observed in Fig. 3c, and the diameter

Table 1 *The weight change of the ENP coated coupon before and after field application.*

	Weight Before (g)	Weight After (g)	Weight Change (g)
ENP coated T-95 coupon	121.546	121.317	-0.229

Table 2 *The diameter change of the T-95 carbon steel coupon, and the ENP coated coupons before and after field application.*

Coupon		Diameter (inch)	Diameter Change
T-95 carbon steel		1.2300	—
ENP coated coupon before field application		1.2405	0.0105 inch (267 µm)
Retrieved ENP coated coupon after three-months of field exposure	Top surface layer (Layer 1)	1.2445	0.0040 inch (102 µm)
	Second surface layer (Layer 2)	1.2395	-0.0010 (-25 µm)

Fig. 4 *The surface profile of the ENP coated coupon after a three-month field application: (a) Photographs of the part of the ENP coated coupon; (b) The surface scan of the blue-squared area in Fig. 4a (6 mm x 6 mm); (c) The magnified scan image of the blue-squared area in Fig. 4b (2 mm x 2 mm); and (d) The height profile along the red line in Fig. 4c.*

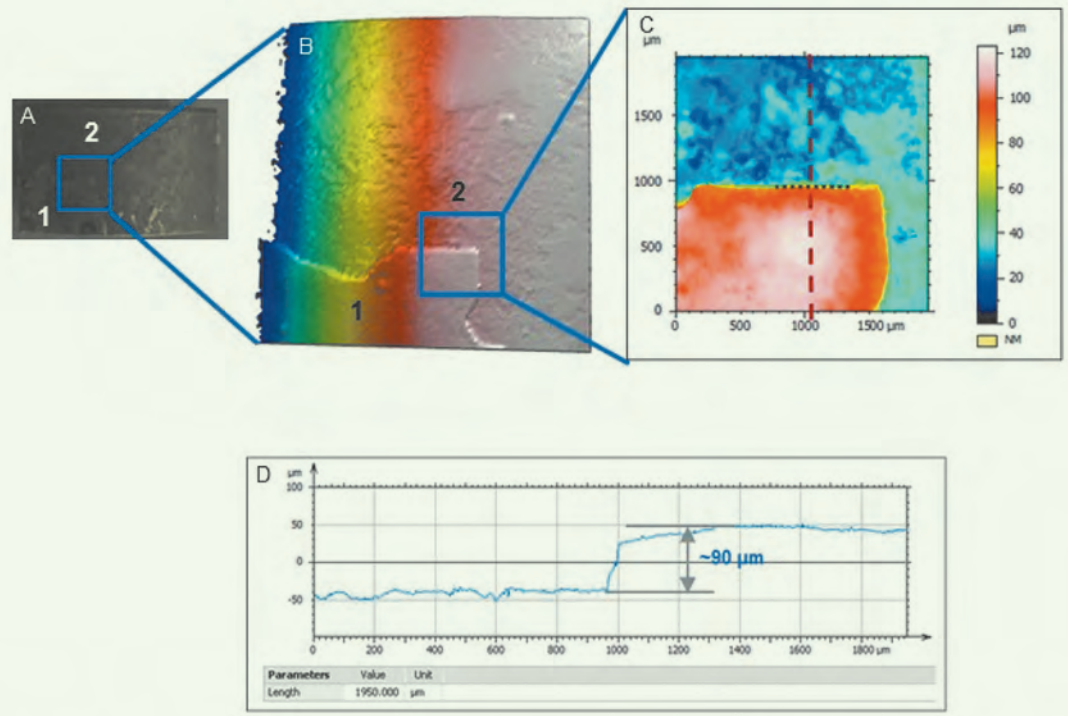

measurement in Table 2, two surface layers were detected for their height difference. The difference between Layer 1 and Layer 2 was calculated to be approximately 90 µm, Fig. 4d.

To quantify the surface changes due to the field exposure, high-resolution SEM images and EDS mapping, were taken on the cross-section of the ENP coated T-95 coupon sample before and after field exposure. Figure 5a shows a back-scattered electron image of the ENP coated T-95 coupon before the field application, and Figs. 5b to 5e show the elemental maps. The ENP coating was mainly composed of Ni, phosphorus (P),

Fig. 5 *The SEM image and EDS analysis of the cross-section of the ENP coated coupon before field application: (a) The back-scattered electron image; (b) The EDS analysis of Fe; (c) The EDS analysis of Ni; (d) The EDS analysis of P; and (e) The EDS analysis of Si.*

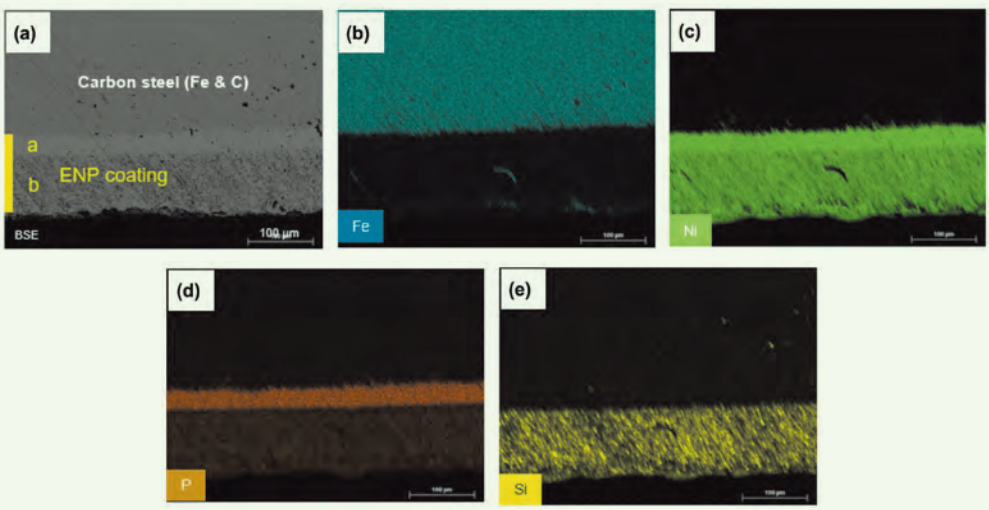

and Si. It was seen that the ENP coating was composed of two coating layers (Layer 1 and 2). Layer 1, which is directly coated onto the surface of the T-95 carbon steel, was approximately 30 µm and mainly composed of Ni and P. Layer 2 was coated on the top of the first layer, and was approximately 100 µm — mainly composed of Ni, Si, with a minor amount of P. The thickness of the ENP coating was approximately 130 µm, which is consistent with the thickness measurement determined from the T-85 coupon diameter measurement.

Figure 6 shows the high-resolution SEM images and EDS analysis on the cross-section of the ENP coated coupon sample with the top surface deposit layer after the three-month field exposure, to identify the thickness and elemental composition of the surface deposit. Figure 6a is a back-scattered image of the cross-section area. EDS analysis was also performed to determine the elemental analysis of the top surface deposit on the coating, Figs. 6b to 6f. It can be seen that the thickness of Layer a', which was part of the ENP coating, remains similar to the original coating, approximately 30 µm, while Layer b' was reduced from 100 µm to approximately 60 µm. Besides the main elements such as Ni, P, and Si, which existed in the original ENP coating, new element S was detected in the outer layer — Layer c', may comprise three sublayers — of the coupon sample. Layer c' was mainly composed of Ni and S and the thickness was approximately 90 µm. The thickness was similar to the thickness of Layer 1, previously seen in Figs. 3 and 4.

Figure 7 shows the high-resolution SEM images and the EDS analysis of the cross-section of the ENP coated coupon sample with a second surface layer (Layer 2 in Figs. 3 and 4) after three-months of field exposure. Figure 7a is a back-scattered image of the cross-section area. Similar to what was observed in Fig. 6, S was detected in the outer layer (Layer c"). The thickness of Layer c" was approximately 10 µm to 20 µm, thinner than Layer c'.

An XRD analysis was carried out to further analyze the mineralogy of the surface deposit on the ENP coated coupon after three-months of field exposure. The surface deposit was composed of two types of sulfide scales, including millerite (NiS) and violarite ($Fe^{2+}Ni_2^{3+}S_4$), Fig. 8. In addition, silicon carbide was detected, which could be part of the ENP coating.

Discussion

Performance of the ENP Coating after Downhole Exposure

According to Chen's study[3], the iron released from the tubing due to tubing corrosion is one of the major iron sources for FeS deposition on downhole tubulars. The iron released from the tubing due to corrosion reacts with H_2S to form FeS scale. There was no FeS crystals detected by XRD analysis on the surface of the ENP coating after three-months of field exposure. The main scale formed on the outer surface layer was NiS. This may be due to the higher reactivity of H_2S with Ni, which was present in the ENP coating. The field test demonstrated that the ENP coating could effectively protect the T-95 carbon steel coupon from direct contact with a highly corrosive sour production environment. No corrosion or iron release was observed from the carbon steel tubing, so that it further prevents the deposition of FeS scale.

In addition, the ENP coating has a nano-nodular structure, approximately 70 µm to 120 µm in diameter, and 5 µm to 10 µm in height, as previously seen in Fig. 1f. It was designed to enhance hydrophobicity and make it difficult for a FeS deposit to achieve sufficient contact with the surface to adhere[6]. The hydrophobic

Fig. 6 *The SEM image and the EDS analysis of a cross-section of the retrieved ENP coated coupon with a top surface deposit layer (Layer 1) after the three-month field exposure: (a) The back-scattered electron image; (b) The EDS analysis of Fe; (c) The EDS analysis of Ni; (d) The EDS analysis of P; (e) The EDS analysis of Si; and (f) The EDS analysis of S.*

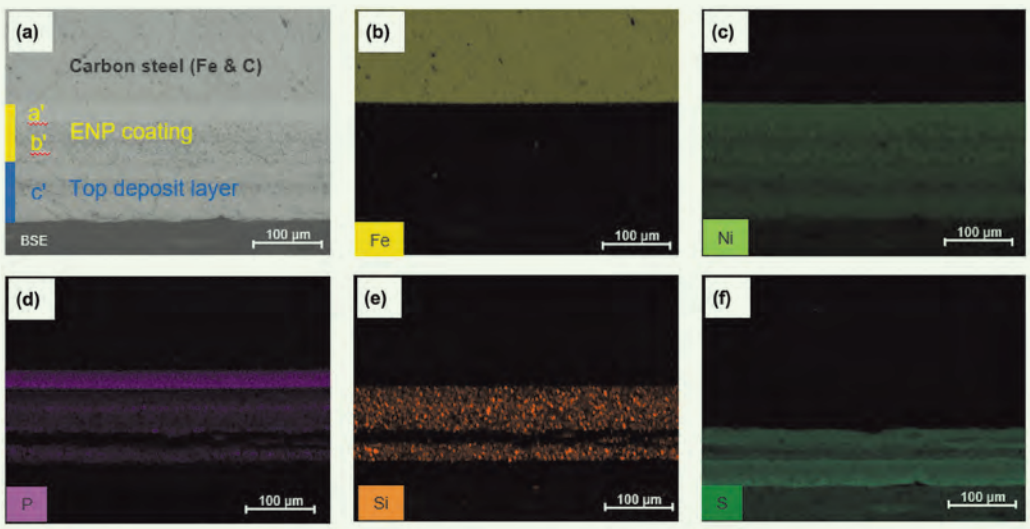

Fig. 7 *The SEM image and the EDS analysis of the cross-section of the retrieved ENP coated coupon with a second surface deposit layer (Layer 2): (a) The back-scattered electron image; (b) The EDS analysis of Fe; (c) The EDS analysis of Ni; (d) The EDS analysis of P; (e) The EDS analysis of Si; and (f) The EDS analysis of S.*

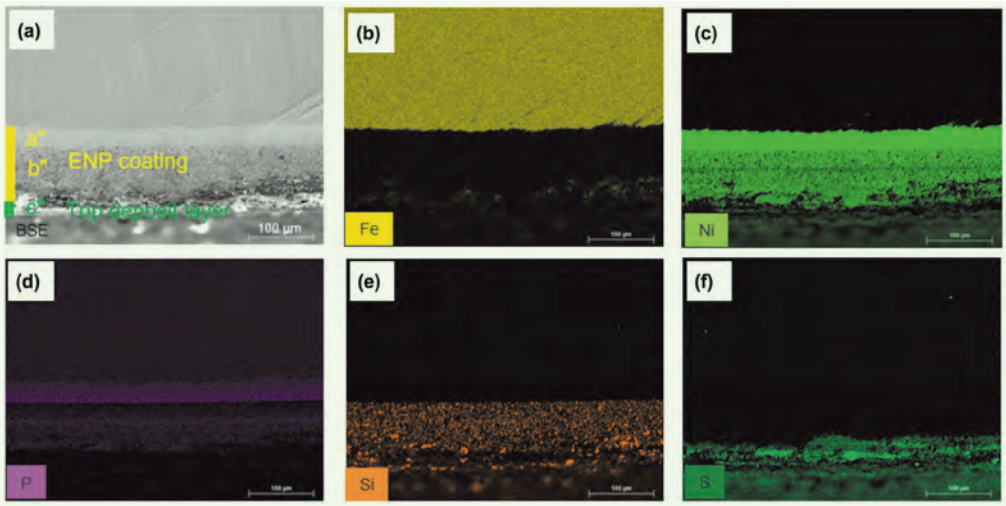

Fig. 8 *The XRD composition analysis of the surface deposition on the ENP coated coupon after three-months of exposure in reservoir conditions.*

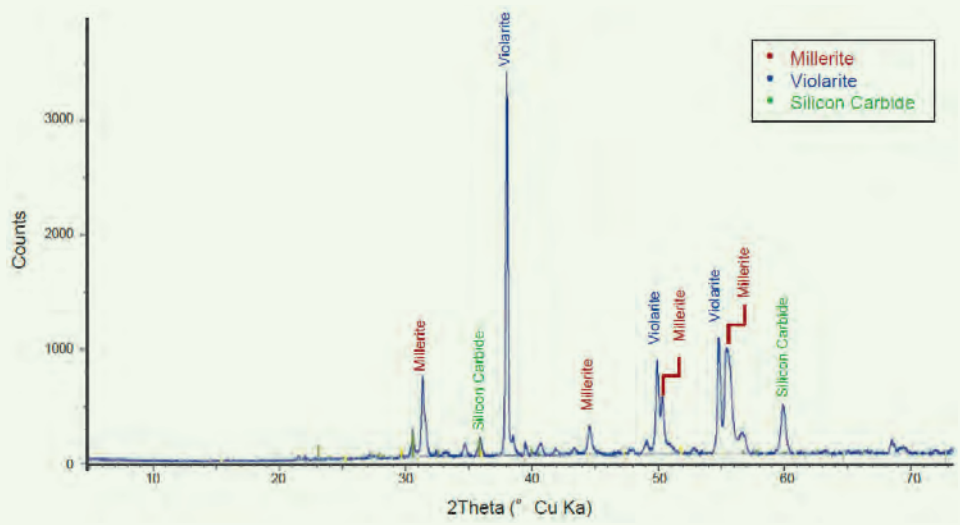

characteristic of the ENP coating could effectively prevent the adhesion of FeS crystals from forming bulk precipitation — if there is any.

The field application has effectively demonstrated that this newly developed ENP coating material is able to protect the metal coupon against corrosion and FeS scaling. The abrasion of the formed surface layer of NiS scale might be a concern for the long-term field application.

Difference between Laboratory Test and Field Test

The ENP coated coupons were tested in a rotating cage apparatus under a HPHT H_2S atmosphere in a laboratory. The ENP coatings effectively prevented the corrosion induced FeS scale deposition. It showed very low affinity for FeS adhesion[6]. These conclusions drawn from the laboratory tests were in agreement with the conclusion derived from the three-month field exposure under real downhole conditions.

The morphologies of the NiS formed in laboratory conditions (Ni_2S_3) are different with the morphology formed in the real downhole conditions (NiS). Violarite formed in the field application, which did not form under laboratory conditions. In addition, the abrasion of the top layer of NiS — one of the major concerns for the long-term field application — was observed during the three-month field-test, instead of under

laboratory conditions.

This could be caused by the difference between the flow regime in the field condition and the designed testing condition in the laboratory. This indicates that although the laboratory tests were conducted using conditions such as temperature and pressure from the field, it is still very challenging to correlate the laboratory results to the real field conditions since it is difficult to simulate the actual environment and downhole multiphase flow regime in the laboratory. The monitoring of the corrosion, scale, and coating performance under real downhole field conditions is still essential for developing and qualifying new coating materials for field applications.

Conclusions

1. The newly developed DCSM tool has an advanced design allowing direct corrosion and scale monitoring under downhole conditions in sour gas wells. This can be applied to evaluate the performance of the coating materials under real downhole conditions. In combination with the post-laboratory analysis on the retrieved coupons, the tool can provide corrosion and scale mechanism for specific metallurgy or coating materials in sour gas wells, and proper corrosion and scale management programs could be designed to minimize the effects of corrosive gases. This developed tool can monitor the effectiveness of the corrosion treatment, and can be deployed in sweet gas wells, oil wells, and water supply wells.
2. The field-test demonstrated that a thin layer (~90 μm in thickness) composed of Ni and S formed on the surface of the ENP coated coupon after its exposure in the high H_2S environment for three months. This newly developed ENP coating material is effectively able to protect the metal coupon against corrosion and FeS scaling. The abrasion of the formed surface layer of NiS scale might be a concern for long-term field application.
3. The monitoring of the corrosion, scale, and coating performance under real downhole field conditions is still essential for developing and qualifying new coating materials for field applications.

Acknowledgments

The authors would like to acknowledge Amro Mukhles and Esmael Albelharith for the field application support, Jilin Zhang for the XRD analysis and Jordan Kone and Joshua Brothers for the SEM analysis.

References

1. Leal Jauregui, J.A., Solares, J.R., Nasr-El-Din, H.A., Franco, C.A., et al.: "A Systematic Approach to Remove Iron Sulfide Scale: A Case History," SPE paper 105607, presented at the SPE Middle East Oil and Gas Show and Conference, Manama, Kingdom of Bahrain, March 11-14, 2007.
2. Wang, Q., Ajwad, H., Shafai, T. and Lynn, J.D.: "Iron Sulfide Scale Dissolvers: How Effective Are They?" SPE paper 168063, presented at the SPE Saudi Arabia Section Technical Symposium and Exhibition, al-Khobar, Saudi Arabia, May 19-22, 2013.
3. Chen, T., Wang, Q. and Chang, F.F.: "Understanding the Mechanisms of Iron Sulfide Formation in Sour Gas Wells," paper presented at the 16th Middle East Corrosion Conference and Exhibition, Manama, Kingdom of Bahrain, February 8-11, 2016.
4. Wang, Q., Leal Jauregui, J.A., Syafii, I., Mukhles, A.E., et al.: "Iron Sulfide and Removal in Scale Formation Sour Gas Wells," SPE paper 179869, presented at the SPE International Oil Field Scale Conference and Exhibition, Aberdeen, Scotland, U.K., May 11-12, 2016.
5. Lu, P., Chen, T., Wang, Q. and Chang, F.F.: "New Understanding on Iron Sulfide Deposition during Acid Stimulation in Sour Gas Wells," paper presented at the NACE International Conference and Exposition CORROSION 2018, Phoenix, Arizona, April 15-19, 2018.
6. Kool, L., Zhu, H., Wang, Q. and Chang, F.F.: "Development of Scaling-Resistant Coatings for High Temperature Sour Gas Service," paper presented at the NACE International Conference and Exposition CORROSION 2018, Phoenix, Arizona, April 15-19, 2018.

About the Authors

Dr. Tao Chen

Ph.D. in Chemical Engineering, Heriot-Watt University

Dr. Tao Chen is a Petroleum Engineering Specialist working with the Production Technology Team of Saudi Aramco's Exploration and Petroleum Engineering Center – Advanced Research Center (EXPEC ARC). His interests are production chemistry and flow assurance in the oil and gas industry, specializing in oil field scale management.

Prior to joining Saudi Aramco in 2014, Tao spent more than 15 years on oil field scale management and worked at Clariant, Champion Technologies, Nalco Champion, and LR Senergy in Aberdeen, U.K.

He has published over 90 technical publications about scale management in oil fields.

Tao received both his B.S. and M.S. degrees in Chemical Engineering from Dalian University of Technology, China, and his Ph.D. degree in Chemical Engineering from Heriot-Watt University, Edinburgh, U.K. Tao also received an MBA from Warwick University, Coventry, U.K.

Dr. Feng Liang

Ph.D. in Organic Chemistry, Rice University

Dr. Feng Liang is currently a Research Science Specialist at the Aramco Americas (formally Aramco Services Company (ASC)), Aramco Research Center-Houston. She has now been with the company for over five years.

Prior to joining the Aramco Research Center, Feng was a Principal Scientist at Halliburton for nearly eight years. Her research interests are the new materials and product development in fracturing fluid, advanced fluid additives, waterless fracturing technologies, biodegradable diversion materials, sand control products, cement additives, and nanomaterials reinforced elastomers.

Feng is a contributor to many patents and technical papers. She holds over 40 issued U.S. patents and 30 additional published patent applications. Feng is the author and coauthor of more than 60 technical papers, with a few in very high impact factor journals such as the *Journal of the American Chemical Society* and *Nano Letters*. She has also coauthored two book chapters as well. Feng's publications have received over 3,000 citations.

She is a member of the Society of Petroleum Engineers (SPE) and the American Chemical Society (ACS). Feng received the 2017 SPE Production and Operations Award for the Gulf Coast North American Region. She also received the 2017 Effective Publication Award from Saudi Aramco's Exploration and Petroleum Engineering Center – Advanced Research Center (EXPEC ARC).

Feng received her Ph.D. degree in Organic Chemistry from Rice University, Houston, TX.

Dr. Fakuen "Frank" F. Chang

Ph.D. in Petroleum Engineering, University of Oklahoma

Dr. Fakuen "Frank" F. Chang is the focus area champion for Productivity Enhancement in the Production Technology Team of Saudi Aramco's Exploration and Petroleum Engineering Center – Advanced Research Center (EXPEC ARC).

Prior to joining Saudi Aramco in September 2012, he worked at Schlumberger for 16 years. Before that, Frank was at Stimlab for 4 years. He has developed many products and technologies dealing with sand control, fracturing, acidizing, and perforating.

Frank is an inventor and recipient of 23 granted U.S. patents, and he is the author of more than 40 Society of Petroleum Engineers (SPE) technical papers.

Frank received his B.S. degree in Mineral and Petroleum Engineering from the National Cheng Kung University, Tainan City, Taiwan; his M.S. degree in Petroleum Engineering from the University of Louisiana at Lafayette, Lafayette, LA; and his Ph.D. degree in Petroleum Engineering from the University of Oklahoma, Norman, OK.

Dr. Qiwei Wang

Ph.D. in Oceanography, Texas A&M University

Dr. Qiwei Wang works in Saudi Aramco's Research & Development Center as a Science Specialist in oil field scale mitigation. Since joining Saudi Aramco in 2011, he has played a key role in all major scale mitigation activities and led the completion of over 60 projects. Before joining Saudi Aramco, Qiwei worked with Nalco Champion as a R&D Coordinator on flow management and as a Senior Specialist on scale management. He has over 25 years of R&D and technical support experience in oil field production chemistry, scale management, and water treatment.

Qiwei is an active member of the Society of Petroleum Engineers (SPE) and National Association of Corrosion Engineers (NACE). He has organized workshops, served on technical committees, and has chaired several conferences for both organizations.

He has authored and coauthored over 150 publications and 20 U.S. patent applications.

Qiwei received his B.Eng. degree in Chemical Engineering from Taiyuan University of Science and Technology, Taiyuan, China; an M.Eng. degree in Material Sciences from Harbin Institute of Technology, Harbin, China; an M.S. degree in Chemistry from the University of Ryukyus, Okinawa, Japan; and a Ph.D. degree in Oceanography from Texas A&M University, College Station, TX.

Mitigating Drilling Hazards in a High Differential Pressure Well Using Managed Pressure Drilling and Cementing Techniques

Peter I. Egbe and Carlos O. Iturrios

Abstract /

Formation pressure heterogeneity in a reservoir can represent a significant challenge when a high overbalance condition is created in a zone with low pore pressure; leading to total losses, and potential stuck pipe events, which subsequently increase well costs and nonproductive time. This article describes a case involving high differential pressure between the heel of the reservoir, and toe of the lateral, and where drilling in an up dip direction increased the complexity of the operation.

The original well design considered drilling the entire reservoir section in one 6⅛" section. Although, to mitigate identified operational challenges, the 7" liner depth was adjusted to cover the high-pressure section of the reservoir, thereby isolating the weaker reservoir zones at the total depth (TD) of the well. Managed pressure drilling (MPD) was deployed to drill both sections to reduce the overall overbalance condition and to provide an additional method to determine the pore pressure. Furthermore, the 7" liner was run in MPD mode to minimize the chances of differential sticking; and cemented in place using the managed pressure cementing (MPC) technique to mitigate against inducing downhole losses during the cementing operation, which would have impacted zonal isolation efficiency, and the long-term well integrity leading to possible sustained casing pressures.

MPD is an adaptive drilling technique that is used to precisely assess the formation pressure and manage the bottom-hole pressure (BHP) accordingly. MPD allows the use of a lighter mud density to reduce the overbalance condition, and by manipulating the annular surface pressure, a condition of constant BHP can be maintained. MPD was implemented to determine the formation pressure and define the optimal mud density for the operation during drilling, and while running and cementing the liner, thereby mitigating the risk of potential losses and differential stuck pipe.

Introduction

The continuous demand for hydrocarbons for multiple purposes has led to the necessity of exploring new ways to develop new or existing oil fields to keep up with the ever-increasing demand. Subsequently, the complexity to reach these reservoirs has proven to be constantly increasing, not only because some of these fields have been under production for many years but also due to the requirement of optimizing reservoir contact, minimizing formation damage, and drilling with the lowest possible nonproductive time.

One of the strategies of the operator to maintain the production rate in these mature fields is to drill power water injector wells to maintain reservoir pressure and increase oil recovery. Consequently, such a strategy comes with its own challenges, like formation pressure heterogeneity and rapid change in formation pressure within the same hole section. For this operator, previous campaigns in the field showed that these conditions generated a significant increment in the nonproductive time due to differential sticking and lost circulation when using conventional drilling techniques.

To overcome the identified challenges, managed pressure drilling (MPD) in its variant of constant bottom-hole pressure (BHP) was implemented in the well used for this article, to evaluate the actual formation pressure and manage the BHPs accordingly. This allowed us to obtain relevant data that permitted making the proper decisions and eliminating the nonproductive time associated to differential stuck pipe and downhole fluid losses.

This article highlights the drilling and liner cementing operations as executed, using the MPD technique in this power injector well. The target reservoir presented high formation pressure heterogeneity with an expected difference between the heel and toe of the reservoir of ±51 pounds per cubic ft (pcf) equivalent at the well's total depth (TD). The results and conclusions for the project are subsequently discussed.

MPD

MPD utilizes an underbalanced mud density, which when combined with the annular surface pressure, maintains the overbalance condition at all times with a target BHP close to the formation pressure[1]. While drilling or

circulating, the frictional pressure losses in the annulus maintain the BHP above the formation pressure, and in static conditions, the surface back pressure (SBP) is adjusted with the MPD choke to maintain a constant BHP, and the overbalanced condition.

In MPD, the following expression holds: $P_{bottom\text{-}hole} = P_{hydrostatic} + P_{friction} + P_{choke}$.

Additionally, the use of a mud density lower than the conventional requirement — and below the formation pressure — allows the performance of MPD pore pressure tests. The pore pressure test is a useful capability to determine the actual pore pressure and optimize the drilling parameters accordingly[2].

To implement the MPD technique, additional surface equipment is needed to be rigged up and connected to the existing rig equipment to allow for the pressurization of the annular space.

A rotating control device (RCD) is installed on top of the annular blowout preventer, allowing the circulating system to open to the atmosphere to convert into a closed loop one; while also diverting the returns of the well to the MPD choke manifold. The MPD choke manifold adjusts the annular SBP to manipulate the annular pressure profile and achieve the desired equivalent circulating density (ECD).

Figure 1 shows all of the MPD system components, which are designed, qualified, tested, and maintained as per the various industry API and ISO standards[3].

Figure 2 illustrates the drilling mud flow path with the MPD system rigged up.

Pre-Drilling Planning

Characteristics of the Well

For the well selected for this article, it was planned to drill an 8½" section and a 6⅛" section across the formation of interest. Due to the high differential pressure expected in the target formation, the 7" liner setting point was optimized to cover ±1,400 ft inside the said formation. This was designed to minimize the differential pressure at which the 6⅛" section was going to be exposed. Figure 3 is a diagram of this well.

The overall objectives of the MPD application in this well were as follows:

- Evaluate the formation pressure limits via MPD pore pressure tests.
- Based on the evaluated formation pressure, adjust the mud weight (MW) and SBP to ensure the optimum required overbalance was used to drill the reservoir section.
- Using the optimum overbalance, minimize or eliminate the potential for induced downhole losses, and possible differential stuck pipe event while drilling both sections.
- Deploy and cement the 7" liner using the managed

Fig. 1 *The components of the MPD system.*

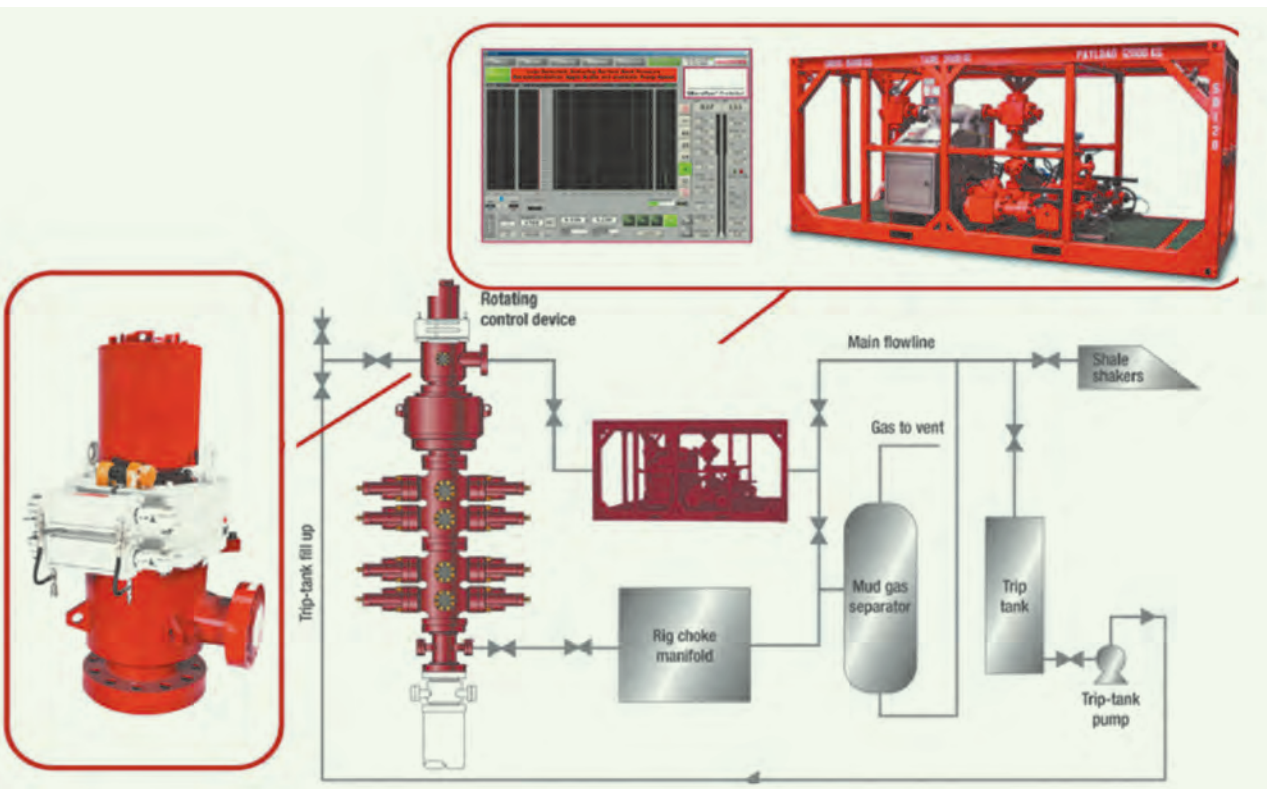

Fig. 2 *The MPD system's flow path while drilling.*

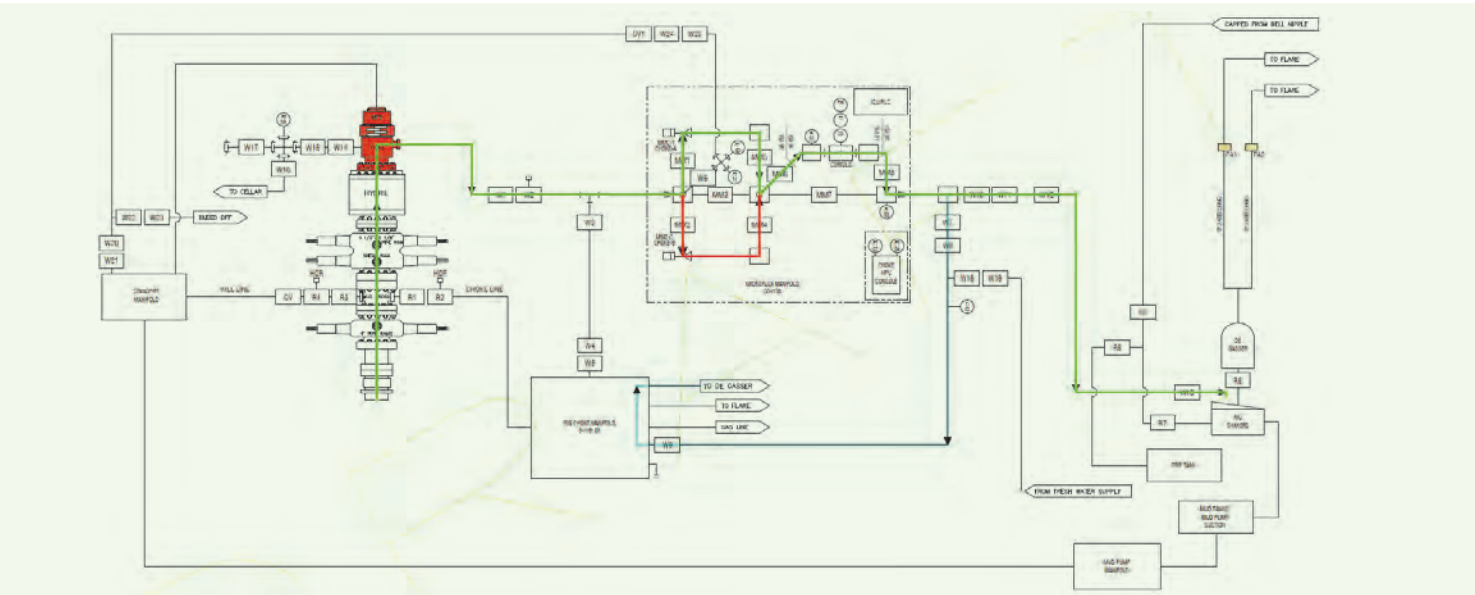

Fig. 3 *Well diagram.*

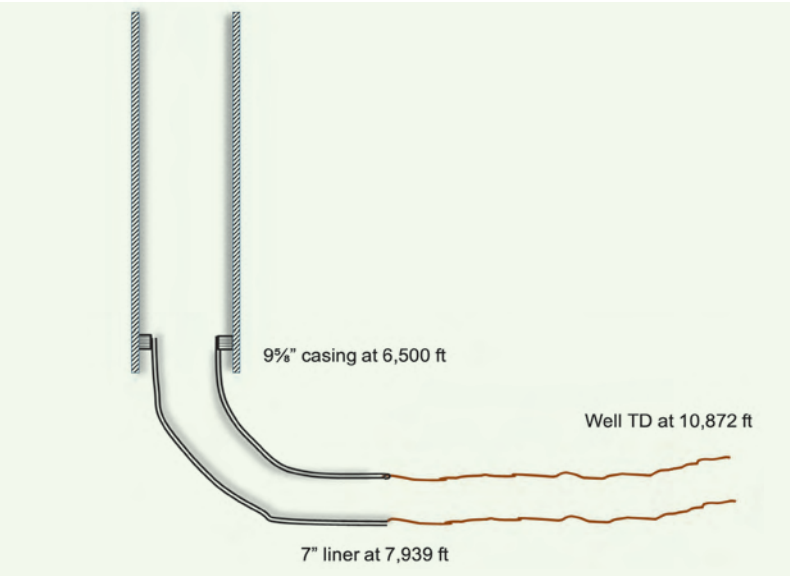

pressure cementing (MPC) technique.

- Save the additional cost of building and maintaining high MWs.
- Ensure minimal near wellbore formation damage due to the use of drilling fluids with high barite content.

Mud Density and Target ECD Selection

To determine the initial target ECD, the MPD approach is to use the conventional mud density as a starting point, and then adjust accordingly based on the results of the MPD pore pressure test. For the case well, the initial target ECD for the 8½" hole section was selected at 106 pcf, to maintain the required 200 psi overbalance as per the operator's policy.

To determine the most suitable combination of mud density and SBP, several hydraulic simulations were prepared, and the results were used to generate the MPD control windows for both sections. In these windows, four different mud densities are predicted as the base. For the case of the 8½" section, 80 pcf, 85 pcf, 90 pcf, and 95 pcf were used. Whereas for the 6⅛" section, 65 pcf, 70 pcf, 75 pcf, and 80 pcf were used to generate the MPD control window.

Figures 4 and 5 show the MPD control windows for the 8½" section for the dynamic and static conditions, respectively. Also, it can be seen that to generate the target ECD of 106 pcf of mud density, 85 pcf was selected, assisted with the pump rate of 550 gallons per minute (GPM), and a SBP of 565 psi. The flexibility of the range of possible mud density to use is given by the pressure rating of the RCD, plus a safety factor. For the operations in this case study, it allowed a significant reduction in the mud density (compared to the conventional mud design) of up to 600 psi — equivalent to 21 pcf.

Figures 6 and 7 show the MPD control windows in the 6⅛" section for the dynamic and static conditions, respectively. The target ECD for this section was selected based on the expected pore pressure at the 7" liner shoe depth, 89 pcf.

To generate 89 pcf of ECD, it was recommended to use 70 pcf of mud with a pump rate of 300 GPM, and a SBP of 550 psi. This combination was assessed to allow for a good range of adjustment in case a lower than expected pore pressure was encountered.

Fig. 4 *The MPD control window for the 8½" section in dynamic conditions.*

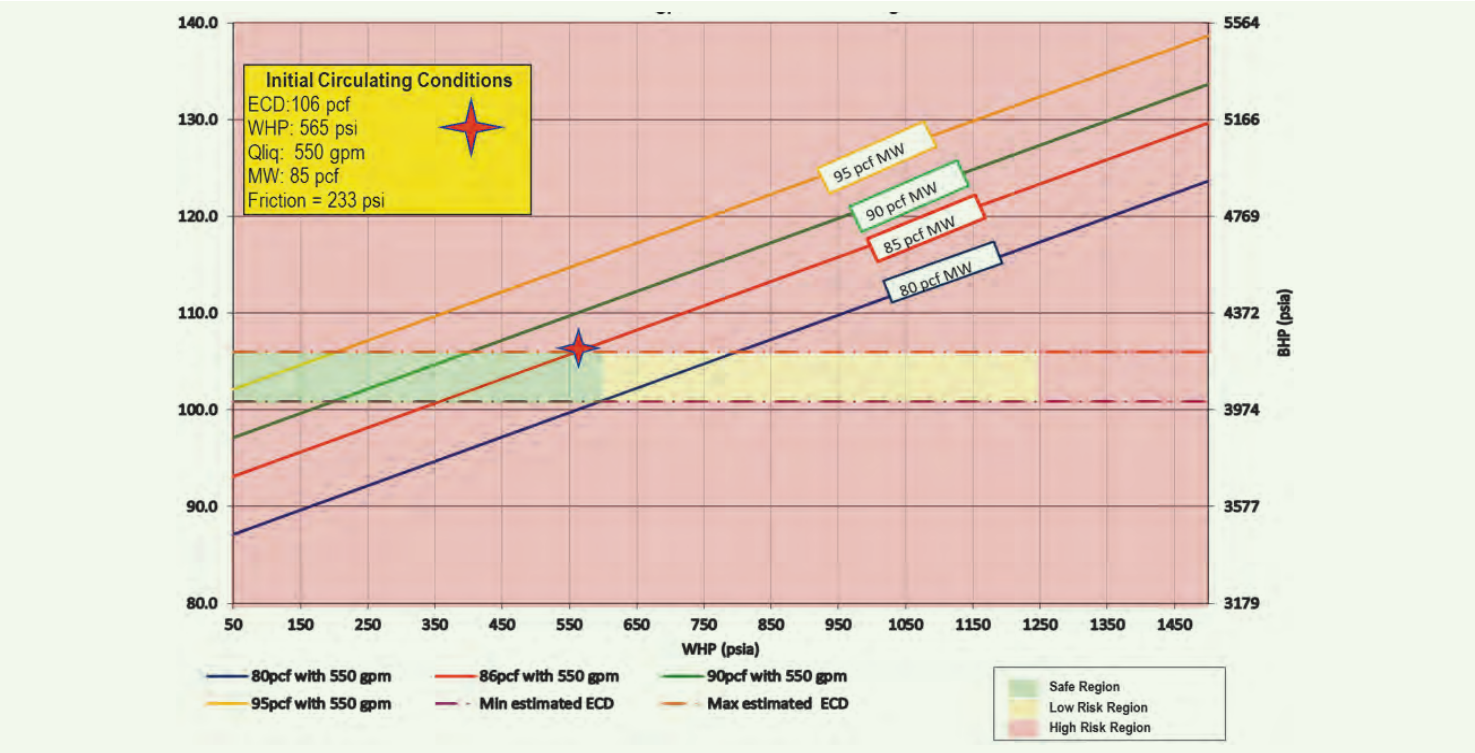

Fig. 5 *The MPD control window for the 8½" section in static conditions.*

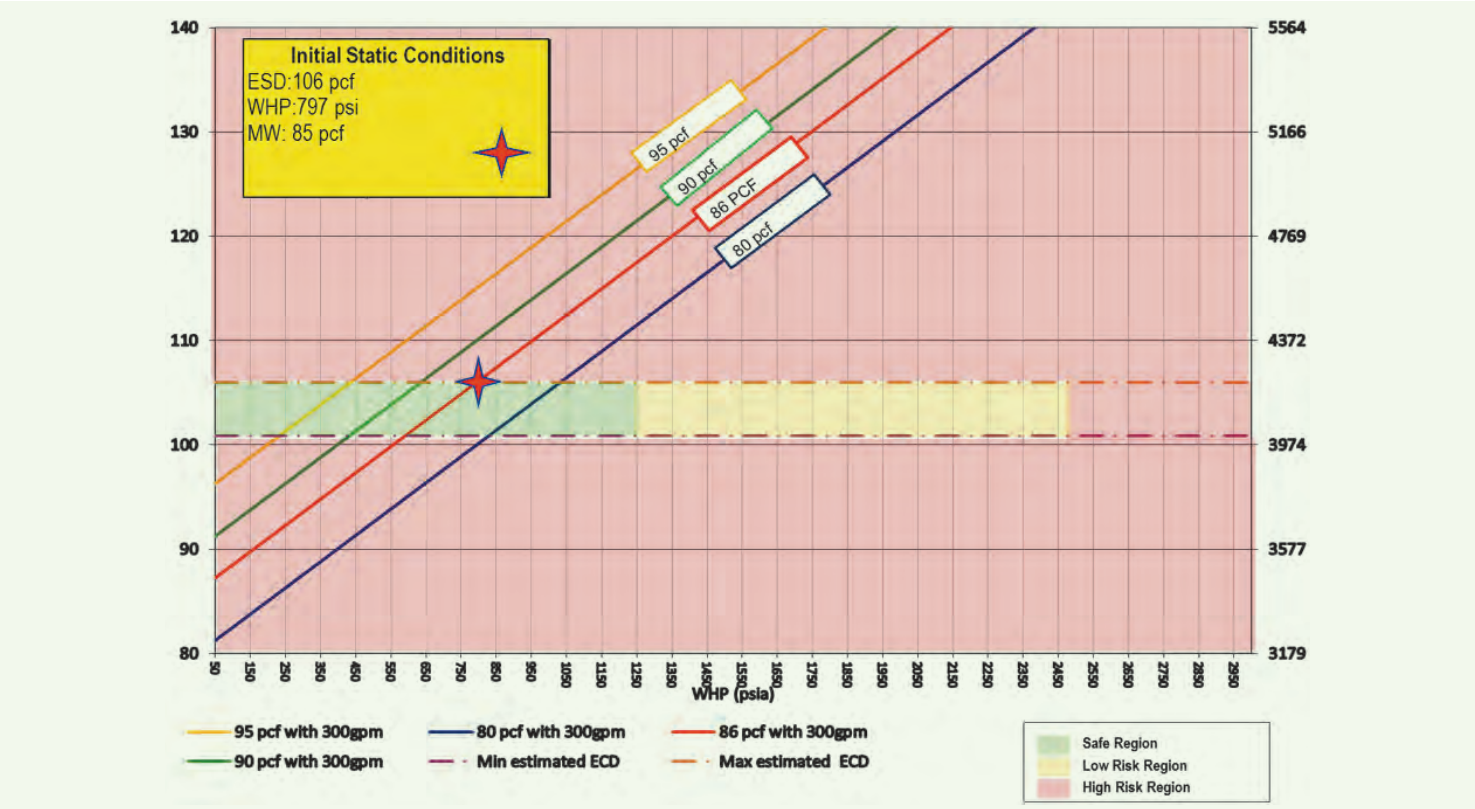

Fig. 6 *The MPD control window for the 6⅛" section in dynamic conditions.*

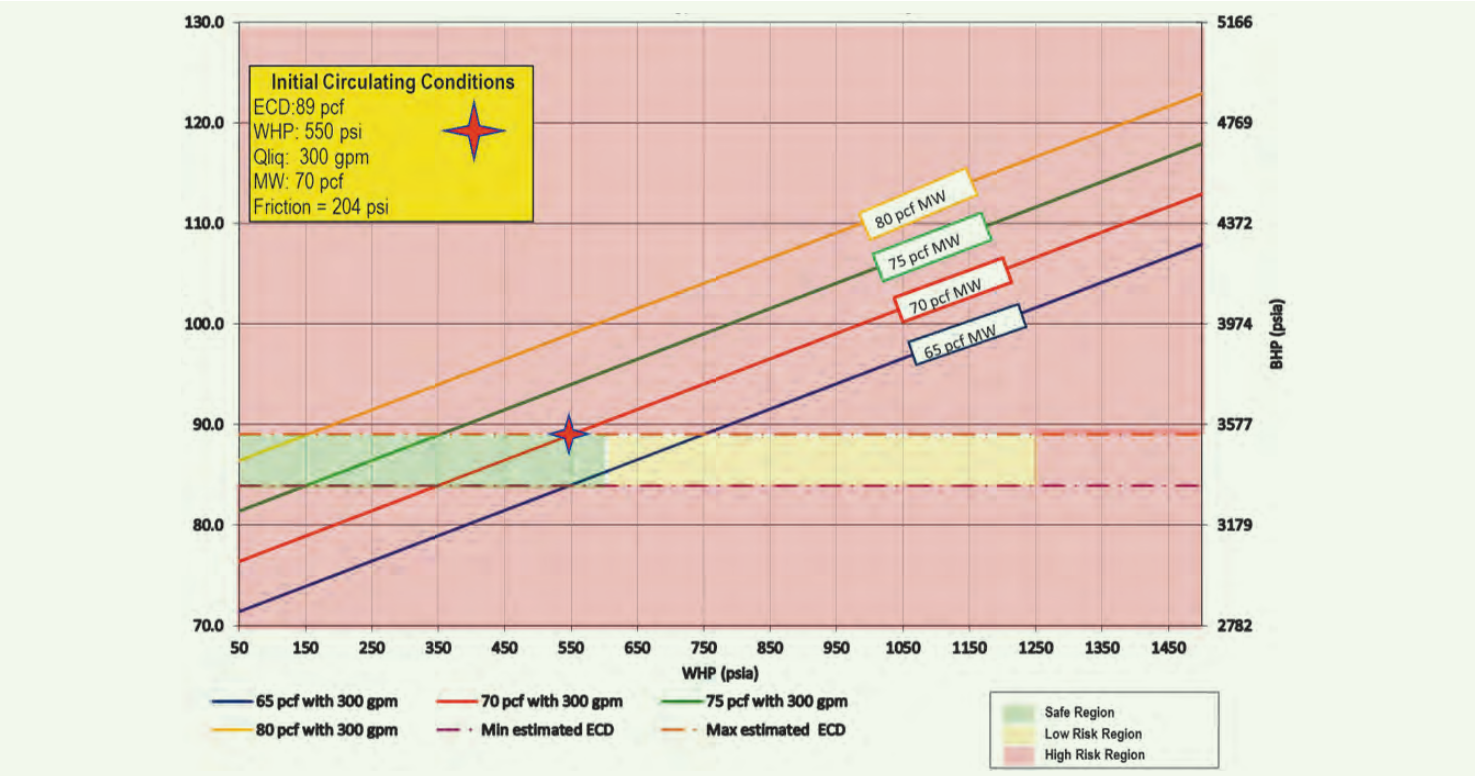

Fig. 7 *The MPD control window for the 6⅛" section in static conditions.*

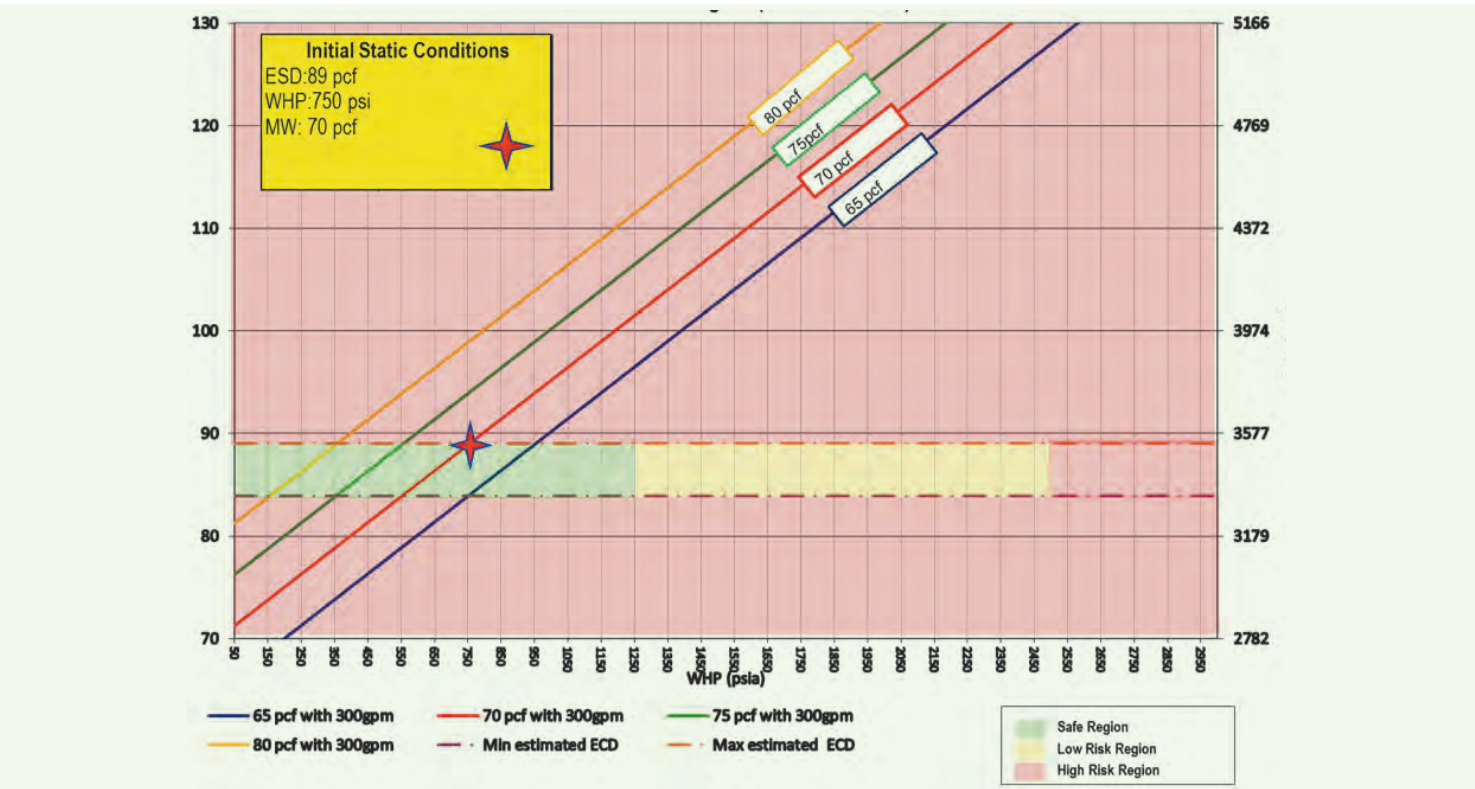

MPD Well Control Matrix

MPD operations deal with complicated scenarios, which in many cases like this case study, where an underbalanced drilling fluid weight — less than conventional MW requirement — is used. Uncertainties in the pore pressure can lead to the influx of unwanted reservoir fluids into the wellbore.

The MPD can deal with these scenarios within the established boundaries set by the MPD equipment pressure rating or pre-agreed limits defined with the operating company. Once these limits are exceeded, a transition needs to be made to conventional well control.

Table 1 is the MPD well control matrix, which indicates the actions that need to be taken in case an influx is detected and defines the limits or boundaries at which the control of the well is handed back to the rig/well operator[2].

Job Execution

Drilling of the 8½" Hole Section

The MPD equipment and crew arrived at the specified location during the running of the 9⅝" casing operation. This was planned to allow enough time for the training sessions with the rig crew and key personnel at the location, regarding the MPD operation.

Prior to commencing drilling operations, the fingerprinting and calibration of the MPD equipment was done, which included a hands-on practice with the rig crew covering the main procedures in which the rig personnel would be involved, e.g., connections or well control events. Once the calibration and fingerprinting procedures were completed, and after tripping to above the 9⅝" casing shoe, the well was displaced from the conventional mud density of 106 pcf to the MPD mud density of 86 pcf, while managing the annular SBP to maintain an ECD of 106 pcf.

The drilling of the 8½" phase started under these conditions until reaching 6,714 ft — 214 ft inside the target formation as confirmed by the geological samples. At this depth, an MPD pore pressure test was performed to assess the actual formation pressure. Prior to the pore pressure test, the hole was circulated clean as required by the standard pore pressure test procedure, and then the annular surface pressure was reduced gradually in steps of 1 pcf per periods of 1 to 2 minutes.

As observed in Fig. 8, the SBP (white curve) was reduced from 780 psi (for an equivalent static density (ESD) of 106 pcf) to 60 psi (for an ESD of 88 pcf), while monitoring the flow in (blue curve), and the flow out (red curve). No signs of an influx were detected.

After the MPD pore pressure test procedure, a pressure point was taken with the logging while drilling (LWD) BHP reading tool in the bottom-hole assembly. The LWD tool measured a pore pressure of 95 pcf in a static period of 15 minutes. It was determined that the MPD pore pressure test was affected by the formation fluid mobility, which required significantly longer waiting times for stabilization to occur. Based

Table 1 *MPD well control matrix[2].*

MPD Well Control Matrix

Normal Operations No influx (100 psi to 500 psi)		Influx Detected Drillpipe Rotation Greater than 5 rpm SBP less than 1,500 psi	Influx Detected Drillpipe Rotation Less than 5 rpm SBP > 1,500 psi and < 2,500 psi	Influx Detected SBP greater than 2,500 psi
Pit Gain/ Influx Indicator	Influx less than 5 bbl	• Increase SBP, pump rate or a combination of both • Pick up off bottom • Maintain rotation • Circulate out influx • Adjust fluid density as required	• Increase SBP, pump rate or a combination of both • Pick up off bottom • Maintain rotation 5 rpm or less • Circulate out influx • Adjust fluid density as required	• Space out drillpipe • Shut down mud pumps • Shut-in on BOP • Inform Saudi Aramco foreman • Proceed with conventional well control through rig choke manifold
	Influx greater than 5 bbl	• Shut down mud pumps • Shut-in on MPD choke • Isolate MPD choke from the well • Maintain rotation • Space out drillpipe • Inform Saudi Aramco foreman • Proceed with conventional well control through rig choke manifold keeping pipe movement	• Shut down mud pumps • Shut-in on MPD choke • Isolate MPD choke from the well • Maintain rotation • Space out drillpipe • Inform Saudi Aramco foreman • Proceed with conventional well control through rig choke manifold keeping pipe movement	

Fig. 8 *The MPD pore pressure test at 6,714 ft.*

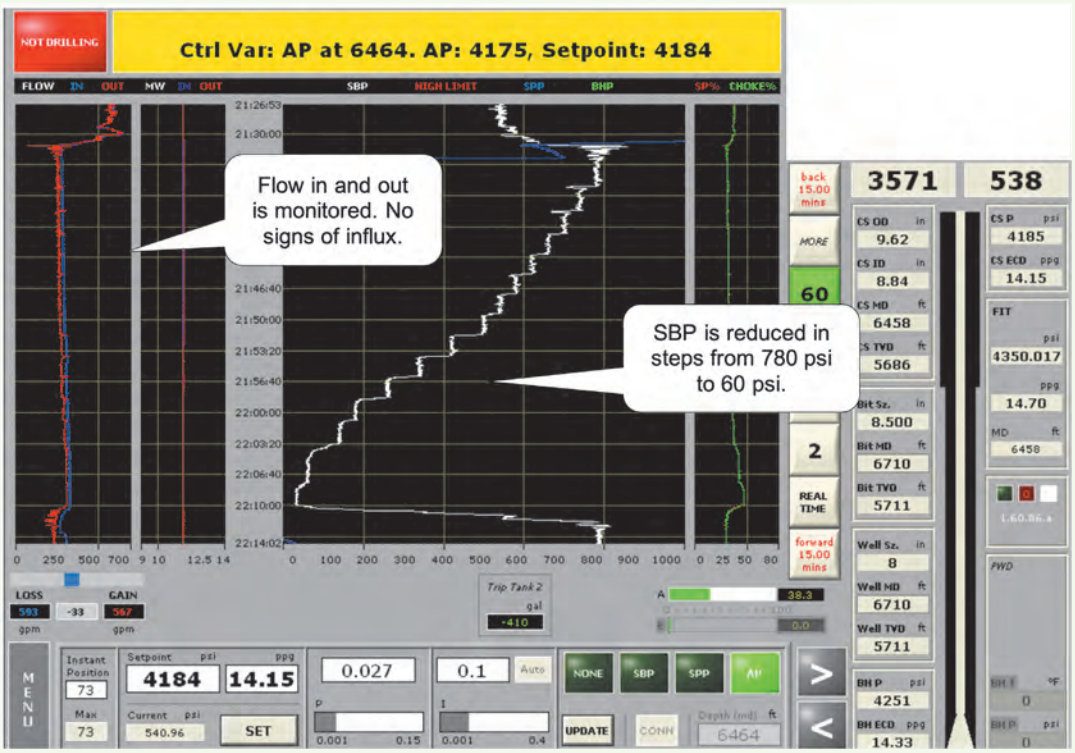

on the results of the LWD pressure measurement, it was decided to adjust the target ECD to 100 pcf, to maintain 200 psi of overbalance.

Drilling operations continued under these conditions until the 7" liner setting depth at 7,939 ft. Subsequent MPD pore pressure tests were done alongside the LWD pressure measurement; and used for quality assurance and quality control purposes.

Figure 9 shows the pressure trends "as drilled" for the entire 8½" section. It can be observed that with the use of MPD, the optimum overbalance was maintained, according to the pore pressure test results, and the results of the pressure points taken with the downhole tool.

The ECD was initially maintained at 106 pcf, considering that this was the original mud design. This was maintained until 214 ft inside the target formation, where a pore pressure test and a pressure point reading were performed. Based on these results, the SBP was adjusted to achieve an ECD of 100 pcf, and to maintain 200 psi of overbalance. These parameters were maintained until 6,855 ft, where another pore pressure test point reading was taken, obtaining a pore pressure value of 98 pcf. To comply with the required 200 psi of overbalance, the SBP was adjusted to achieve an ECD of 103 pcf.

The 7" liner point was reached at 7,939 ft with the target ECD of 103 pcf with no losses observed. To pull out of the hole, the well was displaced to 106 pcf of mud while the MPD system's SBP was gradually adjusted at the surface to maintain a constant BHP.

Running and Cementing of the 7" Liner

The 7" liner was run to above the 9⅝" casing shoe at a controlled speed, filling up and breaking circulation every 100 ft. At the 9⅝" casing shoe, the bell nipple was removed, and the MPD bearing assembly was installed. To minimize the probabilities of encountering losses due to surge pressures or high ECD, the well was displaced to 86 pcf of mud to run the 7" liner to the bottom in the MPD mode. This also minimized the chances of a stuck pipe due to high differential pressure.

The liner was run to the bottom as planned in the MPD mode, and no losses were registered during the operation. Figure 10 is a sequence of the liner operations. The returns of the well were always monitored through the Coriolis flow meter of the MPD manifold.

Once the liner was at the bottom and prior to setting the liner hanger, the well was displaced to 96 pcf of mud in preparation for the cement job. The 96 pcf of mud was required to ensure that the well was sufficiently balanced at the end of the cementing operations. The MPC technique was considered for the well due to the requirement to ensure long-term well integrity via zonal isolation. Preliminary hydraulic analysis revealed that the ECD that would be generated during cement displacement significantly exceeded the formation fracture gradient. As such, to assure efficient and fit-for-purpose zonal isolation for well integrity objectives, it was critical to avoid losses due

Fig. 9 *The ECD management for the 8½" section.*

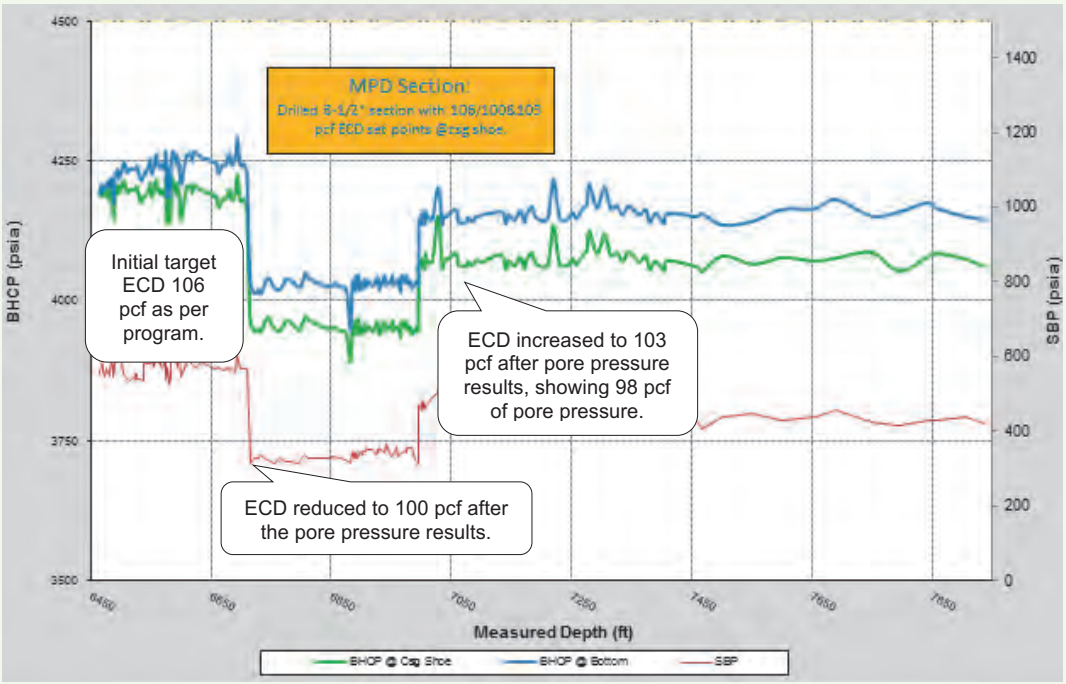

to a high ECD during the displacement of the 122 pcf of cement slurry.

During the cement job, there were several fluids of different densities being pumped. The 96 pcf MPD mud, the 116 pcf of spacer, and the 122 pcf of cement slurry. The displacement from 86 pcf of mud to 96 pcf of mud strived to reduce the consequences in case a pump failure occurred, by reducing the underbalance degree of the drilling fluid. Figure 11 depicts the various stages at which the different fluid densities were pumped.

The pumping schedule of the cement job was as follows:

- 20 bbl of 63 pcf of flush mud
- 100 bbl of 116 pcf of tuned spacer
- 81 bbl of 122 pcf of cement slurry
- First plug

Fig. 10 *The 7" liner operation — displacement and run to the bottom.*

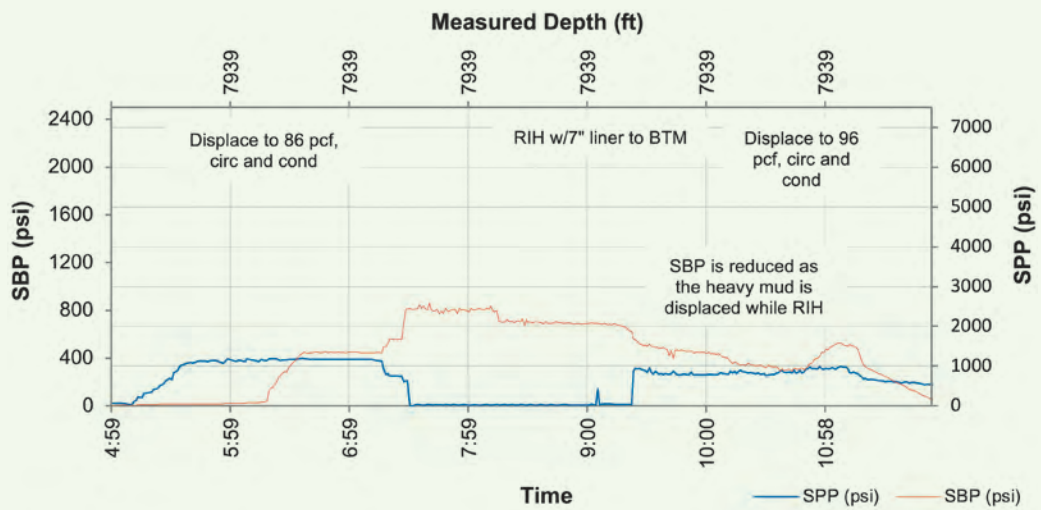

Fig. 11 *The MPC operation.*

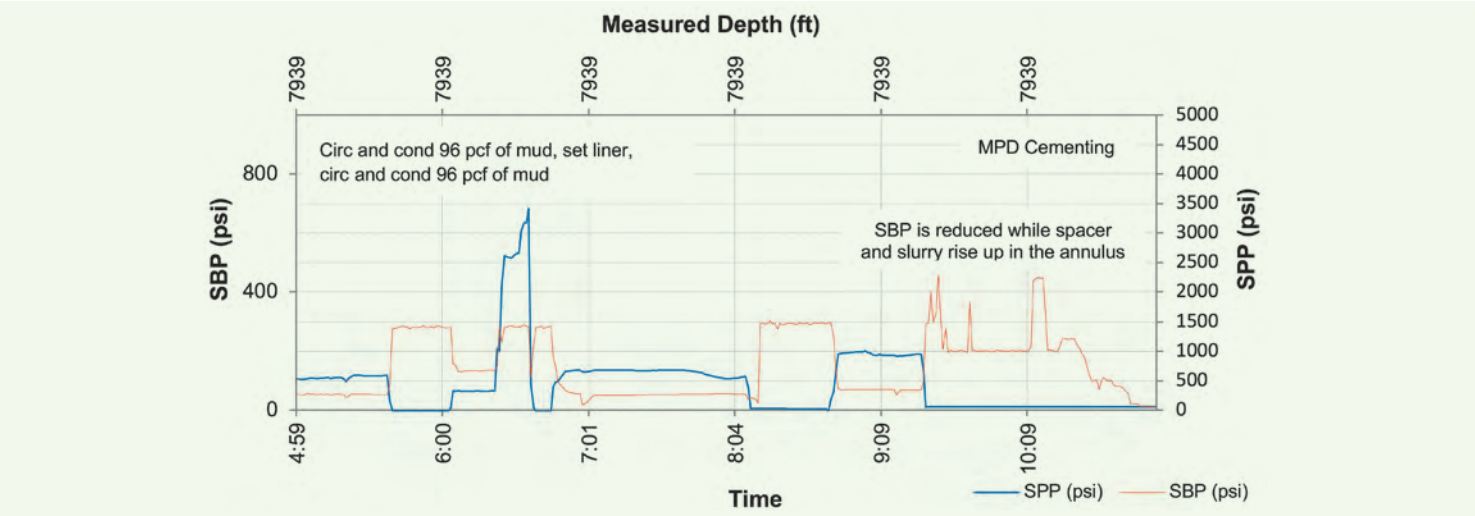

- 5 bbl of cement slurry
- 10 bbl of tuned spacer
- 34 bbl of 96 pcf of mud

The cement operation was executed without any operational or technical issues. To achieve the MPC objectives, a detailed pre-job meeting was held to clarify the operation objectives and define clear responsibilities/accountabilities. In addition, the following points were completed:

- Effective and clear communication lines between the cementing service provider, the MPD supervisor, and the drilling rig crew (drilling supervisor, drilling engineer, driller, and assistant driller).
- The cement and fluids displacement schedules were clearly defined and agreed. Based on these, the MPD crew estimated the SBP required to maintain the required ECD/ESD to always maintain well control.
- The MPD crew monitored the fluid's displacement (displacement rates, volumes, and weights) throughout the operation via real-time data transfer using WITSML (a wellsite information transfer standard markup language), and 2-way radio communication as an extra level of validation to ensure that the applied SBP did not induce a higher than required downhole pressure regime, which could lead to loss circulation, and jeopardize the zonal isolation objectives.

Drilling of the 6⅛" Hole Section

The MPD operations for the 6⅛" section started with 72 pcf of mud, and holding an equivalent MW of 98 pcf. After drilling 20 ft of the new hole section, an MPD pore pressure test was performed at 7,962 ft by reducing the BHP in gradual steps until the MPD choke was fully open. No indication of influx was observed, indicating that the pore pressure was below 72 pcf. The decision was to continue drilling with 72 pcf of mud and no backpressure on the MPD choke for another 120 ft, to take a pressure point reading with the downhole LWD tools.

- At 8,100 ft, the well was circulated clean and a pressure point measurement was performed, indicating a pore pressure of 64 pcf.
- To verify that the pore pressure regime was maintaining the same trend, a further 120 ft was drilled, and another pore pressure test was taken. As in the previous tests, the SBP was reduced in steps until the MPD choke was completely open, with no sign of influx. To confirm the pore pressure, another pore pressure measurement was performed with the downhole tools, finding the pore pressure to be 64 pcf.
- Considering the pore pressure results, to optimize the drilling conditions and minimize the chances of differential stuck pipe and losses, the well was displaced to 58 pcf of mud while holding a target ECD of 69 pcf. This was to maintain the required overbalance margin of 200 psi over the last known formation pressure of 64 pcf.

Drilling operations continued with these parameters, while performing periodic pore pressure measurements with the downhole tools to confirm the expected trend of the pore pressure was being reduced as the measured depth progressed. Table 2 lists the results of the pore pressure measurements. The well was drilled to a TD of 10,872 ft, and the well was circulated using periodic low viscosity and high-density pills during four full circulation cycles.

To pull out of the hole and minimize the chances of a differential stuck pipe, the open hole volume was displaced from 58 pcf of mud to 69 pcf of mud. Despite these precautions, a stuck pipe incident was encountered while pulling out of the hole during a connection

Table 2 *Pore pressure measurements.*

Depth (ft)	Pore Pressure (pcf)
8,760	48.5
9,395	39
9,996	39
10,072	38

Table 3 *The sequence of the acid treatment.*

Sequence	Process
1	50 bbl of 75 pcf of spacer
2	40 bbl of 20% VDA acid
3	50 bbl of 75 pcf of spacer

at 10,680 ft. The well was displaced back to 59 pcf of mud and the ECD decreased gradually to reduce the differential pressure, however, the pipe was not freed. While circulating with the MPD choke fully open and at 100 GPM, a sequence of acid treatment was pumped, Table 3.

While soaking the acid, the pipe was slacked in compression, and became free within four minutes. The trip to the liner shoe continued with 59 pcf mud in the open hole and the MPD choke fully open. Once at the liner shoe, the cased hole was displaced to 72 pcf mud with the MPD choke fully open, and it was circulated until the MW in equaled the MW out.

Before removing the RCD bearing assembly, the well was observed for four hours to confirm that no influx had been taken while circulating or pulling out with no backpressure. After confirming that the well was static, the bearing assembly was removed, and the bell nipple was installed, finalizing the MPD operations.

Conclusions

This case study highlights the successful application of the MPD technique to manage a heterogeneous pressure profile in the same target formation of interest. The objectives of the well were met, and ensured well delivery with minimal lost time due to a differential stuck pipe compared to similar wells drilled in the same part of the field — 17 hours vs. 78 hours.

Additionally, and equally a critical requirement for the well, zonal isolation integrity was achieved through the application of MPC to avoid induced losses, due to high ECD during cement displacement operations. If induced loses had occurred, the quality and placement of the cement around the 7" liner would have been severely compromised. Consequently, the high-pressure zones of the well would not be sufficiently isolated, thereby impacting the long-term well integrity, and leading to an increased risk of potential sustained casing pressure at later stages of the well life.

By utilizing the MPD techniques, the significant costs of some drilling fluids were avoided (67% less cost), and the reservoir section was drilled with less damaging (low barite content) fluids, compared to similar wells with the same objectives.

References

1. Spriggs, P.N. and Frink, P.J.: "MPD Planning: How Much Is Enough?" SPE paper 113682, presented at the SPE/IADC Managed Pressure Drilling and Underbalanced Operations Conference and Exhibition, Abu Dhabi, UAE, January 28-29, 2008.

2. Alrasheed, A., Oqaili, A.H., Aljubran, M.J. and Ezi, P.C.: "Deployment of Fully Automated MPD and Manganese Tetroxide Mud System to Drill Ultra-Narrow Mud Window in HPHT Gas Wells," SPE paper 190000, presented at the SPE/IADC Managed Pressure Drilling and Underbalanced Operations Conference and Exhibition, New Orleans, Louisiana, April 17-18, 2018.

3. Medley, G.H., Moore, D.D. and Nauduri, A.S.S.: "Simplifying MPD — Lessons Learned," SPE paper 113689, presented at the SPE/IADC Managed Pressure Drilling and Underbalanced Operations Conference and Exhibition, Abu Dhabi, UAE, January 28-29, 2008.

About the Authors

Peter I. Egbe

M.S. in Drilling and Well Engineering, Robert Gordon University

Peter I. Egbe currently works as a Senior Drilling Engineer in Saudi Aramco's Exploration and Oil Drilling Engineering Department. He joined Saudi Aramco in 2014, and has over 20 years of experience working with BP International, TAQA Bratani (a subsidiary of Abu Dhabi National Oil Company), Energy Division (an arm of the U.K. Government's Health & Safety Executive responsible for regulating offshore oil and gas operations in U.K. waters), Total S.A., and Schlumberger.

Peter's interests are in drilling optimization through the application of new technologies, well and completions design optimization, and well integrity assurance throughout the well's life cycle from the design phase to well abandonment.

He holds professional certifications as a Chartered Engineer, and Chartered Petroleum Engineer from the Engineering Council U.K., and the Energy Institute U.K., respectively.

Peter received his B.S. degree in Chemical Engineering, and his M.S. degree in Drilling and Well Engineering, from the Robert Gordon University in Aberdeen, Scotland, U.K. He is currently pursuing a Ph.D. degree in Drilling & Well Engineering (degree in view autumn 2020) from his alma mater.

Carlos Iturrios

B.S. in Quality Engineering,

Universidad Juárez Autónoma de Tabasco

Carlos Iturrios has more than 12 years of progressive oil and gas experience in managed pressure drilling (MPD) operations. He is currently the MPD Technical Manager for Weatherford in Saudi Arabia and Bahrain, managing a team of 23 field engineers for MPD operations, as well as providing technical support for the client and business development activities.

Previously, Carlos held the position of the MPD Focal Point for Weatherford operations in the Gas Department of Saudi Aramco, as well as a MPD Field Engineer in Saudi Arabia, Iraq, and Mexico. He also worked to support other projects in Latin America with Weatherford and Schlumberger.

Carlos received his B.S. degree in Quality Engineering from the Universidad Juárez Autónoma de Tabasco, Villahermosa, Mexico.

Dependence of Key Estimates from PTA on Flow Paths in Heterogeneous Reservoir Systems

Dr. N.M. Anisur Rahman and Sukru Sarac

Abstract / Although parameter estimates from pressure transient analysis (PTA) in homogeneous reservoir systems are well understood, such estimates from heterogeneous systems can be illusive if the flow paths of fluid movement in the reservoir are not well captured. This study brings in the perspectives of parameter estimations, e.g., flow capacity, skin factor, and volume of the investigated region, based on the fluid flow paths. The disseminated knowledge will help mitigate potential errors due to misunderstanding flow paths.

A number of idealized multilayer models, and geological sector models, have been built to generate pressure responses, and to understand the flow paths toward wells. Flow paths are controlled through horizontal and vertical permeability, and skin factors in perforated and open intervals in the wells. In each case, the flow capacity, skin factor, and volume investigated are estimated from the generated pressure responses to show the dependence of estimated parameters on the flow paths in the reservoirs. We will also determine the shape and size of the region investigated with changes in flow paths during the numerical experiments.

In this article, we highlight the pitfalls of interpreting pressure transient data for layered, heterogeneous reservoir systems. The fluid flow paths in complex reservoirs have direct impacts on the transient pressure behavior, and on the estimates of key reservoir parameters. Natural paths that fluids flow along deep inside the reservoir can be modified in the reservoir models based on the engineer's input parameters. This can inadvertently result in modifications of the flow capacity, investigated volume, and reserves estimate.

The outcomes of these numerical experiments with analytical and numerical models will certainly challenge the existing understanding of the reservoir flow capacity, and the widely accepted radius of investigation concept. Conventionally, these parameters are explained without any regard for the flow paths in reservoirs. This article shows that the flow paths indeed have a direct impact on the transient pressure behaviors in heterogeneous reservoir systems.

This study establishes a relationship between the parameter estimates and the flow paths in heterogeneous systems. Moreover, running into the pitfalls while building transient and simulation models for heterogeneous reservoir systems will be mitigated with the knowledge gained here.

Introduction

Although parameter estimates from pressure transient analysis (PTA) in homogeneous reservoir systems are well understood, such estimates from heterogeneous systems can be illusive if the flow paths of the fluid movement in the reservoir are not properly captured. This study brings in the perspective of parameter estimations, e.g., flow capacity, skin factor, and volume of the investigated region, based on the fluid flow paths. The disseminated knowledge will help mitigate potential errors due to misunderstanding flow paths. This will also improve reservoir characterization and reserve calculations. Salazar and Villa (2007)[1] discussed the complexity of extracting the effective permeability in heterogeneous reservoir systems.

A number of idealized multilayer models, and geological sector models, have been built to generate pressure responses, and to understand the flow paths toward wells. Flow paths are controlled through horizontal and vertical permeability, and skin factors in perforated and open intervals in the wells. In each case, the flow capacity, skin factor, and volume investigated are estimated from the generated pressure responses to show the dependence of the estimated parameters on the flow paths in the reservoirs.

We will also determine the shape and size of the region investigated with changes in flow paths during the numerical experiments. These experiments with numerical models involve estimations of the distances from the producing well at which a minimum prescribed pressure drawdown exists. Kuchuk (2009)[2] demonstrated that the radius of investigation very much depends on the applied criterion. The region of investigation or influence in the reservoir model will be identified by applying a criterion of pressure drawdown at the farthest possible distance from the producing well. Anisur Rahman et al. (2015)[3] observed that the profiles of the

pressure derivative in the tested reservoir layer can be influenced by the magnitude of the transient cross-flow rate from an adjacent reservoir layer.

In this article, we will highlight the pitfalls of interpreting pressure transient data for layered, heterogeneous reservoir systems. The fluid flow paths in complex reservoirs have direct impacts on the transient pressure behavior, and on the estimates of key reservoir parameters. Natural paths that fluids flow along — deep inside the reservoir — can be modified in the reservoir models based on the engineer's input parameters. This can inadvertently result in modifications of the flow capacity, investigated volume, and reserves estimate. Larsen (1982)[4] demonstrated that the effective skin factor is dependent on the individual skin factor and fractional flow rate of the individual layer of a two-layered reservoir system.

The outcomes of the numerical experiments with analytical and numerical models of this study will certainly challenge the existing understanding of the reservoir flow capacity, and the widely accepted radius of investigation. Conventionally, these parameters are explained without any regard for the flow paths in the reservoirs. We show that the flow paths indeed have a direct impact on the transient pressure behaviors, and on the key parameters, i.e., flow capacity, skin factor, and volume of influence or investigation in the heterogeneous reservoir systems. In addition, the areal growth of such a region of influence is spatially nonuniform due to reservoir heterogeneity. As such, assigning a single value to the radius of investigation can be misleading.

The objective of this study is to establish a relationship between the parameter estimates and the flow paths in heterogeneous reservoir systems. Keeping the possibility of changing flow paths in mind will help mitigate running into the pitfalls while building transient and simulation models for heterogeneous reservoir systems.

Investigation of Layered Reservoir Models

We investigated a number of cases involving multilayer reservoir models to understand the effects of fluid flow paths. Traditionally, for numerical well test interpretation, it is a common practice to match the flow capacity and the reservoir heterogeneity responses by using the derivative match, and then to match the skin factor. These cases are to show that the parameter estimates can change due to a change in flow paths. Subsequently, flow paths would be changed by changing the skin factors at the wellbore.

When skin factors at the wellbore change, the network for fluid flow encounters a new field of resistance in a heterogeneous reservoir system. Under the new field of resistance, reservoir fluids find their new paths while looking for the ones offering the least resistance. Such new paths can potentially result in a new magnitude of the flow capacity. A number of idealized multilayer models and geological sector models have been built to generate pressure responses at the corresponding wellbores. Each model is run for a given production rate through the active well in the model with a numerical package. The pressure derivative values are calculated with the designated production rate and the calculated drawdown pressures from the model.

Grids in all numerical models have been refined around the wellbore to capture fine early time responses for computing the pressure derivatives. While running a simulation model with a negative skin factor, grids connecting the wellbore can sometimes be deactivated if the probe radius[5] exceeds the equivalent radius of the grid block intersected by the wellbore. All the models presented here have been examined to make sure that these models are free of such numerical artifacts, which could unintentionally affect the flow contributions from the reservoir.

Only single-rate drawdown cases have been simulated in this study to be able to capture the shape and the distance of the differential pressure front with time.

Two-Layer Systems

Two idealized, two-layer models are studied to see the effects of skin factors in the individual reservoir layers of Well-A. The top layers of the systems have a permeability of 100 millidarcies (md), and the bottom layers have a permeability of 10 md. Each layer has a pay thickness of 40 ft. In one model, the reservoir layers are considered commingled, and in the other model, the reservoir layers are subject to crossflow through their contact area within the reservoir. A vertical well completely penetrates both reservoir layers. Both reservoir layers are limited in extent, which would be reflected as a unit slope line in the late times of the respective log-log plots.

Figure 1 presents the log-log plot of the drawdown pressure responses due to a constant rate of oil production for different combinations of skin factors in the layers. Here, these layers are commingled without any crossflow among themselves in the reservoir, rather these layers are hydraulically connected through the wellbore only in Well-A. These systems are similar to the commingled systems presented by Lefkovits et al. (1961)[6]. Substantial separation of derivative profiles is observed in the early times for different combinations of skin factors in the reservoir layers. In the middle times of infinite acting radial flow regimes, the pressure derivative profiles of the case of the skin factor (s) $s_1 = 0$, $s_2 = 10$ and of the case of $s_1 = 0$, $s_2 = 0$ show a steady separation leading to a difference in the flow capacity as $\Delta kh = 323$ md-ft. This illustrates the fact that a skin factor of $s_2 = 10$ in the bottom layer can effectively cause a reduction in flow capacity by 7.7%, compared to the undamaged reservoir layers.

Lefkovits et al. (1961)[6] observed that the relative contributions of individual layers to the well production in a commingled system can be affected by the layer's skin factors. Conventional understanding of PTA does not condone the differences in the flow capacity previously observed in Fig. 1, because of disregarding the changed flow paths and flow rate contributions of

Fig. 1 *The effects of skin factors on the log-log plots in a two-layer, commingled reservoir system around Well-A.*

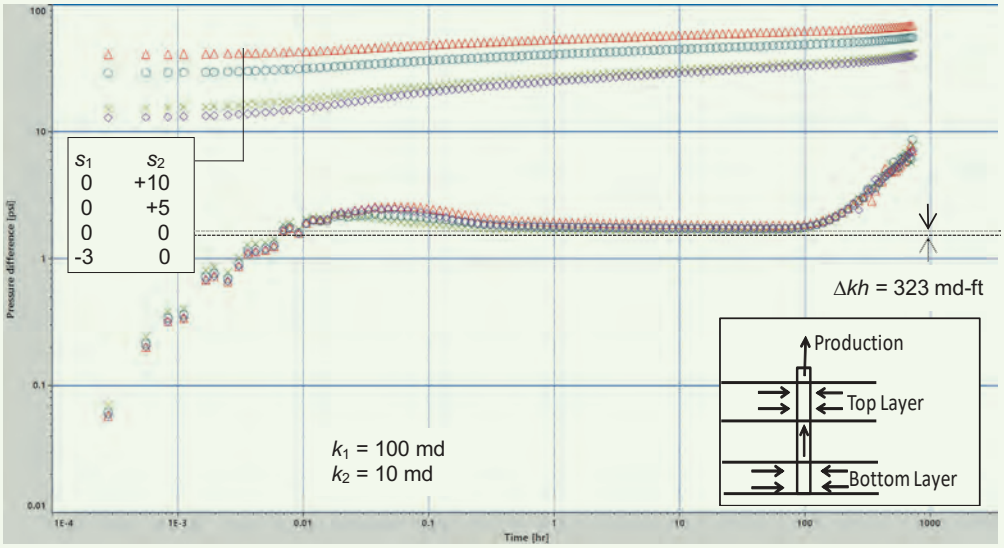

reservoir fluids in the individual layers.

The model results for the reservoir layers that are subject to crossflow within the reservoir are presented in Fig. 2 for different combinations of skin factors in the reservoir layers. Unlike the commingled conditions of the layers presented earlier, there is no separation of pressure derivative profiles in the middle times. Therefore, no preferential paths of fluid flow are observed due to different combinations of designated skin factors in the individual layers.

Heterogeneous Reservoir Systems

Here we use geological sector models to account for reservoir heterogeneity, and generate pressure responses due to a constant rate of production.

Oil Producer. This model captures the heterogeneity with 47,000 cells in 47 layers of an oil reservoir. In this case, a horizontal well, Well-B, produces dry oil at a constant rate. Figure 3 shows the pressure responses during the pressure drawdown generated for different skin factors for a heterogeneous oil reservoir. This example shows that a negative skin factor of -2.2 has caused the flow capacity (kh) to increase by 55% over its magnitude of 6,316 md-ft at $s = 0$ calculated at the late times. Note that a positive skin factor of +1.1 has

Fig. 2 *The effects of skin factors on the log-log plots in a two-layer reservoir system with crossflow around Well-A.*

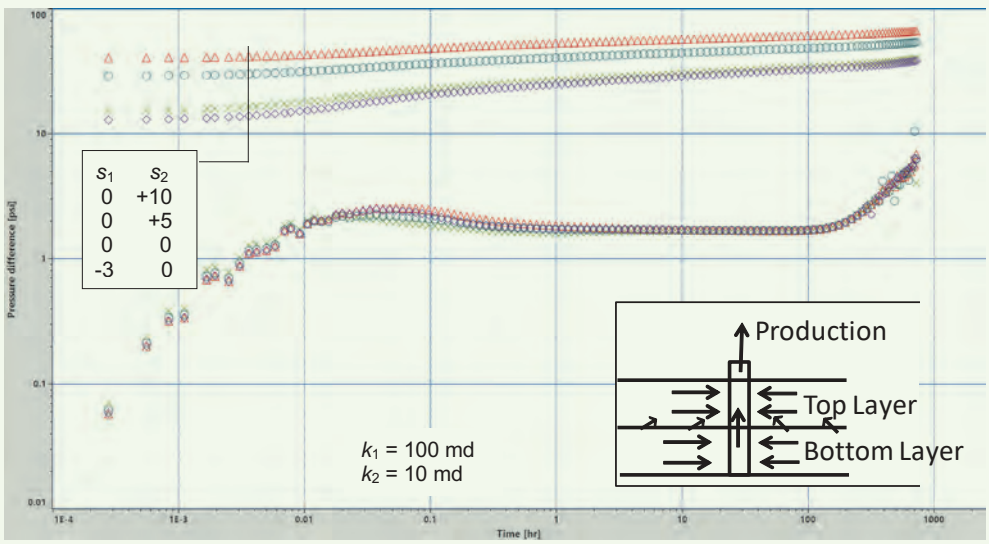

Fig. 3 *The effects of skin factors on the log-log plots for a heterogeneous oil reservoir around Well-B.*

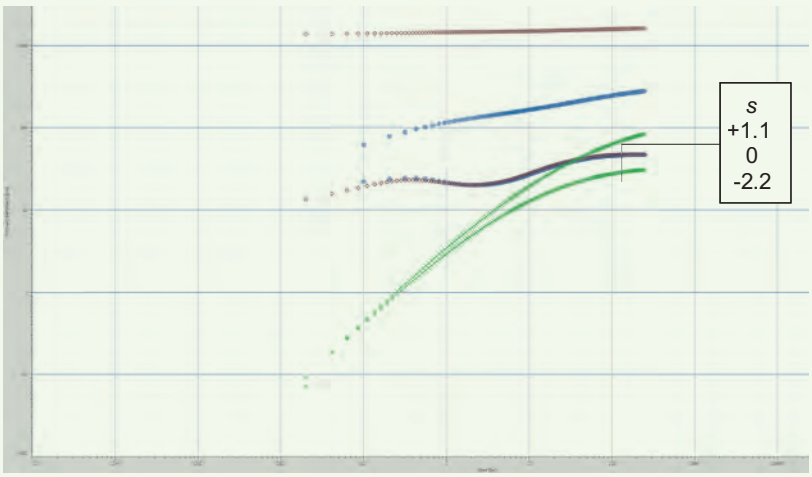

Fig. 4 *The effects of skin factors on the log-log plots in a heterogeneous gas reservoir around Well-C.*

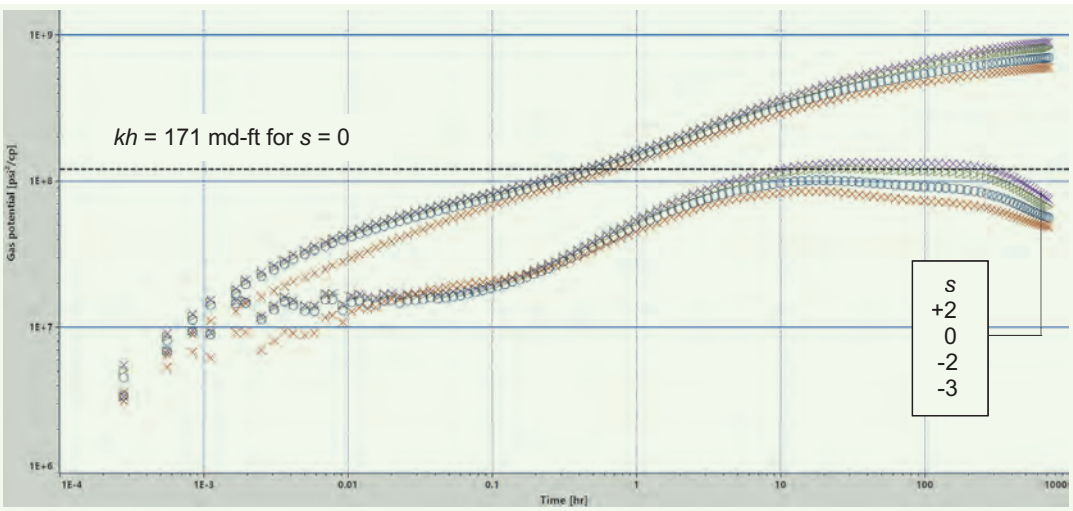

not made the *kh* value change, compared to that at *s* = 0. The studied model has been large enough not to see the effects of the model boundaries as evident in the profiles of the pressure derivative.

Gas Producer. This model captures the heterogeneity of a gas reservoir. In this case, a vertical well, Well-C, produces gas at a constant rate. This cased hole has been completed with six sets of perforations. Pressure responses during the production period generated for different skin factors — one value applied to all perforations at a time — are presented on the log-log plot in Fig. 4. Here, the derivative profiles do not overlay from the middle time to the late time region. For *s* = 0, *kh* = 171 md-ft as calculated from the middle time region of the corresponding log-log plot.

Table 1 shows how the *kh* values change with different values of skin factors. This shows that a skin factor of +2 causes a loss of 8.8% flow capacity, while skin factors of -2 and -3 cause gains in flow capacity of

Table 1 *The effects of variations of skin factor on the apparent flow capacity at Well-C.*

s	*kh* (md-ft)	Percentage Difference with *kh* at *s* = 0
0	171	0
+2	156	-8.8
-2	206	+20.5
-3	244	+42.7

20.5% and 42.7%, respectively.

Effects of Volume Investigated. Now, we are going to look into the volumes investigated around Well-C in the gas reservoir for different values of the skin factor. Kuchuk (2009)[2] demonstrated that the radius of investigation depends on the flow rate, and has expanded this idea by proposing different criteria for estimating the radius of investigation. One of these criteria is based on the gauge resolution in consideration of the natural background noise. In this study, we will utilize such a criterion in determining the volume of investigation in different cases. As shown earlier, the magnitudes of flow capacity have been impacted by the individual skin factors at the wellbore due to changed flow paths in the heterogeneous reservoir. Due to the changed flow paths, it is reasonable to assume that the sizes of the regions of investigation or influence around the wellbore will be different for the same duration of flow.

We will examine different cases of Well-C to understand how the flow paths are influenced due to changed magnitudes of the skin factor, in addition to permeability distributions in both the horizontal and vertical directions. Isosurfaces have been generated, Fig. 5, for different cutoff values in drawdown, δp, with $s = 0$ and a constant rate of production in Well-C. On an isosurface, there exists a front at a given point in the reservoir with a differential drawdown pressure as prescribed by the cutoff value. By definition, the differential pressure drawdown outside an isosurface for δp is less than δp, and the differential pressure drawdown inside the isosurface is greater than δp for a constant rate of production.

As expected, Fig. 5 shows that an isosurface encloses a larger volume for a lower value of δp. Volumes enclosed by isosurfaces depend on the production time, flow rate across each grid block and the cutoff parameter of a drawdown. A cutoff parameter of $\delta p = 0.01$ psia for spatial drawdown appears to be reasonable based on the resolution in commercial gauges normally deployed in the field.

In this study, we will follow the concept of Kuchuk (2009)[2] to estimate the volumes of the regions of influence by generating isosurfaces in the reservoir model around Well-C for a cutoff parameter of $\delta p = 0.01$ psia. Therefore, this cutoff parameter is used to estimate the volume of influence around Well-C, which includes all the reservoir regions with drawdown pressures of 0.01 psia or higher around Well-C. Alternatively speaking, there exists pressure differences of 0.01 psia or higher within the region of influence in production at a constant rate for 31 hours. The region of influence at a given time is defined as the reservoir region, which shows signs of pressure gradients within, and contributes to the production through the wellbore. Such a region of influence can grow spatially with time in the absence of any apparent boundaries in the reservoir while the well is still in production. The areal growth of such a region of influence around the wellbore can be spatially nonuniform along any direction, due to reservoir heterogeneity in both areal and vertical directions.

Regions of influence are being looked into for the cases of $s = +2$ and $s = -3$. The isosurface enclosing the region of influence is presented in Fig. 6 at the end of 31 hours of production for $s = +2$. Figure 7 illustrates the region of influence using the simulation grid view for calculating the volume for the same case. These graphical representations show that the areal growth of the region of influence is spatially nonuniform due to reservoir heterogeneity in both areal and vertical directions. Conventionally, one tends to estimate the radius of investigation even in heterogeneous reservoir

Fig. 5 *The cross-sectional view of the isosurfaces for different values of δp enclosing respective regions of influence for s = 0 after 10 hours around Well-C.*

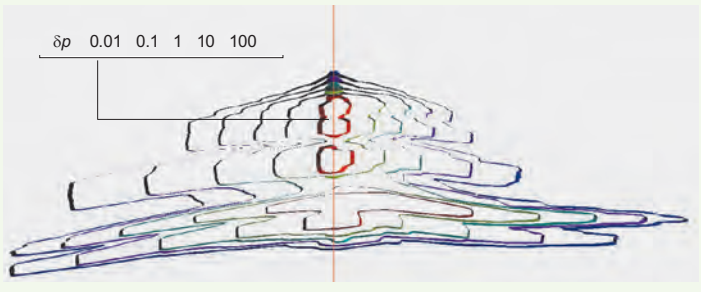

Fig. 6 *A 3D illustration of the isosurface enclosing the region of influence for s = +2 after 31 hours around Well-C.*

Fig. 7 *A 3D view of the grid blocks in the region of influence for s = +2 after 31 hours around Well-C.*

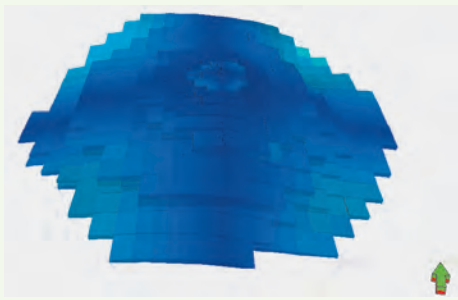

systems. In such cases, assigning a single value to the radius of investigation can be misleading.

Similar to the earlier case, the isosurface enclosing the region of influence is presented in Fig. 8 at the end of 31 hours of production for s = -3. Figure 9 illustrates the region of influence using the simulation grid view for calculating the volume for the same case. As in the earlier case, the areal growth of the region of influence in this case is also spatially nonuniform due to reservoir heterogeneity in both the areal and vertical directions. As done conventionally, assigning a single value to the radius of investigation for a heterogeneous reservoir system can be misleading.

Table 2 presents and compares the volumes of influence for the two cases presented. It shows that there is more volume of influence in the case of s = -3 than that in the case of s = +2 by 20.5%. Note that we have used the same reservoir model for all these cases. Any change in the volume of influence impacts the corresponding magnitude of flow capacity as previously seen in Table 1.

Figure 10 presents production log profiles generated synthetically from the simulation model of Well-C for the cases of s = +2 and s = -3. The case for s = 0 is very similar to the one for s = +2. It is apparent that the relative flow contributions of the tighter sections increase in the case of s = -3, compared to the corresponding ones in the case of s = +2. These changes in the relative flow contributions have affected the distribution of the pressure fronts in different layers in the reservoir, impacting the pressure responses measured at the wellbore. With the altered volume of investigation, the total effective flow capacity of the system achieved by this simulated flow test increases to 244 md-ft as evident in Table 1.

Fig. 8 *A 3D illustration of the isosurface enclosing the region of influence for s = -3 after 31 hours around Well-C.*

Fig. 9 *A 3D view of the grid blocks in the region of influence for s = -3 after 31 hours around Well-C.*

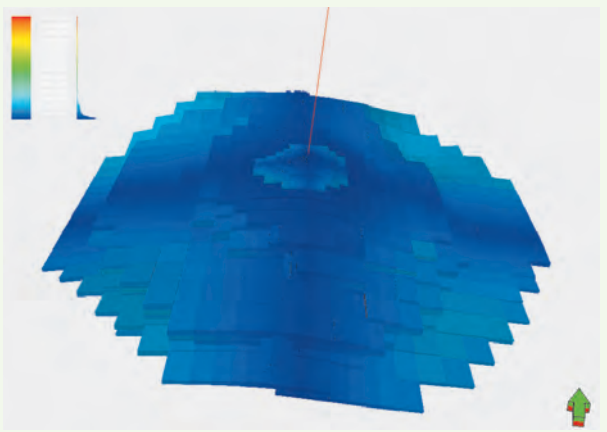

Table 2 *The effects of variations of skin factor on the volume of influence at Well-C.*

s	Volume of Influence (MMbbl)	Percentage Difference with Case of *s* = 0
+2	438.5	-5.3
0	463.2	0
-3	528.5	+14.1

Notice that there is a spike in the fluid contributions across the second to last set of perforations completed across the very high permeability of Well-C, Fig. 10. This spike is more prominent in a particularly high permeability layer for s = +2. We have moderated the permeability of this particular layer, and have run the modified model to understand the effects of the new permeability distribution.

Figure 11 shows the production log profiles generated synthetically from the simulation model of Well-C for the cases of s = +2 and s = -3 with a moderated permeability distribution in the reservoir layers around the second to last perforations. In this case, the spike of the high magnitude of contribution has disappeared, culminating in creating a more uniform fluid contribution in the second to last set of perforations around Well-C for both skin factor values. The high permeability layer in the second set of perforations contributes less for s = -3 to compensate for the contributions from the low permeability layers.

Figure 12 displays comparative log-log plots of pressure responses for different skin factors in the modified reservoir model around Well-C. This shows that the flow capacity at s = 0 has slightly increased to 179 md-ft from the pre-modification level of 171 md-ft.

Table 3 registers the variations of the kh values upon modification of the model. These values are comparable to the respective values prior to the model modification as previously presented in Table 1.

Discussion

To understand what has transpired in the earlier examples of layered, heterogeneous systems, we have built composite reservoir systems over two layers. These

Fig. 10 *The production log profiles around Well-C for s = +2 and s = -3 after 30 days of production.*

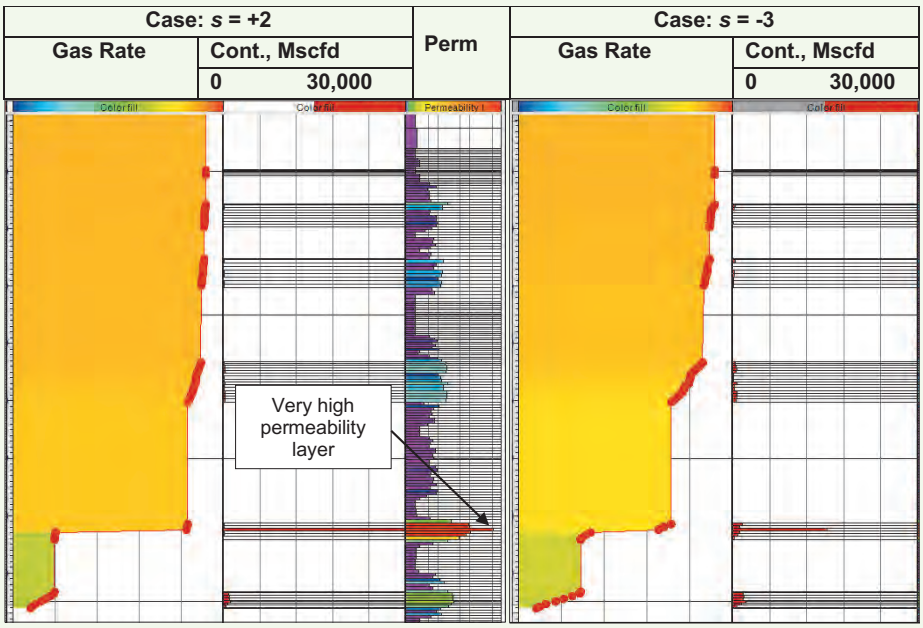

Fig. 11 *The production log profiles around Well-C with modified models for s = +2 and s = -3 after 30 days of production.*

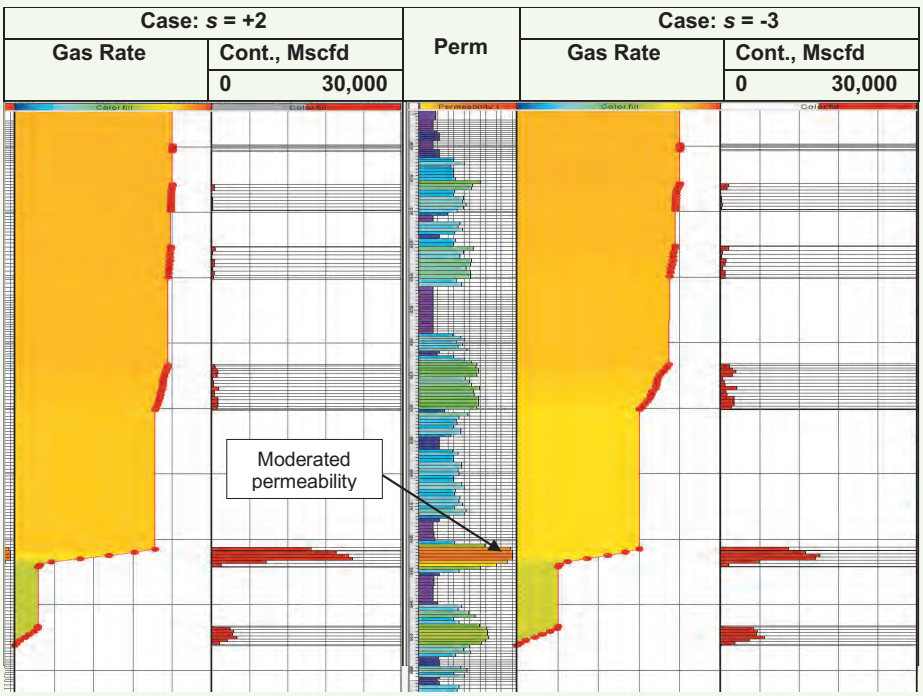

systems, much simpler than the heterogeneous systems considered earlier, can be characterized as heterogeneous in areal and vertical directions with a known description. A vertical well, Well-D, is completed fully over both commingled layers, which are contributing to oil production. The composite zones in each layer — 40 ft thick — have a sharp interface at a distance of 300 ft from the well. The reservoir layers are separated by an impermeable barrier that is 20 ft thick. Here we examine two combinations of permeability

Fig. 12 *The effects of the skin factors on the log-log plots with modified models around Well-C.*

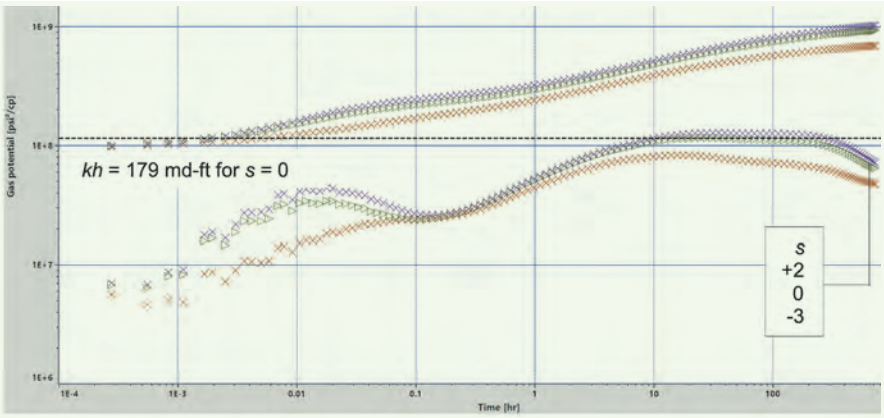

Table 3 *The effects of variations of the skin factor on the apparent flow capacity in modified models around Well-C.*

s	*kh* (md-ft)	Percentage Difference with *kh* at *s* = 0
0	179	0
+2	164	-8.5
-3	251	+40.0

in each layer around Well-D:

- Combination-1: 10 md and 100 md.
- Combination-2: 10 md and 1,000 md.

Combination-1 can be described as: The inner zone around the well in the top layer has a permeability of 10 md, and the outer zone has a permeability of 100 md. In the bottom layer, the inner zone around the well has a permeability of 100 md, and the outer zone has a permeability of 10 md.

Similarly, Combination-2 can be described as: In the top layer, the inner zone around the well has a permeability of 10 md, and the outer zone has a permeability of 1,000 md, while in the bottom layer, the inner zone around the well has a permeability of 1,000 md, and the outer zone has the permeability of 10 md.

Prasad et al. (1996)[7] observed that the effective permeability depends on both the frequency and the spatial distribution of the fine-scale permeability values. We have also observed such a phenomenon in this study.

As the numerical models are built with the properties of Combination-1 and Combination-2, we have validated the numerical models by comparing them with the corresponding analytical models. Figure 13 shows the comparison of pressure responses generated with each of the combinations for $s_1 = +5$, $s_2 = +5$. This shows that the numerical models are consistent with the corresponding analytical models.

Fig. 13 *A comparison of the log-log plots from cases with Combination-1 and Combination-2.*

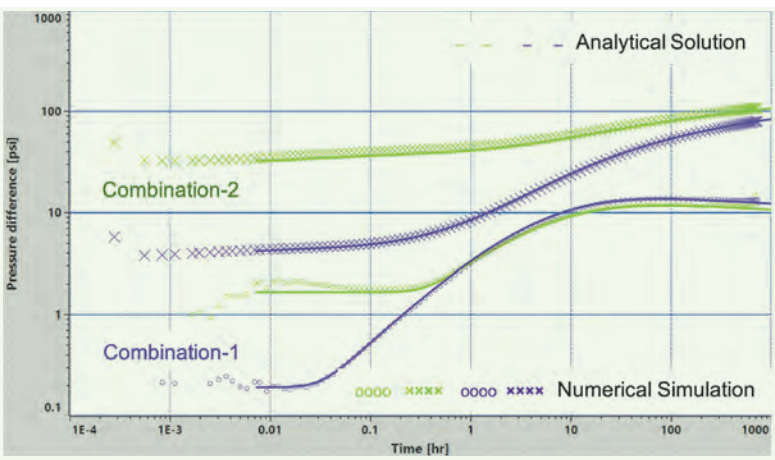

Fig. 14 *The production log profiles of Combination-1 in Well-D.*

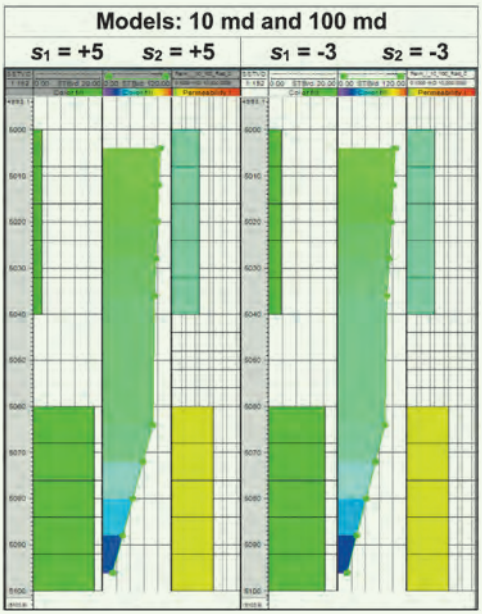

Fig. 15 *A comparison of the log-log plots for Combination-1.*

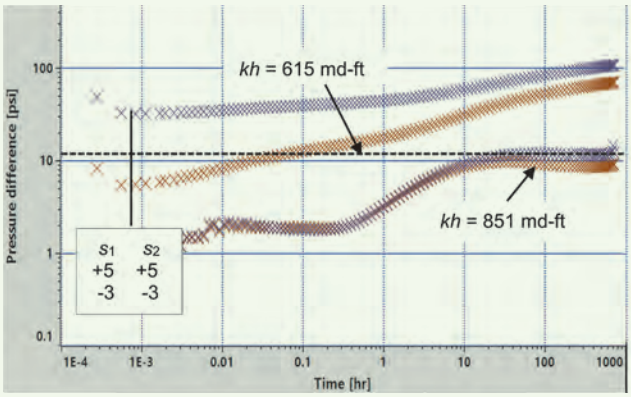

Output of the models with Combination-1 for s_1 = +5, s_2 = +5, and for s_1 = -3, s_2 = -3 are presented in Figs. 14 and 15. The production log profiles in Fig. 14 show that the negative skin factors cause the bottom layer to flow less, allowing the top layer to flow more at 12 hours into production. In this combination, the top layer has a lower permeability in the inner zone around the wellbore, and the bottom layer has a higher permeability in the inner zone around the wellbore. The log-log plots in Fig. 15 show that the negative skin factors have driven the flow capacity to be 38.4% higher, compared to the flow capacity observed in the corresponding positive skin case.

The isosurfaces in Fig. 16 clearly show that the isosurfaces in the top layer with spatial drawdown, δp = 0.01, 0.1 psia and 1.0 psia for s_1 = -3, s_2 = -3, have traveled farther than the corresponding ones for s_1 = +5, s_2 = +5 after 12 hours of production from Well-D. As before, we define the region of influence being the region enclosed by the isosurface for the spatial drawdown, δp of 0.01. This means that the region of influence around Well-D for s_1 = -3, s_2 = -3 caused by the production is more extensive than that for s_1 = +5, s_2 = +5. It remains evident that the areal growth of the region of influence is different in each layer at a given time. It is fair to say that the additional reservoir region for s_1 = -3, s_2 = -3 contributes to capturing the additional flow capacity.

Combination-2 is to provide a higher contrast in permeability variations in an areal direction of each

Fig. 16 *A comparison of cross-sections of isosurfaces at 12 hours into production for Combination-1 at Well-D. Upper plot:* s_1 = +5, s_2 = +5; *Lower plot:* s_1 = -3, s_2 = -3.

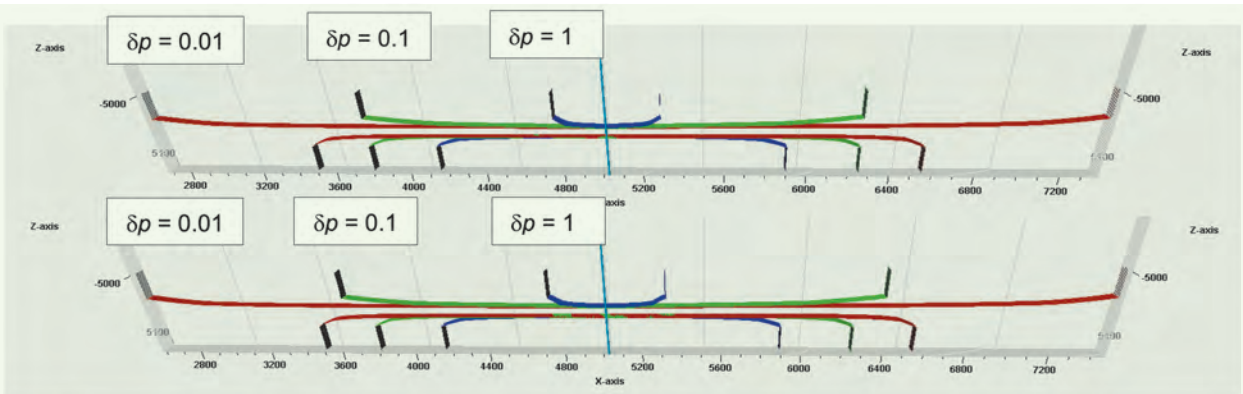

Fig. 17 *The production log profiles of Combination-2 in Well-D.*

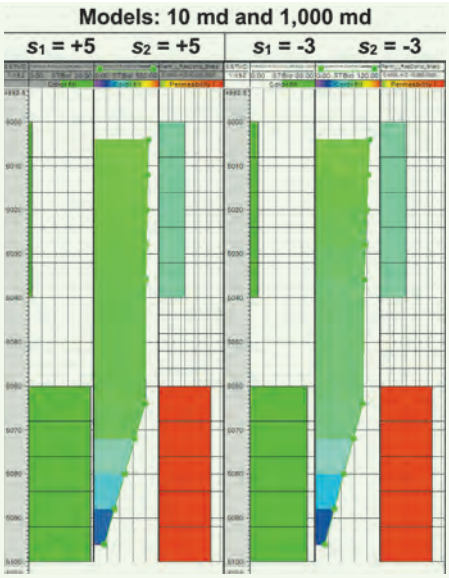

Fig. 18 *A comparison of the log-log plots.*

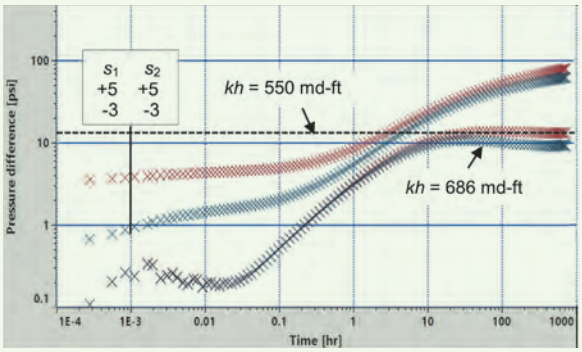

layer than what Combination-1 does. Output of the models with Combination-2 for s_1 = +5, s_2 = +5, and for s_1 = -3, s_2 = -3 are presented in Figs. 17 and 18. The production log profiles in Fig. 17 show that the negative skin factors cause the bottom layer to flow less, allowing the top layer to flow more at 12 hours into production. In this combination, the top layer has a lower permeability in the inner zone around the wellbore, and the bottom layer has a higher permeability in the inner zone around the wellbore. The log-log plots in Fig. 18 show that the negative skin factors have driven the flow capacity to be 24.7% higher, compared to the flow capacity observed in the corresponding positive skin case.

The isosurfaces in Fig. 19 clearly show that the isosurfaces in the top layer with spatial drawdown, δp = 0.01, 0.1 psia and 1.0 psia for s_1 = -3, s_2 = -3 have traveled farther than the corresponding ones for s_1 = +5, s_2 = +5 after 12 hours of production from Well-D. As before, we define the region of influence being the region enclosed by the isosurface for the spatial drawdown, δp of 0.01 psia. This means that the region of influence around Well-D for s_1 = -3, s_2 = -3 caused by the production as it is more extensive than that for s_1 = +5, s_2 = +5. The areal growth of the region of influence in each layer remains nonuniform at a given time. It is fair to say that the additional reservoir region for s_1 = -3, s_2 = -3 contributes to accounting for the additional flow capacity.

There is a clear trend in the examples of this study — whenever fluid flow paths change their directions to include more reservoir regions, the corresponding

Fig. 19 *A comparison of the cross-sections of the isosurfaces at 12 hours into production for Combination-2 at Well-D. Upper plot: s_1 = +5, s_2 = +5; Lower plot: s_1 = -3, s_2 = -3.*

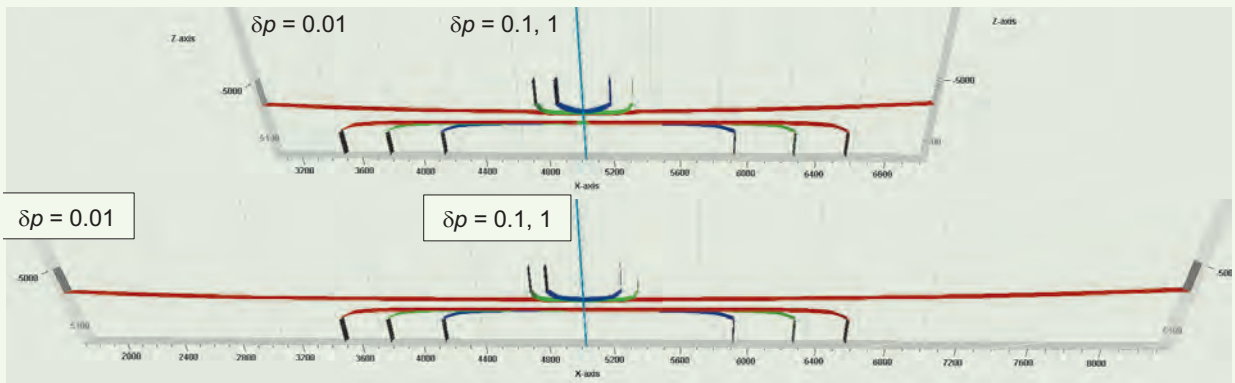

magnitude of the effective flow capacity increases. This increase in flow capacity at a given time depends on the additional region of influence added to the original region of influence at the same time.

Conclusions

1. Heterogeneous reservoir systems are susceptible to changes in flow paths based on production practices and well conditions.
2. Patterns of flow paths control the region of influence around the wellbore for the production from the well. The areal growth of such patterns with continuous production at the well is likely to be spatially nonuniform in any direction for varying degrees of heterogeneity in the reservoir. Assigning a single value to the radius of investigation can be misleading.
3. The region of influence around the wellbore controls the effective magnitude of flow capacity in pressure responses at the wellbore. Any changes in connected reservoir regions will impact the effective flow capacity at the wellbore.
4. The skin factor acts as an influencing factor of controlling the flow pattern around the wellbore, which in turn controls the magnitude of flow capacity in a heterogeneous reservoir system. While calibrating numerical models with the pressure transient data, the skin factor needs to be incorporated in the model along with the permeability updates. Leaving the skin factor calibration to the end can impact the interpretation of the flow capacity.
5. Using numerical models populated with geological knowledge improves the interpretation accuracy and reduces uncertainties in reservoir characterization.

Acknowledgments

The authors would like to thank Shamshudin B. Ahmad and Omar H. Obathani for their valuable assistance during preparation of this manuscript. Review comments of Ibrahim M. Abdulwahab have been very helpful in improving clarity in this article.

This article was presented at the International Petroleum Technology Conference, Dhahran, Saudi Arabia, January 13-15, 2020.

Nomenclature

k_1 = Permeability of top reservoir layer (md)

k_2 = Permeability of bottom reservoir layer (md)

s = Skin factor

s_1 = Skin factor in top reservoir layer

s_2 = Skin factor in bottom reservoir layer

kh = Flow capacity, kh (md-ft)

Δkh = Change in flow capacity, kh (md-ft)

δp = Cutoff for pressure drawdown deep inside reservoir for region of influence (psia)

References

1. Salazar, M.O. and Villa, J.R.: "Permeability Upscaling Techniques for Reservoir Simulation," SPE paper 106679, presented at the Latin American and Caribbean Petroleum Engineering Conference, Buenos Aires, Argentina, April 15-18, 2007.
2. Kuchuk, F.J.: "Radius of Investigation for Reserve Estimation from Pressure Transient Well Tests," SPE paper 120515, presented at the SPE Middle East Oil and Gas Show and Conference, Manama, Kingdom of Bahrain, March 15-18, 2009.
3. Anisur Rahman, N.M., Bin Akresh, S.A. and Al-Thawad, F.M.: "Diagnosis and Characterization of Cross Flow behind Casing from Transient Pressure Tests," SPE paper 174999, presented at the SPE Annual Technical Conference and Exhibition, Houston, Texas, September 28-30, 2015.
4. Larsen, L.: "Determination of Skin Factors and Flow Capacities of Individual Layers in Two-Layered Reservoirs," SPE paper 11138, presented at the SPE Annual Technical Conference and Exhibition, New Orleans, Louisiana, September 26-29, 1982.
5. Peaceman, D.W.: "Interpretation of Well Block Pressures in Numerical Reservoir Simulation," *Society of Petroleum Engineers Journal*, Vol. 18, Issue 3, June 1978, pp. 183-194.
6. Lefkovits, H.C., Hazebroek, P., Allen, E.E. and Matthews, C.S.: "A Study of the Behavior of Bounded Reservoirs Composed of Stratified Layers," *Society of Petroleum Engineers Journal*, Vol. 1, Issue 1, March 1961, pp. 43-58.
7. Prasad, R.S., Al-Attar, B.E.H. and Al-Jasmi, A.K.: "Reservoir Permeability Upscaling Indicators from Well Test Analysis," SPE paper 36175, presented at the Abu Dhabi International Petroleum Exhibition and Conference, Abu Dhabi, UAE, October 13-16, 1996.

About the Authors

Dr. N.M. Anisur Rahman

Ph.D. in Petroleum Engineering, University of Alberta

Dr. N.M. Anisur Rahman is a Senior Petroleum Engineering Consultant with the Well Testing Division of the Reservoir Description and Simulation Department at Saudi Aramco, where he designs and interprets transient tests on hydrocarbon production and water injection wells. Anisur Rahman has also developed analytical solutions to a number of pressure transient models, including methods for short well tests. His interests include production technology, reservoir characterization, and pressure transient analysis.

Prior to joining Saudi Aramco in 2009, Anisur Rahman worked for the Bangladesh University of Engineering and Technology, the University of Alberta, Fekete Associate Inc., and Schlumberger.

He has authored or coauthored 38 technical papers for publication in refereed journals and conference proceedings, and 12 patent documents, of which nine patents have already been granted by the U.S. Patent and Trademark Office. Anisur Rahman was a recipient of the 2016 Society of Petroleum Engineers (SPE) Middle East Regional Reservoir Description and Dynamics Award for his contributions to exceptional service and leadership, and for making significant contributions to the technical discipline. He also serves as a PTA/Well Testing Champion under the Petroleum Engineering Technical Excellence (PETE) and Support Network in Saudi Aramco.

Anisur Rahman received both his B.S. and M.S. degrees in Mechanical Engineering from the Bangladesh University of Engineering and Technology, Dhaka, Bangladesh, and his Ph.D. degree in Petroleum Engineering from the University of Alberta, Edmonton, Alberta, Canada.

He is registered as a Professional Engineer in the Province of Alberta, Canada.

Sukru Sarac

M.S. in Petroleum Engineering, University of Oklahoma

Sukru Sarac is the Well Testing Reservoir Domain Champion for Schlumberger, based in Dhahran, Saudi Arabia. His primary focus areas are well test design and interpretation, multiphase flow metering, perforation design, and fluid analysis.

Previously, Sukru worked as a Reservoir Engineer in Scotland and Norway between 2007 and 2012. Then, he became an instructor in one of Schlumberger's training centers in France. Later, Sukru worked as a Product Champion in Schlumberger's headquarters, responsible for developing numerical well test design and interpretation software, and real-time data analysis software.

He received his B.S. degree from the Middle East Technical University, Ankara, Turkey, and an M.S. degree from the University of Oklahoma, Norman, OK, both in Petroleum Engineering.

Autonomous Reservoir Nano-Agents

Dr. Afnan A. Mashat, Dr. Nan Shi, Dr. Todd Squires, and Dr. Amr I. Abdel-Fattah

Abstract / This article demonstrates the ability of salinity gradients that naturally exist, or could otherwise be induced in the reservoir to target migrate nanoparticles in porous and fractured reservoirs. The nanoparticle's autonomous migration marks a significant milestone toward the development of reservoir nano-agents that self-migrate in deep and hard-to-reach regions in the reservoir without the aid of advective flows.

Direct microscopic visualization experiments were conducted in representative micromodel environments to quantify the displacement and velocity vectors of model nanoparticles in response to different concentration gradients of solutes in the absence of an advective flow. One set of experiments used solutes with different divalent ions and another set used high salinity water to create the concentration gradients.

The nanoparticle's migration distance and speed up or down the imposed gradients were precisely obtained from high-resolution image sequences using particle image velocimetry (PIV) algorithms. The rate at which the particles migrate was calculated and used to validate and extend existing theories to high salinity conditions.

Results showed that in the absence of flow, nanoparticles readily migrate upon exposure to a given gradient, either up or down the gradient, depending on the solute composition (diffusiophoresis (DP)). The rate at which the particles migrate is on the order of μm(s), and was found to be dependent on: (1) the gradient magnitude, (2) the absolute value of the minimum and maximum concentration of the gradient, and (3) ion diffusivities.

The results presented here provide new insights into the transport mechanisms of nanoparticles and microparticles in oil reservoirs where naturally occurring or induced solute and chemical gradients exist. These results provide a platform for the development of reservoir nano-agents that self-migrate in deep and hard-to-reach regions in the reservoir without the aid of advective flows.

Introduction

The potential of using nanomaterials in upstream oil and gas applications has only recently been recognized. In particular, enhanced oil recovery efforts have been exploiting the benefit of using nanomaterials as carriers of treatments and probes[1]. These applications often involve transporting nanomaterials into and out of constricted regions in oil reservoirs to extract trapped oil in dead-end pores. Conventional methods based on convective pressure driven flow have no access to such constricted geometries, due to their significantly high flow resistance. Meanwhile, reservoir stimulation solutions such as applying electromagnetic fields are difficult in remote reservoir locations[2].

To facilitate the delivery treatments or probes in constricted geometries, the autonomous migration of particles when exposed to chemical gradients, i.e., diffusiophoresis (DP), can be exploited. Originally discovered in surface reaction-induced deposition of latex particles[3-5], DP has been exploited in many other new contexts, including dissolving salt crystals[6], soluto-inertial "beacons,"[7] ion exchange membranes[8], osmotic trap for colloids with transient gradients[9], and dynamic clustering of particles[10]. In particular, DP has given rise to the faster transport of nanoparticles into a dead-end pore structure compared to pure diffusion[2, 11].

The quantitative study of DP is not trivial. On the experimental side, direct observation and accurate measurement of DP is challenging, due to the difficulty to establish strong and hydrodynamically stable chemical gradients. On the theoretical side, the classic theory developed[3-5] only applies to gradients of single electrolytes with binary and symmetric ions, e.g., sodium chloride (NaCl)[3]. Subsequently, real reservoir fluids involve divalent and even trivalent ions, so that gradients of multiple and nonsymmetric electrolytes could exist. To account for particle migration in such complex chemical environments, an alternative expression of DP migration velocity, other than ascribed in the classic equation, is required.

Recently, we have developed a versatile microfluidic system with integrated hydrogel microwindow membranes[12, 13], which allows strong and stable gradients to be imposed, a wide range of chemicals tested, and DP migration of individual particles observed and quantified. Using this experimental system, we did not only

characterize particle migration in various gradients, e.g., electrolytes, pH, alcohols, and macromolecules, but we also observed unexpected DP focusing on multiple electrolyte gradients[14]. We further developed a reformulation of the classic expression of DP velocity that can be applied in a general chemical environment, and arbitrary interactions between solute species and particle surfaces.

Here, we describe the direct observation of particle migration in magnesium chloride ($MgCl_2$) and calcium chloride ($CaCl_2$) gradients of different magnitudes and absolute concentration. While DP migration of particles proceeds up both gradients, DP mobility in $MgCl_2$ is much higher than that in $CaCl_2$. Meanwhile, measured values of DP mobility are consistent irrespective of the strength of the gradient or the absolute electrolyte concentration.

We then calculate theoretical DP mobility in both gradients and compare them with those measured in the experiments. In both gradients — more obvious in $CaCl_2$ — the measured DP mobility is smaller than that predicted by theory, largely due to the binding of divalent cations to the carboxylic group at the particle's surfaces, resulting in a reduction of zeta potentials[6].

Finally, we fabricate a microfluidic device with dead-end channel geometry to mimic constricted regions in oil reservoirs. Between the dead end and main channels, a strong salinity gradient is established to evaluate the performance of particle delivery assisted by DP migration. Results from this study further expand the understanding of DP migration under salinity gradients and may provide a rational to design and/or engineer DP-based particle delivery under reservoir conditions.

Methods

Fabrication of Microfluidic Devices

Two different microfluidic devices were used: (1) A three-channel microfluidic device to observe particle migration under different divalent ion gradients, and (2) An H-channel microfluidic device to observe oil droplet migration under high salinity gradients. Both devices were prepared following a standard "microfluidic strikers" method[15].

Figure 1 shows a schematic of the three-channel microfluidic device. The device consists of three channels (height ~10 μm) separated by hydrogel membranes. The hydrogels were prepared following the "hydrogel membrane microwindow" procedure previously described[12].

The other microfluidic device has an H-channel structure. This device was used to create a dead-end channel system to simulate dead-end pores in a reservoir. Following the standard "microfluidic stickers" method, H-junction devices with 15-μm aperture channels were fabricated from glass slides bonded with photo-curable glue (NOA-81). The dimension of two main channels is 10,000 μm long by 500 μm wide, connected by a thinner horizontal channel that is 6,000 μm long and 200 μm wide, Fig. 2a. The horizontal channel was converted to a dead-end channel by permanently blocking one of its ends. This was accomplished by initially filling all channels with high salinity water, then injecting NOA-81 through one of the two main channels. Once penetrated into the horizontal channel, in situ polymerization of NOA-81 via UV light (intensity 30 mW/cm^2) was done quickly — within a few seconds, Figs. 2b to 2d.

Validation of Diffusive Gradients in the Dead-end Channel

We characterize the concentration gradients in the dead-end channels established by the diffusion of a fluorescent dye (sodium fluorescein) as the fluorescent dye (50 mg/250 mL) diffuses into a dead-end channel prefilled with deionized (DI) water, Fig. 3a. The fluorescence intensity is recorded and analyzed with ImageJ (an image processing software) to estimate the relative concentration of the dye. We found that the fluorescence (concentration) profile is well described by the solution to 1D diffusion in semi-infinite space, Fig. 3b[16].

$$\frac{\partial c}{\partial t} = D\frac{\partial^2 c}{\partial x^2} \quad (1)$$

$$\hat{c}(x,t) = 1 - \mathrm{erf}(y) \quad (2)$$

$$y = \frac{x}{\sqrt{4Dt}} \quad (3)$$

where $\hat{c} = \frac{c - c_L}{c_H - c_L}$ is the scaled concentration by the concentration of diffusing solutions c_H and the initial concentration in the dead-end channel c_L. D is the diffusion coefficient and $x = 0$ corresponds to the entrance of dead-end channels.

Image Analysis

The experiments utilized microparticle image velocimetry (μPIV) to measure the migration velocity of particles under different salinity gradients. The detailed steps of the analysis are described in our previous work[13]. Briefly, each image in the recorded movie is divided into small integration windows (64 pixels by 64 pixels) and the μPIV algorithm calculates, frame by frame, the mean velocity from all particles in the field of view.

Fig. 1 *A schematic of the three-channel structure showing the location of the hydrogel membranes and an image of the membranes under the microscope (using a 20x objective).*

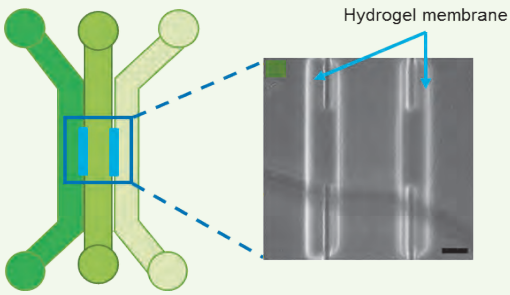

Fig. 2 *Fabrication of a dead-end channel: (a) Schematic of the H-junction microfluidic device structure consisting of two main channels that are connected horizontally by a thinner channel, filled with a solution; (b) Injecting NOA-81 while UV light was spotted on the area to be blocked; and (c) Close up micrograph of the right end of the horizontal channel where UV light was exposed. Once NOA-81 reached the UV, it will become polymerized, yielding a dead-end channel blocked by the solid polymer (d).*

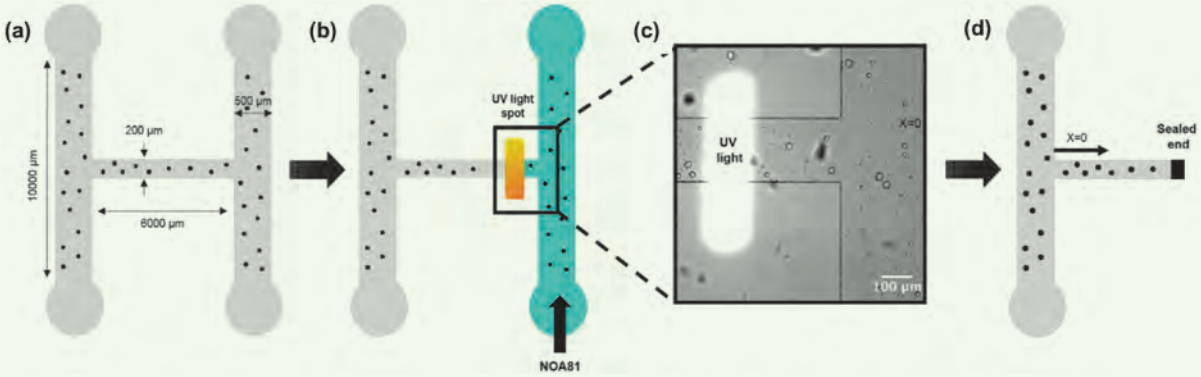

To ensure proper data from the µPIV analysis, significant numbers of the particles in the interrogation region were analyzed. If particle depleted zones existed, we avoided probing particles in these zones. Similarly, accumulated particles at the hydrogel surfaces were excluded to ensure accurate µPIV calculations.

Results and Discussion

Particle Migration in $MgCl_2$ and $CaCl_2$ Gradients: Theoretical DP with Nonsymmetric Divalent Electrolytes

From the classic theory[3-5]:

$$U_{DP} = \frac{\epsilon}{\eta}\left(\frac{k_B T}{e}\right)^2 \left(\frac{\zeta_p}{k_B T/e}\frac{D_+ - D_-}{D_+ + D_-} + 4\ln\cosh\frac{\zeta_p}{4k_B T/e}\right)\nabla \ln n^0, \quad (4)$$

where ϵ and η are the permittivity and the viscosity of the solution, respectively, e is the charge of one electron, ζ_p is the zeta potential of the particle, $D_\pm$ is the diffusion coefficient of cation and anion, and n^0 is the electrolyte concentration.

In Eqn. 4, we can define:

$$D_{DP} = \frac{\epsilon}{\eta}\left(\frac{k_B T}{e}\right)^2 \left(\frac{\zeta_p}{k_B T/e}\frac{D_+ - D_-}{D_+ + D_-} + 4\ln\cosh\frac{\zeta_p}{4k_B T/e}\right). \quad (5)$$

Equations 4 and 5 only apply to binary and symmetric electrolytes, such as NaCl. In addition, studies[17] have given expression of D_{DP} in multiple electrolyte systems with the assumption of small zeta potential of particles ($e\zeta_p/k_B T \ll 1$). For particle ($e\zeta_p/k_B T \sim 1$) migration in $MgCl_2$ and $CaCl_2$ gradients, none of the above methods work.

Alternatively, we can introduce the concept of chemical potential[18-20] $\mu_\pm^0 = Z_\pm\, e\, \phi + k_B T \ln n_\pm^0$ for each ion species in the solution and reformulate the expression of U_DP in general electrolyte gradients[14, 21]:

$$U_{DP} = \nabla\mu_+^0 M_+ + \nabla\mu_-^0 M_-, \quad (6)$$

where $n_\pm^0$ is the concentration of cations and anions in the bulk solution, and $\mathcal{Z}+$ is their corresponding

Fig. 3 *(a) Image sequences showing the fluorescent intensity distribution of sodium fluorescein inside the dead-end channel at different time points; and (b) Temporal fluorescence profiles of fluorescein in the dead-end channel follow the diffusion equation given in Eqns. 1 to 3.*

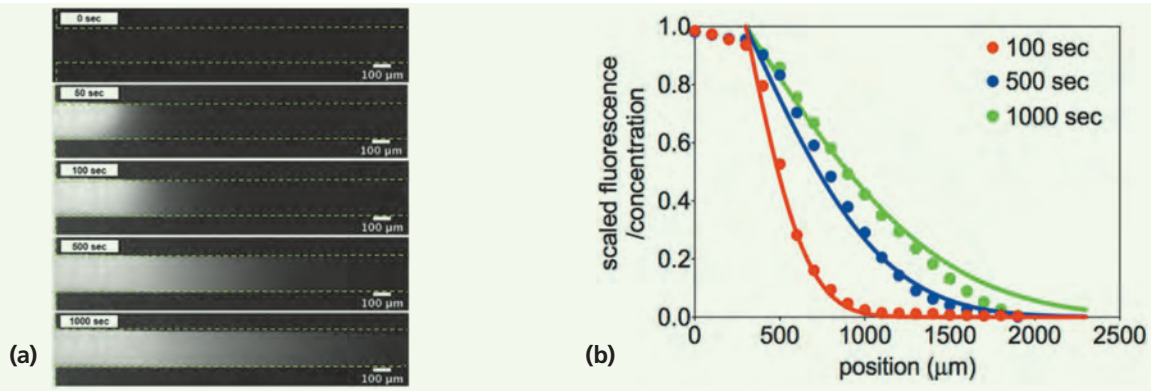

valences. $M+$ is defined as the osmotic mobility of ions that depends on their interaction with the particle surfaces. The gradient of chemical potentials:

$$\nabla\mu_{\pm}^{0} = \mp Z_{\pm}E_s + k_BT\nabla \ln n_{\pm}^{0} \quad (7)$$

represents driving forces on ions, in which E_S is the spontaneous arising electric field, due to ambipolar diffusion of cations and anions[17, 22]. In $MgCl_2$ and $CaCl_2$,

$$E_s = \frac{D_+ - 2D_-}{2(D_+ + D_-)}\frac{k_BT}{e}\nabla \ln n^0 = \beta\frac{k_BT}{e}\nabla \ln n^0 \quad (8)$$

where D_+ is the diffusion coefficient of ions, $n^0 = n_+^0 = 0.5\, n_-^0$ is the concentration of electrolytes in the bulk concentration. Using diffusion coefficients[23] of Mg^{2+} = 706 μm²/s, Ca^{2+} = 792 μm²/s, and Cl^- = 2,032 μm²/s, we have $\beta_{MgCl_2} = -0.61$ and $\beta_{CaCl_2} = -0.58$.

Substituting Eqns. 7 and 8 into Eqn. 6 and rearranging, we get:

$$U_{DP} = [\tfrac{1}{2}M_+(1-2\beta) + M_-(1+\beta)]k_BT\nabla \ln n^0. \quad (9)$$

Therefore, we have:

$$D_{DP} = [\tfrac{1}{2}M_+(1-2\beta) + M_-(1+\beta)]k_BT. \quad (10)$$

As previously mentioned, osmotic mobility depends on the interaction between ions and the particle surface, defined by Eqn. 11[21]:

$$M_{\pm} = \frac{1}{\eta}\int_0^{\infty} z\left(n_{\pm} - n_{\pm}^0\right) dz. \quad (11)$$

The ion concentration, $n_{\pm}$, is connected with their bulk concentration, $n_{\pm}^0$ via the Boltzmann distribution:

$$n_{\pm} = n_{\pm}^0 \exp(-\frac{Z\pm}{k_BT/e}). \quad (12)$$

In particular, the electrostatic potential, ϕ, in the solution follows Poisson's equation:

$$\nabla^2\phi = -\frac{\rho_E}{\epsilon} = -\frac{(n_+Z_+ + n_-Z_-)e}{\epsilon} \quad (13)$$

Substituting Eqn. 12 into Eqn. 13, we can numerically solve for the distribution of ϕ from the particle surface ($\phi = \zeta_p$) to the bulk solution ($\nabla\phi = 0$) using a MATLAB ordinary differential equation solver (bvp4c). After solving for ϕ, we then numerically evaluate the integration in Eqn. 10 to get $M\pm$, which is then substituted into Eqn. 9 to calculate the D_{DP} for particle migration in the $MgCl_2$ and $CaCl_2$ gradients, Fig. 4.

Particle Migration in $MgCl_2$ and $CaCl_2$ Gradients: Experimental Results

We use the three-channel microfluidic device to establish $MgCl_2$ and $CaCl_2$ gradients of different magnitudes and absolute concentration, under which we directly observe and measure the DP velocity of negatively charged polystyrene particles; with a diameter of 0.5 μm (from Bangs Laboatories Inc.). In a typical setup, we prepare $MgCl_2$ and $CaCl_2$ solutions of different concentrations, in the range of 1 mM to 4 mM, which are loaded into the left-hand side channel while DI water goes into the right-hand side channel.

This creates a linear electrolyte concentration gradient in the middle channel, pointing from right toward left. Particles dispersed in electrolyte solutions with a medium concentration between the left-hand side and the right-hand side channels were injected into the middle channel. We started recording particle migration right before stopping the flow in the center channel, using an exposure time of 0.1 second for 1,000 frames. Later, only images after stopping flow are used for image analysis. The analysis was focused on the area between the two hydrogel membranes where the particles were moving.

Figures 5 and 6 shows the DP velocity of particles in different $MgCl_2$ and $CaCl_2$ gradients, respectively — each data point represents the result of multiple runs. To get the D_{DP} value, we adopt the method described in previous work[24]. Briefly, we plot the inverse of the measured DP velocity ($1/U_{DP}$) against the horizontal position in the center channel (x, scaled by the channel width (w = 200 μm)). A linear fitting of this plot allows us to calculate D_{DP}, Tables 1 and 2, based on the slope of the fitting, $1/U_{DP} = x/D_{DP}$ + constant. We also use these fitted D_{DP} values to recalculate the DP velocity, which agrees fairly well with the measured values.

We can now compare experimental and theoretical values of D_{DP}. Negatively charged polystyrene particles

Fig. 4 Distribution of electrostatic potential from particle surface with ζ_p = –50 mV. The distance from the particle surface is measured in terms of Debye screening length, $\lambda_D = \sqrt{\frac{\epsilon k_BT}{2n^0e^2}}$. At the particle surface, $\phi = \zeta_p$, and far from the particle surface, i.e., in the bulk solution, $\phi \approx 0$ and $n_{\pm} = n_{\pm}^0$ from Eqn. 11.

The table presents theoretical D_{DP} values using different zeta potential. Positive values of D_{DP} means negatively charged particles will migrate up both the $MgCl_2$ and $CaCl_2$ gradients.

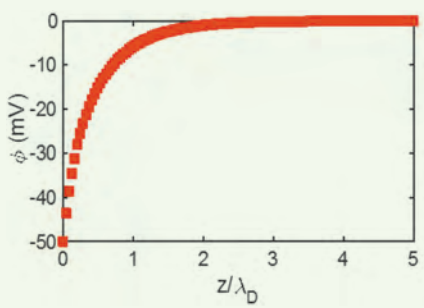

Zeta Potential (mV)	D_{DP} (μm²/s)	
	$MgCl_2$	$CaCl_2$
-10	156.0255	150.45
-20	319.308	314.175
-30	486.75	480.15675
-40	659.325	648.57225
-50	831.9	816.2355

migrate up both the $MgCl_2$ and $CaCl_2$ gradients at the velocity close to 1 µm/s in all conditions, consistent with previous studies with symmetric electrolytes, e.g., NaCl. Moreover, we notice significant smaller D_{DP} values in both gradients compared with their theoretical values, especially for $CaCl_2$.

This could be due to the binding of divalent ions to carboxylic groups at the particle surface that leads to a decrease in zeta potential, which has been re-posted in previous studies[17]. This argument can be further supported by the fact that D_{DP} values are higher when the absolute electrolyte concentration is smaller in both the $MgCl_2$ and $CaCl_2$ gradients.

Establishing High Salinity Gradients to Deliver Particles into Dead-end Channels

To mimic the flow restricted regions in oil reservoirs, we compared the migration of particles into dead-end channels with and without salinity gradients. In the control experiment (no salinity gradients), the dead-end channel was filled with DI water inside. Then, a solution of polystyrene particles dispersed in DI water

Fig. 5 *Velocity of particle migration under different concentration gradients of $MgCl_2$: (a) 4 mM-2 mM-0 mM, and (b) 2 mM-1 mM-0 mM, measured by PIV. The concentration gradients represent the right, middle, and left channels, respectively. (c) The streakline image shows the DP motion in the area between the hydrogel membranes in the center channel — left-hand side with a higher concentration of $MgCl_2$.*

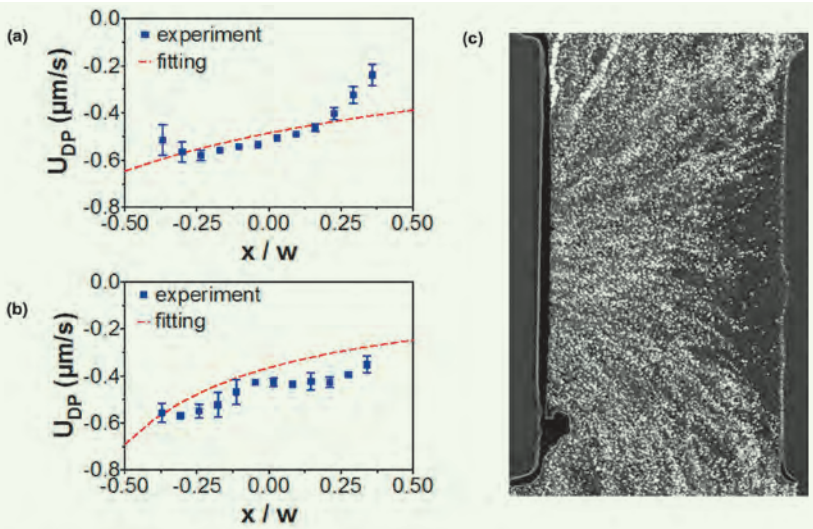

Fig. 6 *Velocity of particle migration under different concentration gradients of $CaCl_2$: (a) 4 mM-2 mM-0 mM, and (b) 2 mM-1 mM-0 mM, measured by PIV. The concentration gradients represent the right, middle, and left channels, respectively. (c) The streakline image shows the DP motion in the area between the hydrogel membranes in the center channel — left-hand side with a higher concentration of $CaCl_2$.*

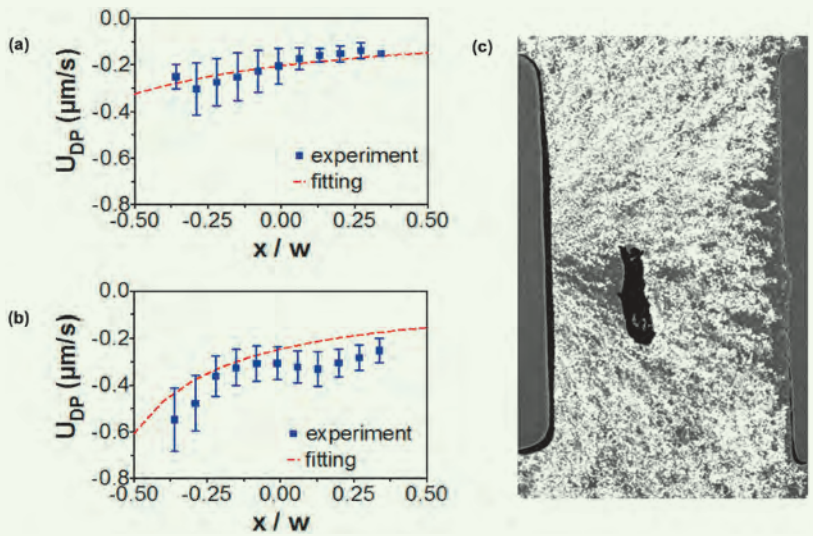

Table 1 *Particle mobility calculated from the DP experiment results under different concentration gradients of $MgCl_2$.*

Gradient in Channel			Measurement Method	D_{DP} (μm²/s)
Left	**Middle**	**Right**		
4 mM $MgCl_2$	2 mM $MgCl_2$	0 mM $MgCl_2$	PIV	78.3 ± 4.7
2 mM $MgCl_2$	1 mM $MgCl_2$	0 mM $MgCl_2$		207.7 ± 21.9

Table 2 *Particle mobility calculated from the DP experiment results under different concentration gradients of $CaCl_2$.*

Gradient in Channel			Measurement Method	D_{DP} (μm²/s)
Left	**Middle**	**Right**		
4 mM $CaCl_2$	2 mM $CaCl_2$	0 mM $CaCl_2$	PIV	44.45 ± 5.3
2 mM $CaCl_2$	1 mM $CaCl_2$	0 mM $CaCl_2$		71 ± 24.3

was injected through the main channel and kept flowing, Fig. 7a, while the migration of particles in the dead-end channels was monitored over time, Fig. 7b.

Without any gradients, the particles transported into the dead-end channel, dominated by diffusion, is very slow. By contrast, in the experiment with salinity gradients, the dead-end channel was filled with high salinity water, Fig. 7c. By flushing the main channel with particles dispersed in DI water (the same as in the control experiment), the salinity differences between the main and dead-end channels establishes a salinity gradient that significantly drives the migration of particles into the dead-end channel, Fig. 7d.

Conclusions

The migration of particles was tested under different

Fig. 7 *Schematic of a dead-end channel filled with DI water (a); filled with high-salinity water (b); followed by the injection of dispersed particles through the main channel. (c) and (d) are image sequences of particles transported over time for the control (no salinity gradient), and the actual experiment (under salinity gradient), respectively.*

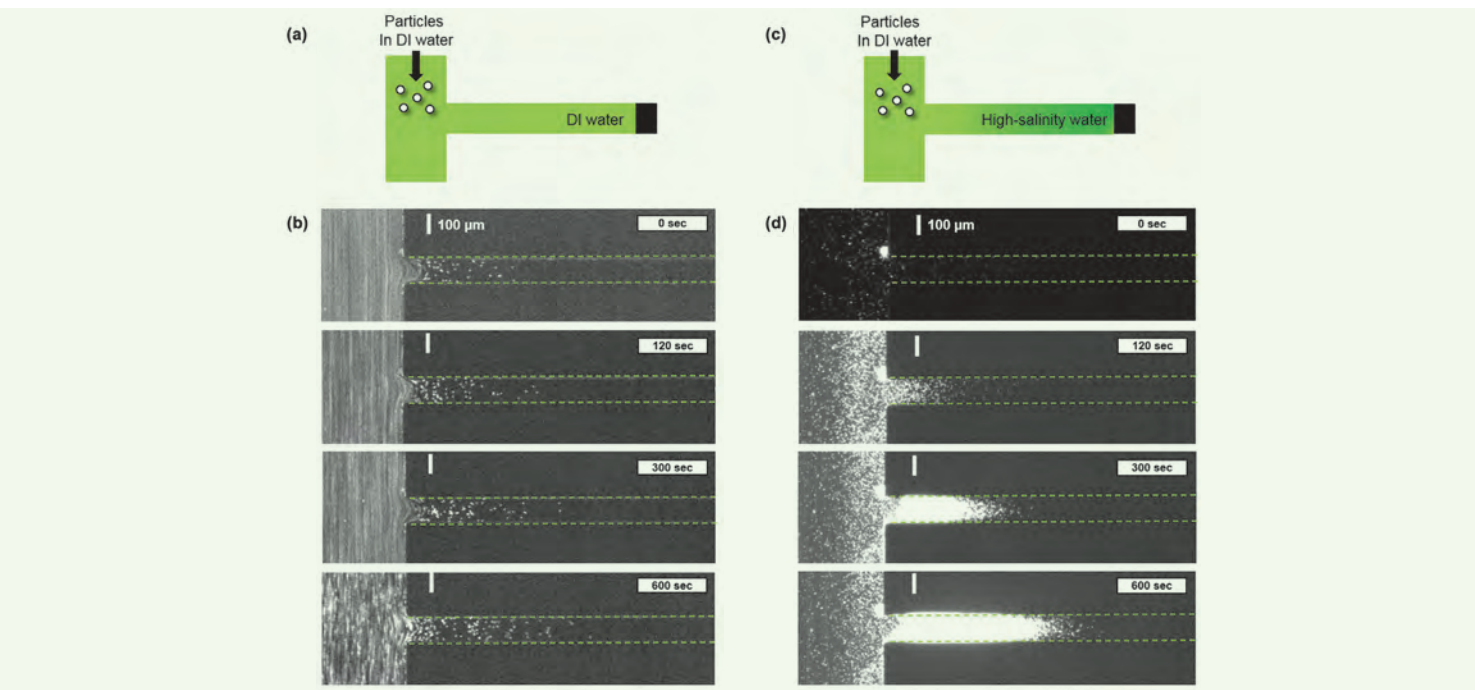

salinity gradients using two different microfluidic devices. The three-channel microfluidic device was used to test the DP mobility under different concentrations of $MgCl_2$ and $CaCl_2$, which are usually presented in oil reservoirs. A dead-end channel was fabricated using the H-junction microfluidic device, which was used to test the migration of particles under high salinity water gradients.

All experiments showed the migration of particles up gradients. The results presented here help in providing a better understanding of the transport mechanisms of nanoparticles and microparticles in dead-end pores in oil reservoirs where chemical gradients exist.

Acknowledgments

This article was prepared for presentation at the 21st SPE Middle East Oil and Gas Show and Conference, Manama, Kingdom of Bahrain, March 15-18, 2021.

References

1. Negin, C., Ali, S. and Xie, Q.: "Application of Nanotechnology for Enhancing Oil Recovery — A Review," *Petroleum*, Vol. 2, Issue 4, December 2016, pp. 324-333.
2. Kar, A., Chiang, T-Y., Ortiz Rivera, I., Sen, A., et al.: "Enhanced Transport into and Out of Dead-End Pores," *ACS Nano*, Vol. 9, Issue 1, January 2015, pp. 746-753.
3. Derjaguin, B.V., Sidorenkov, G., Zubashchenko, E. and Kiseleva, E.: "Kinetic Phenomena in the Boundary Layers of Liquid 1. The Capillary Osmosis," *Progress in Surface Science*, Vol. 43, Issues 1-4, May-August 1993, pp. 138-152.
4. Prieve, D.C., Smith, R.E., Sander, R.A. and Gerhart, H.L.: "Chemiphoresis: Acceleration of Hydrosol Deposition by Ionic Surface Reactions," *Journal of Colloid Interface Science*, Vol. 71, Issue 2, September 1979, pp. 267-272.
5. Prieve, D.C., Anderson, J.L., Ebel, J.P. and Lowell, M.E.: "Motion of a Particle Generated by Chemical Gradients. Part 2. Electrolytes," *Journal of Fluid Mechanics*, Vol. 148, November 1984, pp. 247-269.
6. McDermott, J.J., Kar, A., Daher, M., Klara, S., et al.: "Self-Generated Diffusioosmotic Flows from Calcium Carbonate Micropumps," *Langmuir*, Vol. 28, Issue 44, October 2012, pp. 15491-15497.
7. Banerjee, A., Williams, I., Azevedo, R.N., Helgeson, M.E., et al.: "Soluto-Inertial Phenomena: Designing Long-Range, Long-Lasting, Surface Specific Interactions in Suspensions," *Proceedings of the National Academy of Science*, Vol. 113, Issue 31, July 2016, pp. 8612-8617.
8. Florea, D., Musa, S., Huyghe, J.M. and Wyss, H.M.: "Long-Range Repulsion of Colloids Driven by Ion Exchange and Diffusiophoresis," *Proceedings of the National Academy of Science*, Vol. 111, Issue 18, May 2014, pp. 6554-6559.
9. Palacci, J., Cottin-Bizonne, C., Ybert, C. and Bocquet, L.: "Osmotic Traps for Colloids and Macromolecules Based on Logarithmic Sensing in Salt Taxis," *Soft Matter*, Vol. 8, Issue 4, 2012, pp. 980-994.
10. Theurkauff, I., Cottin-Bizonne, C., Palacci, J., Ybert, C., et al.: "Dynamic Clustering in Active Colloidal Suspensions with Chemical Signaling," *Physical Review Letters*, Vol. 108, Issue 26, June 2012, pp. 268303-1 to 268303-5.
11. Shin, S., Um, E., Sabass, B., Ault, J.T., et al.: "Size-Dependent Control of Colloid Transport via Solute Gradients in Dead-End Channels," *Proceedings of the National Academy of Science*, Vol. 113, Issue 2, January 2016, pp. 257-261.
12. Paustian, J.S., Nery-Azevedo, R., Gilkey, M.J., Lundin, S-T.B., et al.: "Microfluidic Microdialysis: Spatiotemporal Control over Solution Microenvironments Using Integrated Hydrogel Membrane Microwindows," *Physical Review X*, Vol. 3, Issue 4, October-December 2013, pp. 041010-1 to 041010-13.
13. Paustian, J.S., Angulo, C.D., Nery-Azevedo, R., Shi, N., et al.: "Direct Measurements of Colloidal Solvophoresis under Imposed Solvent and Solute Gradients," *Langmuir*, Vol. 31, Issue 15, March 2015, pp. 4402-4410.
14. Shi, N., Nery-Azevedo, R., Abdel-Fattah, A.I. and Squires, T.M.: "Diffusiophoresis Focusing on Suspended Colloids," *Physical Review Letters*, Vol. 117, Issue 25, December 2016, pp. 258001-1 to 258001-5.
15. Bartolo, D., Degre, G., Nghe, P. and Studer, V.: "Microfluidic Stickers," *Lab on a Chip*, Vol. 8, Issue 2, March 2008, pp. 274-279.
16. Bird, R.B., Stewart, W.E. and Lightfoot, E.N.: *Transport Phenomena*, 2nd edition, New York: John Wiley & Sons, 2001, 895 p.
17. Chiang, T-Y. and Velegol, D.: "Multi-ion Diffusiophoresis," *Journal of Colloid and Interface Science*, Vol. 424, June 2014, pp. 120-123.
18. Ohshima, H., Healy, T.W. and White, L.R.: "Approximate Analytic Expressions for the Electrophoretic Mobility of Spherical Colloidal Particles and the Conductivity of their Dilute Suspensions," *Journal of Chemical Society, Faraday Transactions 2*, Vol. 79, 1983, pp. 1613-1628.
19. Probstein, R.F.: *Physicochemical Hydrodynamics: An Introduction*, 2nd edition, New York: John Wiley & Sons, 1994, 400 p.
20. Chu, K.T. and Bazant, M.Z.: "Surface Conservation Laws at Microscopically Diffuse Interfaces," *Journal of Colloid and Interface Science*, Vol. 315, Issue 1, November 2007, pp. 319-329.
21. Squires, T.M.: "Particles in Electric Fields," Chapter 5 in *Fluids, Colloids and Soft Materials: An Introduction to Soft Matter Physics*, Fernandez-Nieves, A. and Puertas, A.M. (eds.), John Wiley & Sons, 2016, 432 p.
22. Anderson, J.L.: "Colloid Transport by Interfacial Forces," *Annual Review of Fluid Mechanics*, Vol. 21, Issue 1, November 2003, pp. 61-99.
23. Cussler, E.L.: *Diffusion Mass Transfer in Fluid Systems*, Cambridge University Press, 1984, 536 p.
24. Nery-Azevedo, R., Banerjee, A. and Squires, T.M.: "Diffusiophoresis in Ionic Surfactant Gradients," *Langmuir*, Vol. 33, Issue 38, August 2017, pp. 9694-9702.
25. Mashat, A., Abdel-Fattah, A. and Gizzatov, A.: "NanoSurfactant: A Novel Nanoparticle-based EOR Approch," SPE paper 190861, presented at the SPE EUROPEC featured at the 80th EAGE Conference and Exhibition, Copenhagen, Denmark, June 11-14, 2018.

About the Authors

Dr. Afnan A. Mashat

Ph.D. in Environmental Science and Engineering,
King Abdullah University of Science and Technology

Dr. Afnan A. Mashat joined the Reservoir Engineering Technology Division of Saudi Aramco's Exploration and Petroleum Engineering Center – Advanced Research Center (EXPEC ARC) in July 2015. Her research interests include using nanomaterials for enhanced oil recovery and improved oil recovery applications. Prior to joining Saudi Aramco, Afnan was working on nanomaterials for drug release and delivery applications.

She received her B.S. degree in Microbiology from King Abdulaziz University, Jiddah, Saudi Arabia, and her M.S. and Ph.D. degrees in Environmental Science and Engineering from King Abdullah University of Science and Technology, Thuwal, Saudi Arabia.

Dr. Nan Shi

Ph.D. in Chemical Engineering,
Texas A&M University

Dr. Nan Shi is a contracted Petroleum Engineer at the Reservoir Engineering Technology Division of Saudi Aramco's Exploration and Petroleum Engineering Center – Advanced Research Center (EXPEC ARC). His research interests include transport, fluid flow, and colloidal/interfacial phenomena in reservoirs. Nan's work integrates both an experimental and computational approach to understanding and applying microscale physics in reservoir processes.

Prior to joining Saudi Aramco in 2018, he worked as a Postdoctoral Research Associate in the Department of Chemical Engineering, University of California at Santa Barbara, where he studied the autonomous migration of particles driven by chemical gradients and biophysics of oil degrading bacterial species.

Nan received his B.S. degree from Zhejiang University, Zhejiang, China, and his Ph.D. degree from Texas A&M University, College Station, TX, both in Chemical Engineering.

Dr. Todd Squires

Ph.D. in Physics,
Harvard University

Dr. Todd Squires is Professor of Chemical Engineering at UC Santa Barbara. His research includes theoretical and experimental studies, targeting both fundamental and applied questions in complex fluids and multifunctional mixtures, dynamics, and rheology of surfactant-laden interfaces, and microfluidic and electrokinetic systems.

His honors include an APS fellowship, the GSOFT Early Career Award, the Francois Frenkiel Award, Beckman Young Investigator, Camille & Henry Dreyfus Teacher-Scholar, and the NSF CAREER Award.

Todd received his B.S. degree in Physics from the University of California Los Angeles, Los Angeles, CA, and his Ph.D. degree in Physics from Harvard University, Cambridge, MA.

Dr. Amr I. Abdel-Fattah

Ph.D. in Chemical and Nuclear Engineering,
University of New Mexico

Dr. Amr I. Abdel-Fattah is a Petroleum Engineering Specialist and Team Leader of the In-Situ Sensing and Intervention focus area in Saudi Aramco's Exploration and Petroleum Engineering Center – Advanced Research Center (EXPEC ARC). He joined EXPEC ARC's Reservoir Engineering Technology Division in late 2012 after working 16 years with the Los Alamos National Laboratory in New Mexico, U.S., where he reached a Senior Scientist status. Amr is currently spearheading a number of research and technology development programs in EXPEC ARC geared at utilizing nanotechnology for upstream oil and gas applications.

He has over 30 years of experience in subsurface energy and environmental applications of nanotechnology, colloid and interface science, and electrokinetics. Amr is a Society of Petroleum Engineers (SPE) Distinguished Lecturer, a founding Board Member of the International Association of Electrokinetics, a U.S. Representative on the International Board of Electrokinetics, a Technical Member on the Science Advisory Board of the International Association of Colloid and Interface Scientists, and a Guest Editor for the international *Journal of Colloids and Surfaces A*. He has published numerous papers in international journals, including some of the world's premier and most cited journals, and delivered numerous plenary and invited talks and lectures worldwide. Amr chaired the International Electrokinetics Conference in Santa Fe, NM, in 2008, in addition to several international workshops and conference sessions in the U.S., Canada, and Europe since 2005.

He received his B.S. degree in Civil Engineering and an M.Eng. in Geotechnical Engineering from Ain Shams University, Cairo, Egypt. Amr received his M.S. degree and his Ph.D. degree in Chemical and Nuclear Engineering from the University of New Mexico, Albuquerque, NM.

Reservoir Description Insights from Interwell Gas Tracer Test

Dr. Abdulaziz S. Al-Qasim, Dr. Sunil L. Kokal, Sven K. Hartvig, and Dr. Olaf K. Huseby

Abstract / Tracer technology has gained considerable attention recently as an effective tool in the reservoir monitoring and surveillance toolkit, particularly in improved oil recovery (IOR) operations. Gas flow paths within the reservoir can be quite different from liquid — oil and water — flow paths. This is primarily due to gravity override, and differences in density and relative permeability between the gas and liquid phases.

An interwell gas tracer test (IWGTT) is a key monitoring and surveillance tool for any IOR project. The IWGTT should be designed and implemented to track the flow behavior of the gas phase. The test generally entails injecting a small amount of unique perflouro-hydrocarbon tracers into the gas phase injectant stream. The IWGTT has been conducted on a limited number of fields across the globe, and sample results of some will be presented.

The sampling frequency of the tracers from the producers should be designed carefully to collect the necessary data that will provide insights about the connectivity between the injector and producer well pairs, gas breakthrough times ("time of flight"), and possible interwell fluid saturations. Different fit-for-purpose unique tracers can be deployed in the subject injector(s) stream, and their elution can be monitored in the corresponding updip producer(s).

In addition to reservoir connectivity and breakthrough times between injector and producer pairs, an IWGTT helps in optimizing water altering gas (WAG) operations and production strategies for gas injection projects, improving sweep efficiency and ultimately enhancing oil recovery. It can also be used to identify the source of inadvertent gas leakage into shallow aquifers or soil gas, and help in the planning and placement of future wells.

This article reviews the workflow and necessary logistics for the successful deployment of an IWGTT. It will provide the best practices for designing, sampling, analyzing, and interpreting a gas tracer deployment. This article also highlights the benefits of gas tracer data, and their usefulness in understanding well interconnectivity and dynamic fluid flow in the reservoir. The results can be used to refine the reservoir simulation model and fine-tune its parameters. This effort should lead to better reservoir description and an improved dynamic simulation model. The challenges associated with the IWGTT will also be shared.

Introduction

Tracers are used in the oil industry to qualitatively or quantitatively gauge how fluid flows through the reservoir, and are also a useful tool for estimating residual oil saturation. It is one of the technologies that can be deployed for surveillance and monitoring of any (injectant related) improved oil recovery (IOR) project.

Tracers are compounds injected in a well, with the main goal of producing from the same well — using a single well tracer test — or in a different well — using an interwell tracer test (IWTT). In IWTTs, the tracer is injected in one well along with the carrier fluid (water in a waterflood or gas in a gasflood) and then detected in a producing well after a period of time, which can be anything from days, weeks, months or years. In single well tracer tests, the tracer is injected into the formation from a well and later produced from the same well. The interplay of the tracer amount injected, produced, and breakthrough times, along with the interval of injection, allows the capture of some key information about the subsurface, such as fluid flow characteristics, estimation of the remaining — or sometimes residual — oil saturation and its distribution, which may be difficult to acquire by other means.

Tracer technology was first applied in hydrology to monitor the movement of groundwater in the early 1900s. Applications of tracers in the petroleum industry did not start until nearly half a century later[1]. Tracers reflects the reservoir's flow dynamics. When properly deployed, tracers can render information that is nearly impossible with other methods, such as identifying flow paths, breakthrough times from injector to producers, and estimations of the interwell oil saturation. The following are some key applications of tracers in upstream exploration and production operations[1-3]:

- Volumetric sweep: The volume of fluid displaced in an injection well until breakthrough of the traced fluid at an offset producer is a measure of the volumetric sweep efficiency between that pair of wells. The volume and timing of detected tracers relative to the interwell pore volume (PV) would indicate the presence of an interwell open fracture, thief zone (or Super-K zone) and could also give an indication of the volume of such conductive channel(s).
- Investigation of communication across fault(s): In this case, a tracer is injected on one side of the fault and the producers on the other side of the fault(s) are monitored for tracer arrival.
- Delineation of flow barriers: Usually sealing faults (faults with large displacement along the fault plane) and permeability pinchouts can represent barriers to the flow of fluids perpendicular to their axis. In addition to the bottom-hole pressure build up surveys used to infer/detect such barriers, tracers can be used to delineate the course of such flow barriers.
- Improving reservoir description by defining the interwell communication and flow paths: This involves the injection of different tracers at each injector and monitoring all the producers for all of the tracers.
- Determination of the existence of an attic oil volume: In this scenario, two or more tracers are injected from the same injector at a different time. The simultaneous arrival of the tracers might indicate the existence of an attic volume.
- Tagging relative velocities of injected fluids: When different fluids are injected simultaneously, alternatively or sequentially in the same well, e.g., traced solvent and traced water during alkaline/surfactant/polymer (ASP) or water altering gas (WAG) flooding, with each fluid tagged with a different non-adsorbing tracer, the relative velocities of these fluids can be measured from the individual arrival time at the offset producers. The early arrival of one of the traced fluids at the producer would indicate that the early arriving fluid has contacted less of the reservoir compared to the slower fluid, Fig. 1.
- Confirmation of miscibility during gas injection: This also involves a simultaneous injection of two tracers with different partitioning coefficients into the reservoir. The simultaneous arrival of the two tracers to the producer(s) indicates single-phase flow conditions in the reservoir.
- Estimation of the remaining oil saturation: This involves a simultaneous injection in the water phase of two tracers with different partitioning coefficients to the oil. The difference of the retention time of the two tracers provides estimates of the residual or remaining oil saturation. A variant of this can be applied to the following:
    a. Connate water saturation determination
    b. Waterflood assessment
    c. Evaluating the efficacy of IOR projects
- Monitoring stimulation, fracturing and gravel pack operations: Tracer techniques can accurately profile both the solid and the liquid phases during stimulation operations, sand fracturing, gravel pack and acid solid/fluids positioning.
- Cement squeeze or grouting operations: Unlike conventional temperature or electronic surveys, specialized tracer techniques can be used to locate cement when more than one steel tube wall lies

Fig. 1 *The IWTT for IOR applications. Courtesy of the Institute for Energy Technology.*

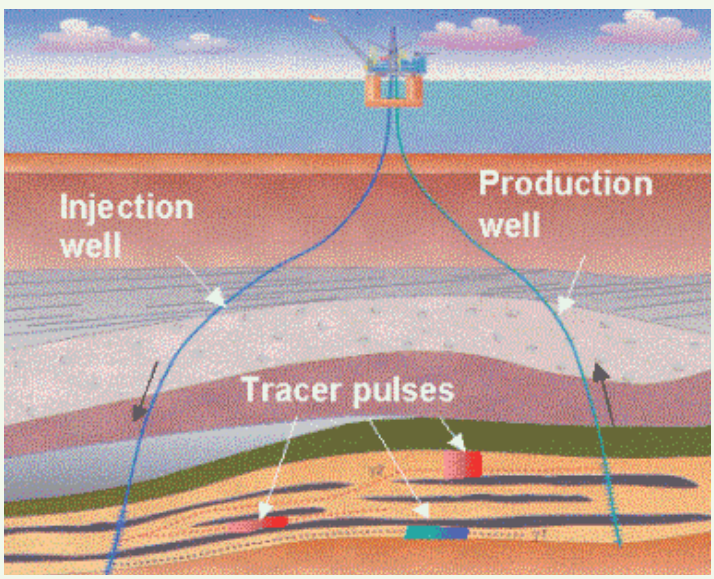

between the cement and the logging system. In the case of grouting or cement squeeze operations, a tracer may be added to the cement material at the surface. Following cement setting, a logging tool can be lowered downhole and an accurate profile obtained of the cement position.

In addition, tracers have been deployed for the surface and downtream applications in exploration and production. Tracers have been used for flow rate measurements and flow regime applications in pipe and gathering lines, pipeline leak detection, flow separator efficiency tests, and refinery surveys. They are also used for monitoring underground gas storage, scale and corrosion monitoring, and sometimes for solving environmental problems.

There are no generally agreed classification of tracers in the literature for the oil and gas industry; tracers may broadly be classified as passive or active. A passive tracer blindly follows the fluid phase in which it is injected, while active tracers interact with other fluids, or with the rock surface in the porous media. Tracers have been identified in many ways: radioactive tracers and nonradioactive tracers by radioactivity; partitioning tracers and nonpartitioning (ideal) tracers by functionality; water tracers and gas tracers by the state of material; and single well tracer and interwell tracer by field implementation[4]. Among these identifications, the premier distinction of water tracers and gas tracers is often utilized[1]. Figure 2 presents an overall classification based on this distinction.

Technology Background and Objectives

Interwell gas tracers tests (IWGTT) can be used to determine whether a gas flood is first contact miscible, or if free gas flow does exist during gas injection. In addition, when different fluids are injected simultaneously, alternatively or sequentially in the same well during ASP or WAG flooding, non-absorbing tracers can measure the relative velocities of these fluids and individual arrival time at the offset producers, thereby giving a good insight into single or multiphase flow conditions in the reservoir.

The IWGTTs are used as a comprehensive monitoring and surveillance tool to evaluate the performance of an IOR project for reservoirs that have been undergoing gas injection. Any typical IOR project consists of a set of injectors, a set of observation wells, and a set of producers that are drilled to test the impact of water injection on recovery, prior to any IOR injectant being introduced, Fig. 3. It should be noted that the reservoir simulation streamline simulation study made ahead of the IOR project showed tramline communication between the injector and direct producer pairs.

The main objectives of the IWGTT are to: (a) understand the injectant's flow paths and connectivity between injector and producer pairs; (b) identify inadvertent leakage (if any) into a shallow aquifer (Neogene) or soil gas; (c) optimize production/injection strategy; (d) use the tracer data to refine static and dynamic reservoir models; (e) help in future planning/selection/placement of updip wells; and (f) push the envelope on tracer technology. The breakthrough times are

Fig. 2 *Classification of tracers for interwell and/or single well applications[1].*

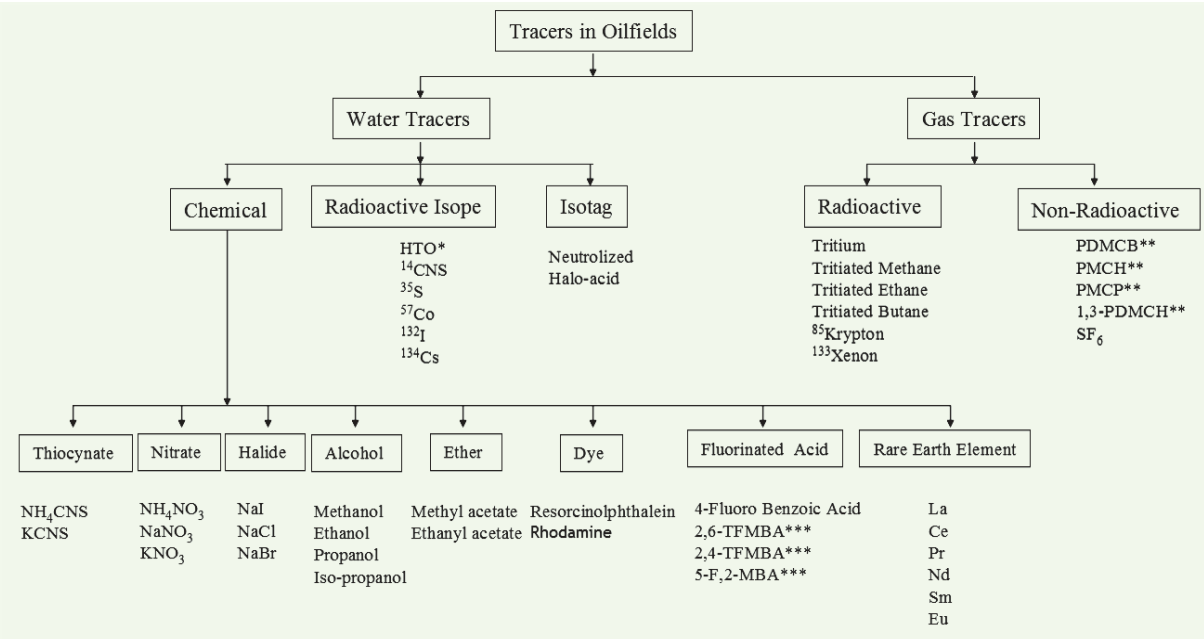

* HTO – Tritiated water
** PDMCB: perfluorodimethylcycyclbutane; PMCH: perfluoromethylcyclopentane; PMCP: perfluoromethylcyclopentane, 1,3 PDMCH: 1,3-perfluorodimethylcyclohexane
***2,6-TFMBA: 2,6-bis(trifluoromethyl) benzoic acid; 2,4-TFMBA: 2,4-bis(trifluoromethyl) benzoic acid; 5F,2-MBA: 5-fluoro, 2-methyl benzoic acid;

Fig. 3 *A typical IOR project test area, showing a set of injector wells (E-1 to E-4), and corresponding producer wells (B-1 to B-4).*

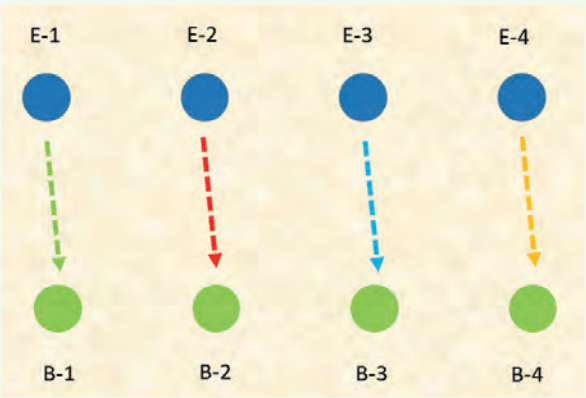

essential in assessing the robustness of the static and dynamic simulations for evaluating the IOR project.

This article summarizes results from an interwell chemical gas tracer study as part of a comprehensive monitoring and surveillance plan to evaluate the performance and sweep efficiency of injectants. The test area is a partially depleted down flank part of a Jurassic age reservoir that has been undergoing peripheral water injection for many decades. The test area consists of a set of injectors (E-1, E-2, E-3, and E-4), a set of observation wells (M-1 and M-2), and a set of corresponding producers (B-1, B-2, B-3, and B-4).

Water tracer results were previously summarized[5]. The current article focuses on gas tracer monitoring of the injectant plumes.

The injectant plumes in the four wells in the test area were traced using four different tracers — one tracer per well — Table 1. In addition to the tracers in Table 1, a mass of 0.85 kg of the tracer candidate (IFE-GT-7) was injected to qualify it for use as a reservoir tracer in gas applications. The tracer candidate IFE-GT-7 was injected simultaneously with PMCH in the B-2 injector well.

Field Implementation and Sampling

The producer wells (B-1 to B-4) were put on production for several months to evaluate their performance before drilling the corresponding injector wells. The injectors were then switched on to see their impact on the producers. The IWGTT was then commenced, during which gas tracers were injected shortly after the injectors were switched on.

Additionally, four different unique water tracers were injected in four different wells — one tracer per well — together with four pilot tracers, injected to verify the pilot tracers' applicability in real field cases[5].

For sampling, the Chemical Adsorption Tube (CAT) technology was used, Fig. 4. This technology allows for adsorption of all tracer mass from a known volume of reservoir gas. This mass is then extracted at an off-site laboratory, and concentrations in the reservoir gas are accurately measured. The CATs are unpressurized and easy to ship, compared to alternative methods that require shipment of reservoir gas samples in pressurized cylinders.

Given the importance of a tracer sampling protocol on the success of any IWGTT operation, the sampling procedure adopted ensured that the sampling frequency was congruent with anticipated possible breakthrough times. Sanni et al. (2016)[6] enumerated some of the steps taken by the sampling team. The key steps are:

- The sampling frequency was designed to ensure that early breakthrough times for the tracers are not missed. High frequent sampling (twice a week) at the beginning; then sampling every two weeks; and less frequent sampling (monthly) toward the end, Table 2.
- Field personnel were trained to the follow the sampling protocol developed for the project.

Fig. 4 *Picture of a CAT used to sample reservoir gas tracers. The length of the total CAT system is about 22 cm.*

Table 1 *Tracers injected in the test area's four wells.*

Well	Tracer	Injection Date	Mass (kg)	Boiling Point (°C)	Vapor Pressure (mbar)	Vapor Density at 25 °C (kg/l)
E-1	PMCP	February 1, 2017	0.85	48	451	0.0135
E-2	PMCH	March 13, 2017	0.90	76	141	0.0125
E-3	PECH	February 1, 2017	0.92	101.7	28.7	0.0131
E-4	n-PPCH	March 13, 2017	0.95	130	10	No data

Table 2 *Sampling frequency plan.*

Time After First Injection (t)	Sampling Frequency	No. of Samples per Well during Time Interval	Total No. of Samples during Time Interval
t < 8 weeks	Twice a week	15	60
9 weeks < t < 12 weeks	Weekly	4	16
13 weeks < t < 27 weeks	Every two weeks	7	28
27 weeks < t < 52 weeks	Monthly	6	24

- Samples were clearly labeled for each collection to avoid contamination.
- Ensure good communication ability between the office and field personnel to ensure alignment of objectives and priorities.

A high frequency sample rate was applied at the early part of the project for about six months. This resulted in a lot of samples. Only a selection of the collected samples were analyzed until the tracer was detected in the samples. Afterward, some additional samples were analyzed from the pool of collected samples to narrow down the exact breakthrough times for the water tracers. It is important to highlight that these tracers were designed to be detected at very low detection limits, i.e., in the range of parts per trillion.

Subsequently, the sampling frequency and sample analysis were optimized to provide reasonable data points to generate the tracer response curves (elusion concentration vs. time) for each well.

Tracer Curve Analysis and Reservoir Information

As summarized in previous work[5, 7-9], residence time distribution analysis, introduced by Shook (2003)[10] and Shook and Forsmann (2005)[11], has proven to be an effective manner to analyze ordinary tracer tests, as well as partitioning interwell tracer tests. Next, we recollect the previously presented methodology[5, 7-9].

The distribution of times used by a population of passive tracer particles to travel through a medium can be used to quantify the flow through that medium. The tracer particles travel through different paths, and therefore use different amounts of time to travel from the inlet to the outlet. The distribution, $E(t)$ of these times is called the exit age distribution, or residence time distribution, of the fluid in the system. $E(t)$ is defined from produced tracer concentrations, $C(t)$, production rate, $Q_p(t)$, and injected tracer amount, M, as:

$$E(t) = C(t) \cdot Q_p(t)/M \quad (1)$$

The unit of E is the inverse of the time unit. If a system has one injector and multiple producers, j, with production rates, Q_j, we can then define the residence time distributions between each j as:

$$E_j(t) = C_j(t) \cdot Q_j(t)/M \quad (2)$$

In a closed system, mass balance requires that:

$$\sum_j \int_{-\infty}^{\infty} E_j(t)dt = 1 \quad (3)$$

where the sum is over all producers.

The three first moments of the residence time distribution are given as:

$$m_0 = \int_{-\infty}^{\infty} E_j(t)dt\,,\ m_1 = \int_{-\infty}^{\infty} t \cdot E_j(t)dt \text{ and}$$

$$m_2 = \int_{-\infty}^{\infty} t^2 \cdot E_j(t)dt \quad (4)$$

The zero order moment (m_0) represents the relative amount of tracer produced in production well j, the first order moment (m_1) represents the average residence time for the tracers between the injection well and j, and the second order moment (m_2) is related to the dispersion of the tracers.

Shook (2003)[10] and Shook and Forsmann (2005)[11] introduced a method to characterize the flow and geometry of a system using the residence time distribution. Briefly, two functions, the flow capacity, $F(t)$, and the storage capacity, (t), can be defined as:

$$F(t) = \frac{1}{m_{0,j}} \int_0^t E_j(\tau)d\tau \text{ and}$$

$$\Phi(t) = \frac{1}{m_{1,j}} \int_0^t \tau \cdot E_j(\tau)d \quad (5)$$

and combined in a $F-\Phi$ diagram to quantify a measure of the heterogeneity of the system. The swept reservoir volume as a function of time can be estimated from $F(t)$. For a water tracer, it is given as[12]:

$$V_{s,j}(t) = \int_0^t Q_j(\tau)\big(1 - F(\tau)\big)d\tau \quad (6)$$

In cases where produced fluid is re-injected, contributions due to re-injection can be removed using de-convolution[7].

Moment analysis of tracer curves requires normalization of residence time distributions integrated to infinity.

As tracer campaigns (including the present one) is ended at a finite time after injection, integration to infinity must be based on extrapolation of the tracer curves. Various extrapolation methodologies have been previously proposed[7, 11, 13]. We used the approach proposed by Viig et al. (2013)[7], based on fitting type curves of the form:

$$C(t) = \frac{A_0}{\sqrt{D_0 t}} exp\left[-\frac{(t-t_0)^2}{D_0 t}\right] \quad 7$$

with three parameters: A_0, t_0, and M_0, to the data.

The extrapolation suggested[11] is convenient in cases where a sufficient portion of the tail is available. If large portions of the tail is lacking from the tracer curve, the method introduced[7], which includes data on both sides of the apex, is more robust, and can provide reliable extrapolations. The method[7] also works for cases when larger portions of the tail is available.

Tracer data, as well as the analytical models used to extrapolate the curves, are displayed in Fig. 5. The results show residence time distributions as a function of time for the E-1 tracer (PMCP) in producer B-1 (a), E-2 tracer (PMCH) in producer B-2 (b), E-3 tracer (PECH) in producer B-3 (c), and E-4 tracer (n-PPCH) in producer B-4 (d).

The measured data are represented by circles and the fit of the data are used to extrapolate the residence time distributions to infinity, as indicated by the dashed curves. The combined blue curve represents the full residence time distributions used to analyze the tracer data.

A bimodal distribution is observed for several of the tracers. To extrapolate the curve in such cases, a linear combination of solutions given by Eqn. 7 was used.

Results and Discussion

Tracer concentration curves are summarized and organized according to the injector-producer well pairs in Fig. 6. This illustration of the tracer data gives an overview of the flow patterns. The abscissa scale is similar for all tracer profiles, and since the injected amount is similar for all tracers, the relative significance of each of the injector-producer communications can be assessed by comparing the magnitude of the concentrations.

For example, we see directly from the figure that tracer transport from E-2 toward B-2 is comparable to that from E-4 to B-4, and that the transport from E-1 to B-1 is smaller than these two transports. The figure also shows that for all injectors, the producer directly opposite receives injectants from that corresponding injector.

The tracer production data can be compared to the WAG injection cycles. This is shown in Fig. 7 where the WAG cycle of specific injectors is compared to the tracer production curves in each offset producer of the tracer injected in the corresponding injector. The tracer curve of PMCP (injected in E-1) in producer B-1 is compared to the WAG cycle in E-1, the tracer curve of PMCH (injected in E-2) in producer B-2 is compared

Fig. 5 *Residence time distributions as a function of time.*

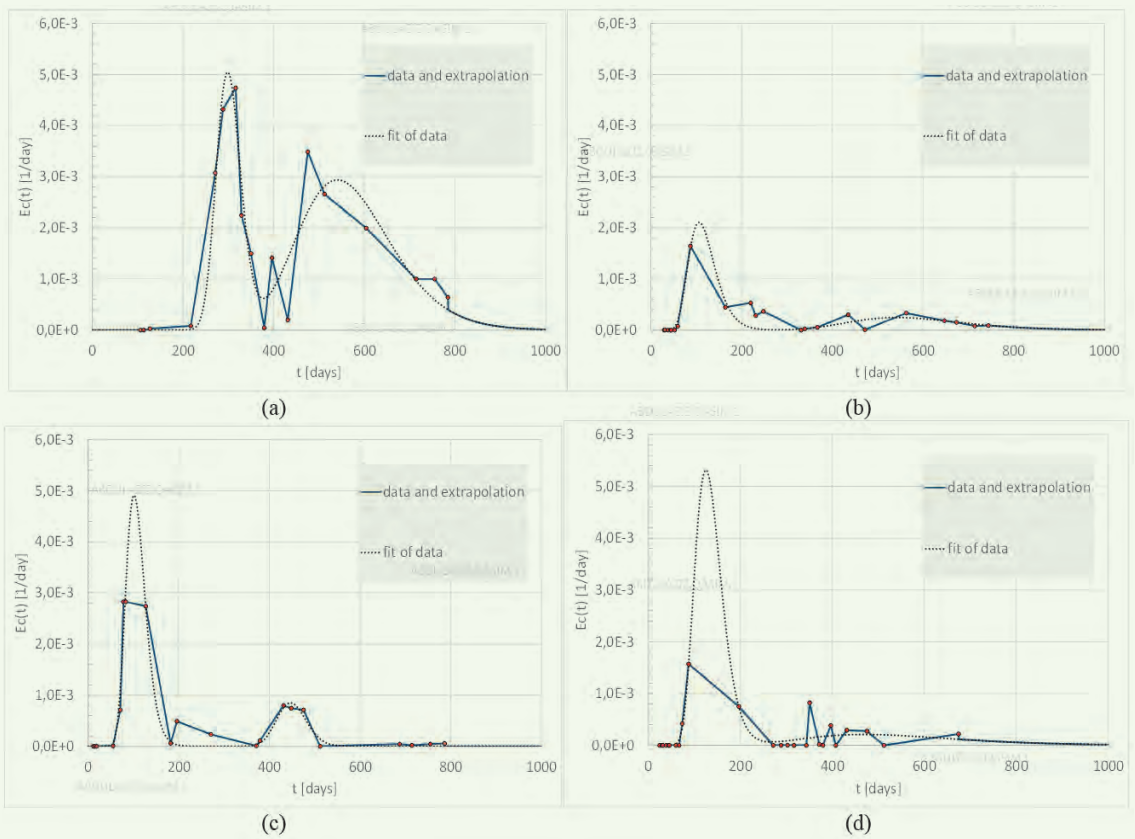

Fig. 6 *Tracer response of the gas tracers in the individual injector-producer well pairs where the tracer was identified.*

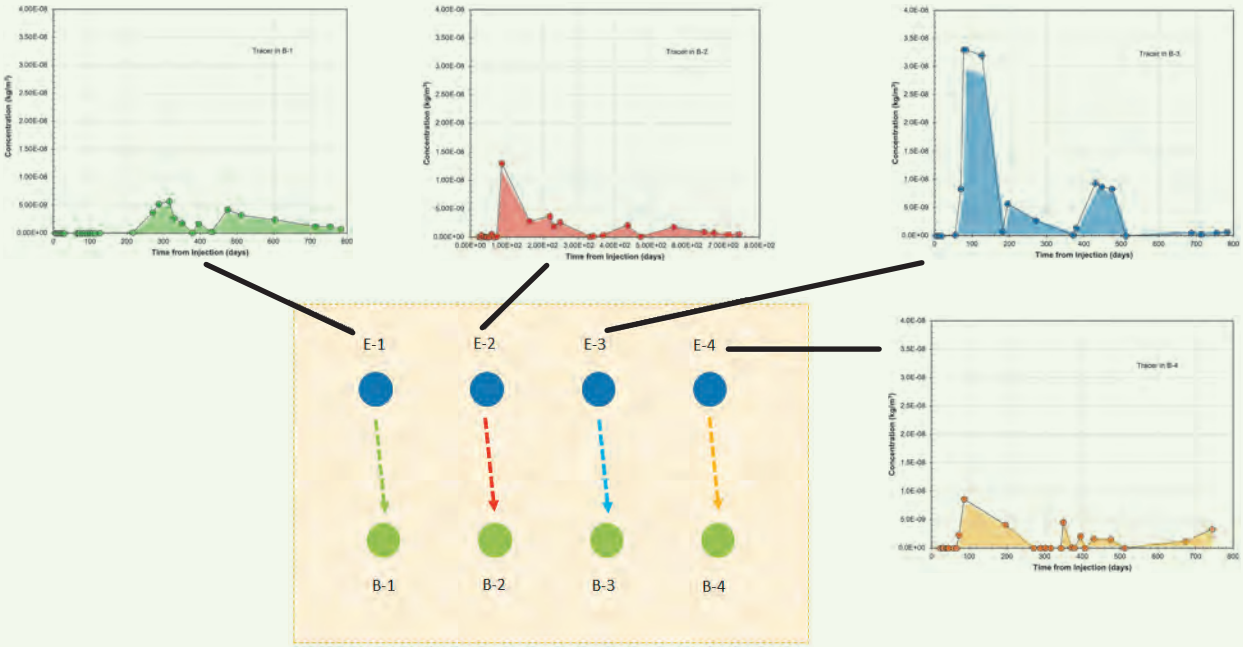

Fig. 7 *Tracer production curves in the producers compared to the WAG injection cycles in the injectors, corresponding to each tracer.*

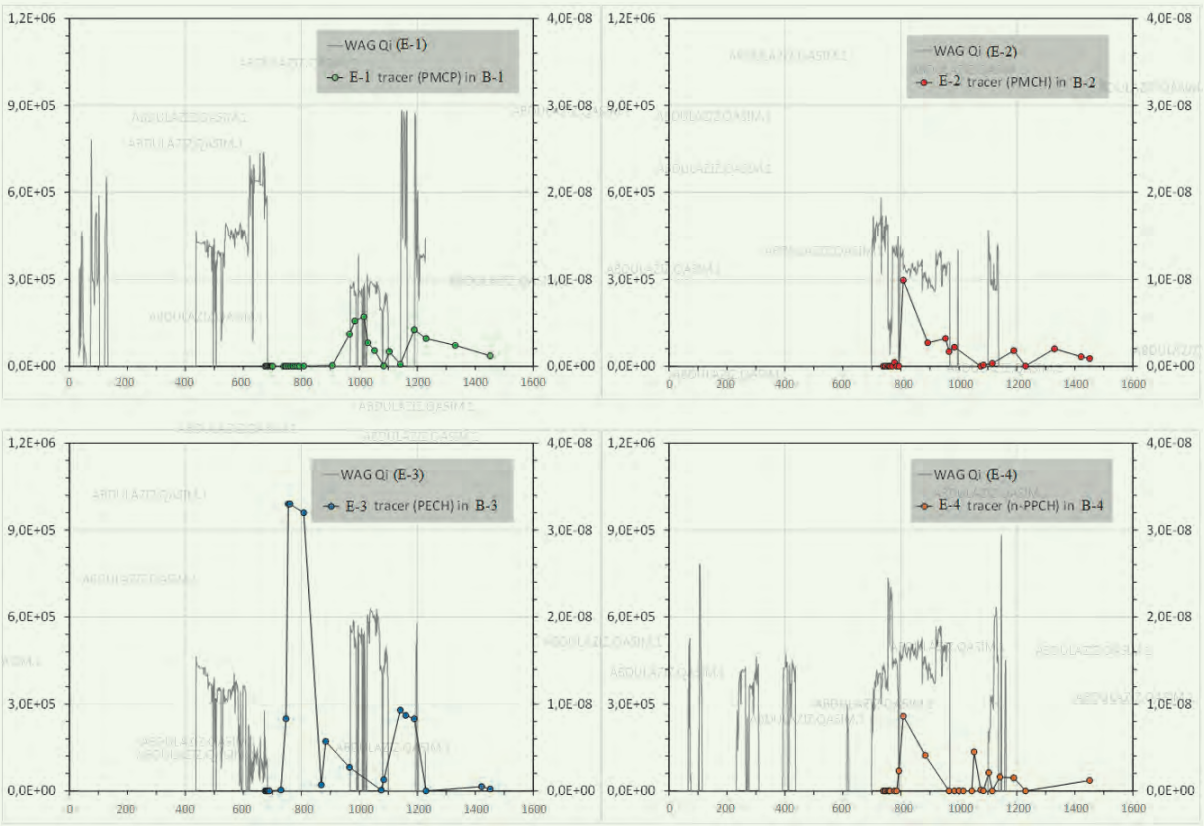

to the WAG cycle in E-2, the tracer curve of PECH (injected in E-3) in producer B-3 is compared to the WAG cycle in E-3, and the tracer curve of n-PPCH (injected in E-4) in producer B-4 is compared to the WAG cycle in E-4.

Direct comparison of the WAG injection cycles and the tracer production curves shows that the time scales are somewhat equal is duration for the tracers and the WAG cycles — in the sense that typical widths of the tracer curves correspond fairly well to those of the WAG cycles. Double peaks are visible in the tracer curves, with a time separation of the apex in the two peaks corresponding roughly to the time between the two WAG cycles.

As the WAG cycles correspond to injection and the tracer curves to production, they cannot be directly compared to reveal any correlation. To enable a direct comparison, the same data is therefore plotted in Fig. 8 with the tracer curves shifted by the time of arrival of the bulk of the tracers — times T_m in Table 3. In Fig. 8, we also note that for the two tracers moving from B-2 and B-4 to their corresponding producers E-2 and E-4, there is a fair overlap between the tracers and the WAG cycle. This may indicate that the tracers and the WAG cycle move simultaneously as one phase from the injectors to the producers.

Fig. 8 *Tracer production curves in the producers compared to WAG injection cycles in the injectors corresponding to each tracer.*

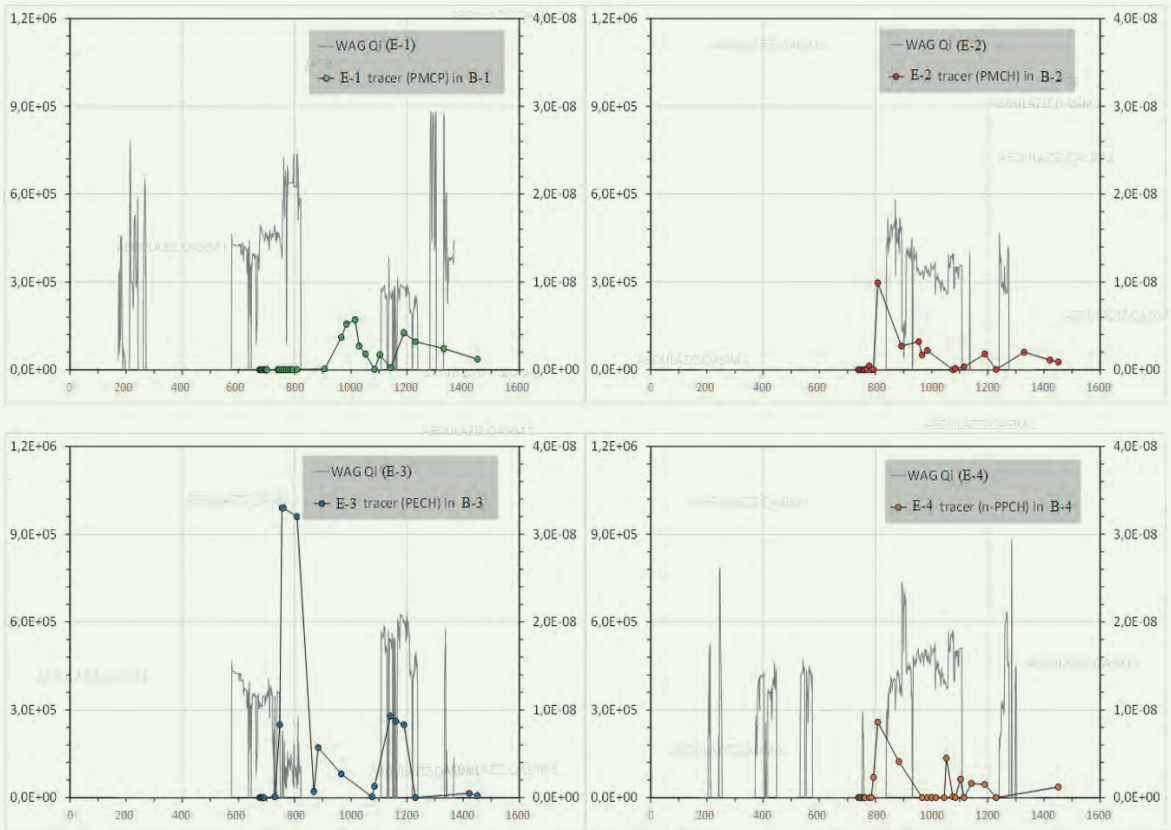

Table 3 *Summary of estimated quantities from the residence time distribution analysis for tracers in B-1, B-2, B-3, and B-4.*

Tracer	Injector	Producer	m_0	m_1 (days)	m_2 (10^5 days^2)	$\langle T \rangle$ (days)	T_m (days)	L_c	V_s (10^5 m)
PMCP	E-1	B-1	0.12	57	0.3	459	316	0.18	0.66
PMCH	E-2	B-2	0.22	69	0.3	308	88	0.4	0.23
PECH	E-3	B-3	0.35	71	0.2	203	103	0.36	0.04
n-PPCH	E-4	B-4	0.25	67	0.3	926	130	0.41	0.26

For the tracer injected in B-3 and produced in E-3, there is also a fair overlap — and interestingly a decrease in tracer production in the time interval corresponding to zero injection of gas in the WAG cycle. Again, this gives some support to a transport of the tracer together with the gas in the reservoir. For the last well pair (B-1 to E-1) there is no indication of an overlap. It is noted that this well pair is also the one with the longest residence time — $\langle T \rangle$ = 926 days — and with the longest time from injection to arrival of the tracer peak, T_m = 316.

One interpretation of this behavior for the tracer in this well pair is that it is transported through the gas phase, but with a delay due to contact with (partly stagnant) oil along its transport route toward the producer. This interpretation explains both the delayed arrival and the arrival in between WAG cycles.

To further quantify the transport of gas, a residence time distribution analysis of the tracer data was performed. In this analysis the following assumptions were made:

- All gas moved exclusively to the nearest producer, i.e., gas injected in E-1 moved toward B-1, gas injected in E-2 moved toward B-2, gas injected in E-3 moved toward B-3, and gas injected in E-4 moved toward B-4. This assumption is supported by the fact that this is the dominant pattern seen from the tracers, Fig. 6.
- All the injected gas was produced, and the production rate in a given producer corresponded to the average injection rate of the relevant injector. This assumption can be validated against actual gas, oil, hydrocarbon gas, and water production rates at relevant pressure and temperature.
- Finally, sweep volumes obtained using volumetric rates for the gas injection were converted to relevant reservoir volumes by assuming standard pressure and temperature for the surface conditions, and a reservoir pressure and temperature of 200 bar and 100 °C, respectively.

Results from the residence time distribution analysis based on the data and the extrapolations are summarized in Table 3. Recall that recovery of a tracer in a well is given by the zero order moment, Eqn. 4, of the residence time distribution. For a given producer, the recovery quantifies how much of the injected tracer is produced in that particular well. This implies that the zero order moment also quantifies how much of the injected gas from a given injector is produced in one particular producer[14]. From this quantity in Table 3 we can, e.g., conclude that the recovered mass is relatively similar for all well pairs, with an exception for E-1 to B-1, where the recovered mass is less than for the other producers.

The average time spent by the tracers in the reservoir equals the average travel time for the injected gas from the injectors to the producers. This is quantified by the average residence time $(T) = m_1/m_0$, also summarized in Table 3. From this, it is evident, e.g., that the time it takes to transport the gas phase from injector E-3 to B-3 is significantly smaller (about 200 days) than from E-4 to B-4 (about 900 days).

Another measure of transport time is given from T_m, the mode of the residence time distribution, corresponding to the apex in the tracer curves. The mode of the residence time distributions represents the typical transport time from the injectors to the producers. Note that overall it gives a smaller estimate of traveltime from the injectors to the producers. This reflects the fact that most of the tracers in the test display a bimodal nature and have relatively long tails.

The average time spent by the tracers in the reservoir is also related to the swept volume (V_s) between an injector and its offset producers. These volumes correspond to the volumes explored by the gas phase from a given injector that arrives at a given producer and the sweep volume can be used to quantify how effective the reservoir is flooded. If the sweep volume is large compared to the PV between an injector and a producer, the sweep is effective.

From Table 3 we see that the most effective sweep is from injector E-1 toward B-1. This sweep is about three times as effective as the sweep from E-2 to B-2, and E-4 to B-4. For the flow of the gas phase from E-3 to B-3, the sweep volume is significantly smaller than for the other well pairs. This suggests that the flow from E-3 to B-3 occurs in a particularly narrow space, compared to the other well pairs.

The flow capacity, $F(t)$, and the storage capacity, $\Phi(t)$, were estimated from the tracer data using Eqn. 5. These functions can be used to quantify the heterogeneity of the flow between an injector and producer. The Φ represents the volume accessible for flow and the F represents the flow and can be used to quantify how much of the flow occurs in a certain part of the accessible space. This gives an indication of the degree of heterogeneity of the reservoir. For a highly heterogeneous pore space, i.e., if large parts of the flow occur in a small fraction of the space, F increases fast with an increasing Φ. The heterogeneity can be quantified by the Lorentz coefficient, defined as the area between the $F - \Phi$ curve and the diagonal, normalized by one-half[12]:

$$L_c = 2\int_0^1 F(\Phi)d\Phi - 1 \qquad 8$$

L_c is zero for a perfectly homogeneous flow and one for perfectly heterogeneous flow — all flow in an infinitely narrow channel. Shook et al. (2009)[12] reports L_c = 0.18 for a homogeneous 5-spot and L_c = 0.7 for the fractured Beowawe geothermal reservoir. The results[7] gives L_c = 0.26 – 0.30 in the Lagrave carbonate reservoir.

For the cases investigated here, three of the well pairs (E-2/B-2, E-3/B-3, and E-4/B-4) yield $L_c \sim 0.36 - 0.41$, Table 3.

This indicates that the swept volume between the injectors and producers is relatively heterogeneous. For the last well pair, E-1/B-1, the heterogeneity index is significantly smaller ($L_c \sim 0.18$), indicating that the

Fig. 9 *Illustration of results from the residence time distribution analysis of gas tracer data.*

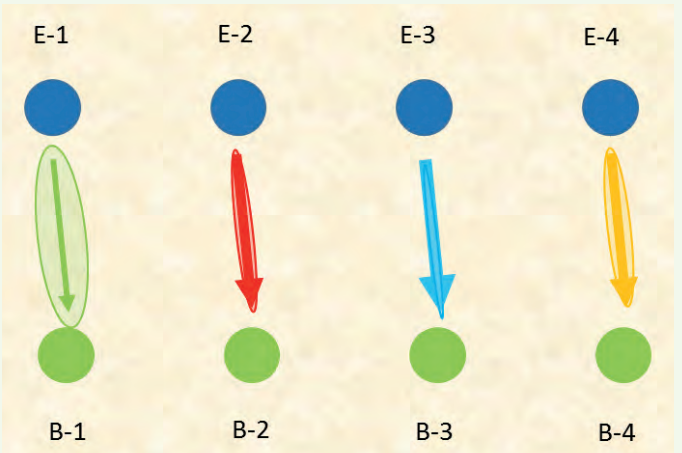

transport here is more homogeneous than for the other well pairs in the field.

Figure 9 summarizes the results from the residence time distribution analysis of tracer data in the field. The yellow arrow represents the flow of gas from injector E-4 toward B-4, the blue arrow represents flow from injector E-3 toward B-3, the red arrow represents flow from injector E-2 toward B-2, and the green arrow represents flow from injector E-1 toward B-1.

The widths of each of the arrows is proportional to the amount of tracer produced in each of the producers, and the areas of the ellipses correspond to the swept areas for each injector-producer well pair.

Conclusions

The IWGTT shows a potential in terms of ability to provide a quantitative overview of the connectivity in a given area of the reservoir interspersed with injector and producer well pairs. The data obtained from the IWGTT has been quite helpful in identifying the connectivity or fluid pathways between all the injector-producer well pairs for the project and assessing the "time of flight" between the injector and producer well pairs.

The detailed analyses of the results were compared to a characterization of waterflooding in the reservoir, obtained using water tracers, reported in previously published work[5]. These are reflective of some apparent reservoir heterogeneities that were not anticipated at the beginning of the pilot.

Acknowledgments

This article was presented at the Abu Dhabi International Petroleum Exhibition and Conference, Abu Dhabi, UAE, November 11-14, 2019.

References

1. Du, Y. and Guan, L.: "Interwell Tracer Tests: Lessons Learned from Past Field Studies," SPE paper 93140, presented at the SPE Asia Pacific Oil and Gas Conference and Exhibition, Jakarta, Indonesia, April 5-7, 2005.
2. Greenkorn, R.A.: "Experimental Study of Waterflood Tracers," *Journal of Petroleum Technology*, Vol. 14, Issue 1, January 1962, pp. 87-92.
3. Zemel, B.: *Tracers in the Oil Field*, in *Developments in Petroleum Science No. 43*, (ed.) Chilingarian, G.V., Amsterdam: Elsevier, 1995, 487 p.
4. Kleven, R., Høvring, O., Opdal, S.T., Bjørnstad, T., et al.: "Non-Radioactive Tracing of Injection Gas in Reservoirs," SPE paper 35651, presented at the SPE Gas Technology Symposium, Calgary, Alberta, Canada, April 28-May 1, 1996.
5. Sanni, M.L., Al-Abbad, M.A., Kokal, S.L., Hartvig, S.K., et al.: "A Field Case Study of Interwell Chemical Tracer Test," SPE paper 173760, presented at the SPE International Symposium on Oil Field Chemistry, The Woodlands, Texas, April 13-15, 2015.
6. Sanni, M.L., Al-Abbad, M.A., Kokal, S.L., Dugstad, Ø., et al.: "Pushing the Envelope of Residual Oil Measurement: A Field Case Study of a New Class of Interwell Chemical Tracers," SPE paper 181324, presented at the SPE Annual Technical Conference and Exhibition, Dubai, UAE, September 26-28, 2016.
7. Viig, S.O., Juilla, H., Renouf, P., Kleven, R., et al.: "Application of a New Class of Chemical Tracers to Measure Oil Saturation in Partitioning Interwell Tracer Tests," SPE paper 164059, presented at the SPE International Symposium on Oil Field Chemistry, The Woodlands, Texas, April 8-10, 2013.
8. Huseby, O.K., Hartvig, S.K., Jevanord, K. and Dugstad, Ø.: "Assessing EOR Potential from Partitioning Tracer Data," SPE paper 172808, presented at the SPE Middle East Oil and Gas Show and Conference, Manama, Kingdom of Bahrain, March 8-11, 2015.
9. Hartvig, S.K., Huseby, O.K., Yasin, V., Ogezi, O., et al.: "Use of a New Class of Partitioning Tracers to Assess EOR and IOR Potential in the Bockstedt Field," paper presented at the 18th European Symposium on Improved Oil Recovery, Dresden, Germany, April 14-16, 2015.
10. Shook, G.M.: "A Simple, Fast Method of Estimating Fractured Reservoir Geometry from Tracer Tests," *Transactions of the Geothermal Resources Council*, Vol. 27, 2003.
11. Shook, G.M. and Forsmann, J.H.: "Tracer Interpretation Using Temporal Moments on a Spreadsheet," Geothermal Technologies Program, Idaho National Laboratory Report, June 2005, 27 p.
12. Shook, G.M., Pope, G.A. and Asakawa, K.: "Determining Reservoir Properties and Flood Performance from Tracer Test Analysis," SPE paper 124614, presented at the SPE Annual Technical Conference and Exhibition, New Orleans, Louisiana, October 4-7, 2009.
13. Sharma, A., Shook, G.M. and Pope, G.A.: "Rapid Analysis of Tracer for Use in EOR Flood Optimization," SPE paper 169109, presented at the SPE Improved Oil Recovery Symposium, Tulsa, Oklahoma, April 12-16, 2014.
14. Huseby, O.K., Andersen, M., Svorstol, I. and Dugstad, Ø.: "Improved Understanding of Reservoir Fluid Dynamics in the North Sea Snorre Field by Combining Tracers, 4D Seismic, and Production Data," *SPE Reservoir Evaluation & Engineering*, Vol. 11, Issue 4, August 2008, pp. 768-777.

About the Authors

Dr. Abdulaziz S. Al-Qasim

Ph.D. in Petroleum Engineering, University of Tulsa

Dr. Abdulaziz S. Al-Qasim is a Petroleum Engineer and a Champion of Enhanced Oil Recovery Monitoring and Surveillance on the Reservoir Engineering Technology team of Saudi Aramco's Exploration and Petroleum Engineering Center – Advanced Research Center (EXPEC ARC). Since joining Saudi Aramco in 2007, he has been involved in enhanced oil recovery and improved oil recovery projects, reservoir management, field development, and production related challenges.

Abdulaziz's experience includes working in a variety of departments within Saudi Aramco. He has disclosed and filed more than 20 patents, contributed to over 20 papers, including peer reviewed papers, and deployed different technologies.

Abdulaziz was one of the finalists of the 2019 Energy Institute Young Energy Professional of the Year Award. He previously served as a Vice Chairman of the Society of Petroleum Engineers-Young Professionals (SPE-YP) regional symposium held in Oman in February 2009. Abdulaziz has also served in numerous SPE events at different levels.

He received his B.S. degree in 2007 from King Fahd University of Petroleum and Minerals (KFUPM), Dhahran, Saudi Arabia; his M.S. degree in 2011 from the University of Texas at Austin, Austin, TX; and his Ph.D. degree in 2016 from the University of Tulsa, Tulsa, OK, all in Petroleum Engineering.

Dr. Sunil L. Kokal

Ph.D. in Chemical Engineering, University of Calgary

Dr. Sunil L. Kokal is a Principal Professional and a Focus Area Champion of enhanced oil recovery (EOR) on the Reservoir Engineering Technology team of Saudi Aramco's Exploration and Petroleum Engineering Center – Advanced Research Center (EXPEC ARC). Since joining Saudi Aramco in 1993, he has been involved in applied research projects on EOR/improved oil recovery, reservoir fluids, hydrocarbon phase behavior, crude oil emulsions, and production-related challenges. Currently Sunil is leading a group of scientists, engineers and technicians in efforts to develop a program for carbon dioxide EOR and to conduct appropriate studies and field demonstration projects. Prior to joining Saudi Aramco, he worked at the Petroleum Recovery Institute, Calgary, Canada.

Sunil is a member of the Society of Petroleum Engineers (SPE), and he is a Registered Professional Engineer and a member of the Association of Professional Engineers, Geologists and Geophysicists of Alberta, Canada.

Sunil has written over 125 technical papers. He has served as an Associate Editor for the *Journal of Petroleum Science and Engineering* and SPE's *Reservoir Evaluation and Engineering Journal*.

Sunil is the recipient of several awards, including the SPE IOR Pioneer Award (2018), the SPE Honorary Member Award (2016), the SPE DeGolyer Distinguished Service Medal (2012), the SPE Distinguished Service Award (2011), the SPE Regional Technical Award for Reservoir Description & Dynamics (2010), and the SPE Distinguished Member Award (2008) for his services to the society. He also served as a SPE Distinguished Lecturer during 2007-2008.

In 1982, Sunil received his B.S. degree in Chemical Engineering from the Indian Institute of Technology, New Delhi, India, and in 1987, he received his Ph.D. degree in Chemical Engineering from the University of Calgary, Calgary, Alberta, Canada.

Sven K. Hartvig

M.S. in Nuclear and Analytical Chemistry, University of Oslo

Sven K. Hartvig is the Discipline Lead in reservoir tracer operations at RESMAN. He was one of the co-founders of the tracer service provider Restrack, recently acquired by RESMAN. Sven has 20 years industry and R&D experience in tracer technology. Previously, he was leading major R&D projects involving new inter-well tracer technology — from the lab scale up to operational full-field application.

Sven is a member of the Society of Petroleum Engineers (SPE) and the European Association of Geoscientists and Engineers (EAGE). He has coauthored several SPE papers pertaining to utilization of tracer technology.

In 1997, Sven received his M.S. degree in Nuclear and Analytical Chemistry from the University of Oslo, Oslo, Norway.

Dr. Olaf K. Huseby

Ph.D. in Reservoir Physics, University of Oslo

Dr. Olaf K. Huseby is the Discipline Lead in reservoir tracer operations at RESMAN. He was one of the co-founders of the tracer service provider Restrack, recently acquired by RESMAN. Olaf co-developed Restrack's interpretation schemes for inter-well and single well tracer data, including simulation as well as analytical techniques.

He has 20 years of industry experience, focusing on inter-well and single well tracer applications.

Olaf has published more than 50 scientific papers, and co-chaired and co-organized several Society of Petroleum Engineers (SPE) workshops on reservoir and tracer technology.

Olaf received his Ph.D. degree in Reservoir Physics from the University of Oslo, Oslo, Norway. He then went on to undertake postdoctoral studies in Poitiers and in Paris on transport processes in discrete fracture networks.

Notes

Notes

Have an article you would like to publish? Here are our guidelines.

These guidelines are designed to simplify and help standardize submissions. They need not be followed rigorously. If you have any questions, please call us.

Length

Average of 2,500-4,000 words, plus illustrations/photos and captions. Maximum length should be 5,000 words. Articles in excess will be shortened.

What to send

Send text in Microsoft Word format via email plus one hard copy. Send illustrations/photos and captions separately but concurrently, both as email and as hard-copy (see file format section for more information).

Procedure

Notification of acceptance is usually within three weeks after the submission deadline. The article will be edited for style and clarity and returned to the author for review. All articles are subject to the company's normal review. No paper can be published without a signature at the manager level or above.

Format

No single article need include all of the following parts. The type of article and subject covered will determine which parts to include.

Working Title
Lorem Ipsum here.

Abstract
Usually 150-300 words to summarize the main points.

Introduction
Different from the abstract in that it sets the stage for the content of the article, rather than telling the reader what it is about.

Main body
May incorporate subtitles, artwork, photos, etc.

Conclusion/Summary
Assessment of results or restatement of points in introduction.

Endnotes/References/Bibliography
Use only when essential. Use author/date citation method in the main body. Numbered footnotes or endnotes will be converted. Include complete publication information. Standard is *The Associated Press Stylebook*, 52nd ed. and *Wesbter's New World College Dictionary*, 5th ed.

Acknowledgments
Use to thank those who helped make the article possible.

Illustration/Tables/Photos and explanatory text

Submit these separately. Do not place in text. Positioning in the text may be indicated with placeholders. Initial submission may include copies of originals; however, publication will require the originals. When possible, submit both electronic versions and printouts. Color is preferable.

File Format

Illustration files with .EPS extensions work best. Other acceptable extensions are .TIFF/.JPEG/.PICT.

Permission(s) to reprint, if appropriate

Previously published articles are acceptable but can be published only with written permission from the copyright holder.

Author(s)/Contibutor(s)

Please include a brief biographical statement.

Submission/Acceptance Procedures

Papers are submitted on a competitive basis and are evaluated by an editorial review board comprised of various department managers and subject matter experts. Following initial selection, authors whose papers have been accepted for publication will be notified by email.

Papers submitted for a particular issue but not accepted for that issue may be carried forward as submissions for subsequent issues, unless the author specifically requests in writing that there be no further consideration.

Submit articles to:

Editor
The Saudi Aramco Journal of Technology
C-3D, Room AN-1080
North Admin Building #175
Dhahran 31311, Saudi Arabia
Tel: +966-013-876-0498
Email: *william.bradshaw.1@aramco.com.sa*

Submission deadlines

Issue	Paper submission deadline	Release date
Fall 2020	May 12, 2020	September 30, 2020
Winter 2020	August 13, 2020	December 31, 2020
Spring 2021	November 16, 2020	March 31, 2021
Summer 2021	February 9, 2021	June 30, 2021

There is more.

Dynamic Diverter Technology Efficiency in Acid Fracturing Applications

Qasim A. Sahu, Rommmel E. Arias and Eyad A. Alali

Abstract / Acid fracturing has been an integral part of reservoir development strategies for carbonate reservoirs as mechanical and chemical means of bypassing formation damage to enhance well productivity. Over the past few years, acid fracturing has significantly increased, targeting more carbonate reservoirs. There is a need to fully address the heterogeneous petrophysical and geomechanical properties of target reservoirs, which adversely affect the stimulation efficiency and production if fluids are not properly designed.

High Speed, High Rate Slim ESP Development and Qualification Testing

Rafael A. Lastra, Dr. Jinjiang Xiao, Dr. Woon Lee, and Alan Radcliffe

Abstract / Use of the electric submersible pump (ESP) is the most suitable artificial lift method for producing high flow rates, however, there are shortcomings with the standard ESP technology in slim well applications. On the one hand, well production is often curtailed due to pump performance limitations, and on the other hand, long strings and tight clearances make the current slim ESP systems more prone to failure when compared with larger diameter ESP applications.

Development of New Rheology Modifier for Invert Emulsion Drilling Fluids

Dr. Vikrant B. Wagle, Dr. Abdullah S. Al-Yami, Khawlah Alanqari, and Sara Alkhalaf

Abstract / It is of prime importance for a drilling fluid to have optimal rheology to achieve good hole cleaning, and to have good barite sag resistance. Invert emulsion fluids with organoclay as a viscosifier sometimes fail to maintain sufficient rheology during drilling, due to the thermal degradation of organoclay with time and temperature. Therefore, there was a need to develop a drilling fluid with optimal rheology sufficient to give good hole cleaning and barite sag resistance in high-pressure, high temperature (HPHT) conditions.

أرامكو السعودية
saudi aramco

Aramco
Journal
of Technology

Liked this issue? Sign up. It's free.

To begin receiving the *Aramco Journal of Technology* please complete this form, scan and send by email to ***william.bradshaw.1@aramco.com.***

Got questions?

Just give us a call at +966-013-876-0498 and we'll be happy to help!

Scan the QR code to go straight to your email and attach the form!

Subscription Form

Name
Title
Organization
Address
City
State/Province
Postal code
Country
Email address
Number of copies